Master's thesis

NTNU
Norwegian University of Science and Technology
Faculty of Natural Sciences
Department of Materials Science and Engineering

Martin Raaen

Silicon nanowires grown-on-graphite as composite anodes for high-energy lithium ion batteries

Tin oxide and tin sulfide as catalysts
Cyclohexasilane as silicon precursor

Master's thesis in Chemical engineering and biotechnology
Supervisor: Pascale Chenevier and Ann Mari Svensson
August 2022

NTNU
Norwegian University of Science and Technology

Martin Raaen

Silicon nanowires grown-on-graphite as composite anodes for high-energy lithium ion batteries

Tin oxide and tin sulfide as catalysts
Cyclohexasilane as silicon precursor

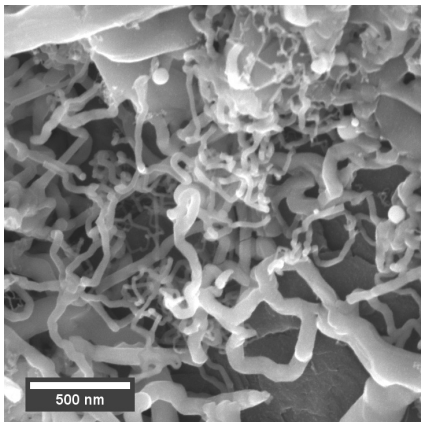

Master's thesis in Chemical engineering and biotechnology
Supervisor: Pascale Chenevier and Ann Mari Svensson
August 2022

Norwegian University of Science and Technology
Faculty of Natural Sciences
Department of Materials Science and Engineering

NTNU
Norwegian University of
Science and Technology

Preface

This is a master thesis in chemical engineering and biotechnology with specialization in materials chemistry and energy technology at the Norwegian University of Science and Technology (NTNU). The thesis was written in Grenoble, France, during a 5-month internship at Commisariat à l'énergie atomique et aux énergies alternatives (CEA) in the research group IRIG/SyMMES/STEP. A portion of the thesis is a part of the project "Research on the Cyclohexasilane in the creation of silicon anodes", which is a collaboration between CEA and The Coretec Group, the producer and provider of Cyclohexasilane.

I want to give a huge thanks to my supervisor Pascale Chenevier, who gave me a warm welcome in the lab and provided continuous guidance and support throughout my internship, with a contagious passion for science. Also big thanks to my supervisor from NTNU, Ann Mari Svensson, for helping me realize this exchange to Grenoble and for the regular follow-up. Thanks to Dmitry Aldakov for doing XPS measurements and fitting of the resulting data, and to Katharina Märker who conducted the ^{1}H-NMR measurements for this project and helped interpret the data. I want to send my thanks to Daniel Tomasi for training in electrode formulation and coin cell assembly, and to Cédric Haon for helping set up the battery testing and for sharing his knowledge about electrochemistry. Thanks to Jingxian Wang for being a great team member and for helping me during synthesis of tin sulfide nanocrystals. I also want to thank Théodore Barret, my office-roommate, for sharing his experience in the lab and for nice moments both in and outside of the office.

Abstract

Silicon is a promising anode material for future high-energy lithium ion batteries, but it has issues with a low electronic conductivity and high volume changes during cycling. Silicon nanowires combined with graphite as a composite anode can mitigate these limitations. Tin-based seeds is a low-cost alternative to gold as a catalyst for growth of Si nanowires through the vapor-liquid-solid (VLS) method, and the process can be improved further by increasing the silicon yield through new silicon precursors.

Two new VLS synthesis routes of graphite-silicon nanowire (Gt-SiNW) active materials were explored in this work: 1) Tin oxide and tin sulfide as catalysts and 2) Cyclohexasilane (CHS) as silicon source. The aim was to identify chemical and structural changes in the material induced by the different growth methods, and their effect on the electrochemical performance when assembled in batteries.

Gt-SiNW active materials with Si contents of $\sim$20 wt% were made through a one-pot-synthesis using a VLS growth mechanism with tin catalysts. Their microstructure and chemical composition was studied by materials characterization, and their performance in batteries was tested in half-cells. A series of SiNW-growths with various percentages of CHS in a mixture with diphenylsilane as precursor was conducted to test the nanowire growth, before two precursor compostions of 100% and 46% CHS were chosen for Gt-SiNW composite synthesis and battery tests.

Gt-SiNW synthesis by SnO_2 formed nanowires with smaller diameter and an additional oxide layer compared to SnS. The smaller diameter nanowires gave a better capacity retention, but higher initial capacity loss. SnO_2 and SnS catalysts gave average specific capacities of 1017 and 1123 $\mathrm{mA\,h\,g^{-1}}$ at cycle 150, respectively. CHS improved Si yield with 25%, but did not grow nanowires for CHS-rich precursors. On graphite substrates, pure CHS formed 50-100 nm silicon balls, while 46% CHS in the precursor gave nanowires. The Si "nanoballs" gave a lower Coulombic efficiency, but lower initial capacity loss than the wires. After 60 cycles, the average specific capacities were 829 and 731 $\mathrm{mA\,h\,g^{-1}}$ for 100% CHS and 46% CHS precursors, respectively.

Sammendrag

Silisium er et lovende anodemateriale for fremtidige litium-ionbatterier med høy energitetthet, men det finnes utfordringer med lav elektrisk ledningsevne og store volumendringer av materialet under sykling. Silisium nanotråder kombinert med grafitt som en kompositt-anode kan dempe disse begrensningene. Tinnbaserte frøpartikler er et rimelig alternativ til gull som katalysator for vekst av silisium nanotråder gjennom vapor-liquid-solid (VLS) metoden, og prosessen kan bli ytterligere forbedret ved å øke silisiumutbyttet gjennom bruk av nye forløpere.

To nye VLS synteseruter av grafitt-silisium nanotråd (Gt-SiNW) aktive materialer ble utforsket i dette arbeidet: 1) Tinnoksid og tinnsulfid som katalysatorer og 2) Syklohexasilan (CHS) som silisiumkilde. Målet var å identifisere kjemiske og strukturelle endringer i materialet som følge av de forskjellige vekstmetodene, og deres effekt på den elektrokjemiske ytelsen av anoder i batterier.

Gt-SiNW aktive materialer med Si-innhold på $\sim$20 wt% ble laget gjennom en one-pot-syntese ved bruk av en VLS-vekstmekanisme med tinnkatalysatorer. Mikrostruktur og kjemisk sammensetning ble studert ved materialkarakterisering, og materialenes ytelse i batterier ble testet i halvceller. En serie SiNW-vekster med ulike prosentandeler CHS i en blanding med difenylsilan som forløper ble utført for å teste innvirkningen av CHS på veksten av nanotråder, før to forløpersammensetninger på 100% og 46% CHS ble valgt for syntese av Gt-SiNW kompositter og batteritester.

Gt-SiNW syntese ved hjelp av SnO_2 som katalysator dannet nanotråder med mindre diameter og et ekstra oksidlag sammenlignet med da SnS ble brukt som katalysator. Nanotrådene med mindre diameter ga en bedre kapasitetsbevaring, men høyere initialt kapasitetstap. SnO_2- og SnS-katalysatorer ga gjennomsnittlig spesifikk kapasitet på henholdsvis 1017 og 1123 $\mathrm{mA\,h\,g^{-1}}$ ved syklus nummer 150. CHS forbedret Si-utbytte med 25%, men produserte ikke nanotråder for forløpere med over 54% CHS. På grafittsubstrat dannet ren CHS 50-100 nm silisiumkuler, mens 46% CHS i forløperen ga nanotråder. Silisium "nanokuler" ga en lavere Coulombisk effektivitet, men lavere initialt kapasitetstap enn nanotrådene. Etter 60 sykluser var den gjennomsnittlige spesifikke kapasiteten 829 og 731 $\mathrm{mA\,h\,g^{-1}}$ for henholdsvis 100% CHS og 46% CHS-forløpere.

Abbreviations

EV - Electric vehicle

SiNW - Silicon nanowire

Gt-SiNW - Graphite-Silicon nanowire

CHS - Cyclohexasilane

SEI - Solid electrolyte interphase

CE - Coulombic efficiency

DEC - Diethyl carbonate

EC - Ethylene carbonate

DMC - Dimethyl carbonate

VLS - Vapor-liquid-solid

CVD - Chemical vapor deposition

XPS - X-ray photoelectron spectroscopy

SEM - Scanning electron microscopy

EDX - Energy dispersive X-ray analysis

NMR - Nuclear magnetic resonance

Contents

Chapter 1

Introduction

Global warming and climate change is forcing humanity to act quickly in terms of reducing greenhouse gas emissions and improving sustainability in everything we do. Both road transportation and the energy industry are major sources of greenhouse gas emissions due to their dependence on fossil fuels. With an ever-increasing global energy demand, the transition to renewable energy sources is urgent, and electrification of the transport sector has been identified as an encouraging solution to reduce emissions. [1] Promising renewable energy sources like wind and solar energy are intermittent, and together with electric road transport they will drastically increase the demand for mobile, sustainable, high-quality energy storage in the coming years. [2]

Lithium ion batteries is the state of the art battery when it comes to electric vehicles (EVs), and they are also used in stationary energy storage applications. Compared to other battery technologies, lithium ion batteries have a high energy density and power density coupled with a long lifetime. For EV applications though, energy density of batteries still restricts the driving range, which makes developing new electrode materials with higher capacity a priority, in addition to optimizing safety, sustainability and costs. [3]

Silicon is considered a promising candidate for next generation anode materials, due to its high theoretical capacity ($3579\,\mathrm{mA\,h\,g^{-1}}$), abundancy, low cost, appropriate working potential and already well developed industrial applications in e.g. electronics and photovoltaics. [4] Silicon anodes have challenges when it comes to large volume changes during cycling with detrimental consequences for their cycle life, and a low electronic conductivity. [5] Among several other methods to mitigate these disadvantages, nanostructuration in terms of silicon nanowires (SiNW) has been identified as a promising technique. [6] Due to a limited capacity of current commercial cathodes, a specific capacity of around $1000\,\mathrm{mA\,h\,g^{-1}}$ in the anode is ideal for improving

energy density while maintaining mechanical stability of the electrode. [7] Composite anodes with around 25 wt% silicon mixed with graphite is a way of reaching this specific capacity while benefitting from the excellent cyclability of graphite. [8] The following study will thus focus on new ways of synthesizing graphite-silicon nanowire (Gt-SiNW) composite anodes for improving the energy density of future lithium ion batteries.

Aim of work

The main aim of the work is to fabricate composite materials of silicon nanowires grown on graphite with Si content around 20-25 wt%, and evaluate the performance of the materials as anode material for lithium ion batteries. Specifically, the work has focused on:

- Growth of silicon nanowires directly onto graphite by use of a mixture of diphenylsilane and phenylsilane as the silicon precursor, comparing effects of tin oxide or tin sulfide catalysts on the graphite surface. Tin oxide and tin sulfide represent two different oxidation states of tin, Sn(+IV) and Sn(+II), and they introduce different impurities to the system in terms of oxygen and sulfur, respectively. This can influence the chemical composition, size and shape of the synthesized Gt-SiNW active material, which again has an impact on the electrochemical performance. Thus, the active material will be characterized, and anodes will be fabricated from the active materials and tested in batteries.

- The effects of cyclohexasilane as precursor on the growth of nanowires. Pure silicon nanowires with no graphite substrate will be synthesized with precursor compositions of around 0%, 25%, 50%, 75% and 100% cyclohexasilane in a mixture with diphenylsilane, in order to identify differences in microstructure and chemical composition of the products, and also identify whether cyclohexasilane can improve silicon yield and reduce the growth temperature of silicon nanowires due to its high number of silicon atoms and high reactivity.

- Identifying the effect of cyclohexasilane as precursor on the electrochemical performance. This will be done by growing nanowires on graphite for selected precursor compositions of cyclohexasilane and diphenylsilane, and fabricating anode materials for testing in batteries.

Chapter 2

Theory

2.1 Introduction to lithium ion batteries

A lithium ion battery is a secondary battery, an energy storage device which transforms chemical energy to electrical energy upon discharging and vice versa during charging. The main components of a lithium ion battery are two electrodes (one positive and one negative) separated by an ion-conducting electrolyte. The positive and negative electrodes are electrically connected through an external circuit. During discharging, an oxidation reaction at the negative electrode releases lithium ions which move through the electrolyte towards the positive electrode. At the same time, a low electronic conductivity in the electrolyte forces the electrons from the same electrochemical reaction through the external circuit where they can do work. [9]

The terms anode and cathode are used for the electrodes where oxidation and reduction reactions take place, respectively. As the electrode reactions change direction depending on whether the battery is charging or discharging, the terms anode and cathode may lead to confusion. By convention, the electrodes will be referred to as if the battery is discharging. This means that when the anode is mentioned, it is the negative electrode which is referred to.

For cells with a liquid electrolyte, a separator is placed between the two electrodes as a porous barrier to avoid short circuits while still allowing ion-conduction between the two electrodes. Standard liquid electrolytes are based on carbonate solvents in a mixture with the lithium salt $LiPF_6$. As an alternative to liquid electrolytes, all-solid-state lithium batteries with gel, polymeric or glassy matrices as electrolyte are being researched for a future generation of lithium ion batteries. [10]

In a lithium ion battery, both electrodes are capable of storing lithium ions, either through alloying, conversion reactions or through intercalation. Intercalation is the

reversible insertion of an ion or a molecule within a crystalline structure, and it is the most common mechanism for lithium ion storage in electrode materials.

The first commercial lithium ion battery is a good example for describing their working principles. It was commercialized in 1991 by Sony [11], and the technology is still used commercially in 2022. An illustration of the cell is shown in Figure 2.1.1. This battery has the lithiated transition metal oxide $LiCoO_2$ as cathode material, and graphite as anode material. $LiCoO_2$ has a $\alpha-NaFeO_2$ structure capable of intercalating lithium ions [12], and the weak interlayer bonds in graphite makes it a good intercalation host while allowing fast Li^+ diffusion through the material. Both graphite and $LiCoO_2$ also have sufficient electrical conductivity for transporting electrons between the electrode and the current collector.

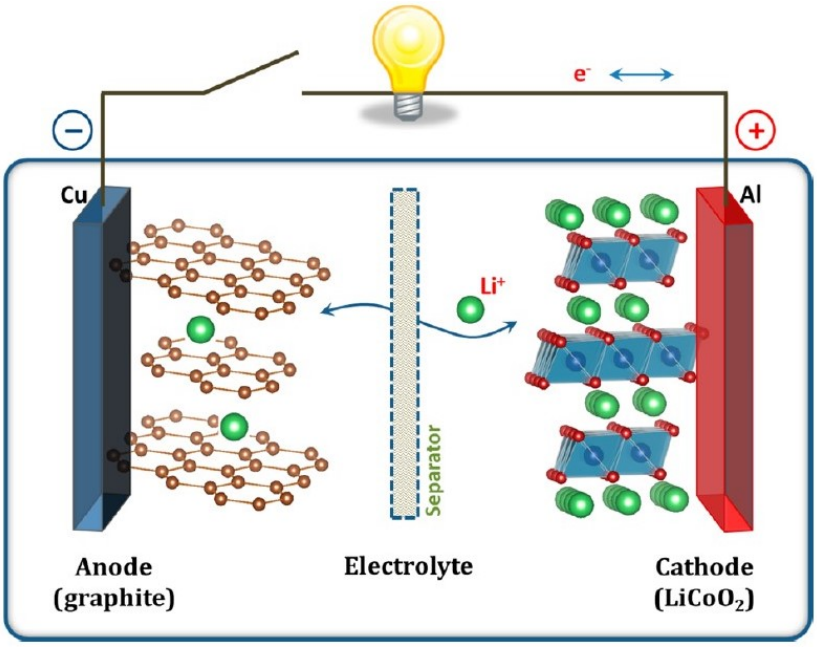

Figure 2.1.1: Illustration of a lithium ion battery cell, with $LiCoO_2$ as cathode material and graphite as anode. Figure from [9].

2.1.1 Battery terminology

Battery cell potential, or cell voltage (E_{cell}) is given by the difference in chemical potential between the two electrodes, $\Delta G = -nFE_{cell}$ [12], where ΔG is the Gibbs free energy of the total reaction in the battery, n is the number of electrons transferred in the electrode reactions and F is the Faraday constant. Open circuit voltage (V_{oc}) is the measured voltage over the cell when no current is running, and V_{oc} is dependent on the state of charge of the battery. The voltage during charge and discharge of the cell changes due to its internal resistance (R_b). When charging, the resistance will increase the voltage such that more energy is needed to charge the battery. Similarly, the internal resistance causes a lower voltage when discharging, as seen in Equation (2.1.1),

$$\begin{aligned} V_{ch} &= V_{oc} + I_{ch}R_b \\ V_{dis} &= V_{oc} + I_{dis}R_b, \end{aligned} \tag{2.1.1}$$

where $V_{ch} > V_{oc}$ and $V_{dis} < V_{oc}$ with discharge current defined as negative.

The capacity of a battery is a measure of the amount of charge it can store, and is limited by the electrode with the lowest capacity. The theoretical specific capacity (Q_{th}) of an electrode material can be calculated as shown in Equation 2.1.2:

$$Q_{th}(mAh/g) = \frac{nF}{3.6 \cdot M_m}, \tag{2.1.2}$$

where n is the amount of electrons transferred in the electrode reaction, F ($\mathrm{C\,mol^{-1}}$) is the Faraday constant and M_m ($\mathrm{g\,mol^{-1}}$) is the molar mass of the electrode material.

The energy which can be delivered by a fully charged battery cell can be described by the potential $V(q)$ when a charge q is moved between the two electrodes, integrated over the total charge that can be stored in the electrodes, Q, as in Equation 2.1.3: [9]

$$Energy\ (Wh) = \int_0^Q V(q)\ dq. \tag{2.1.3}$$

A useful term when discussing how much energy a battery can store is energy density. Volumetric (kWh/L) and specific (kWh/kg) energy densities are two common ways of expressing energy storage in batteries. In addition to energy density, power density is a key parameter, describing how much power the battery can deliver, i.e. how much energy it can deliver per time. As with energy density, power density can

be expressed with regards to volume or mass. Power density is closely related to C-rate, which is a measure of how fast the battery is charged/discharged. A C-rate of 2C means that the battery is charged/discharged in 30 minutes, while a C-rate of C/2 means that it takes two hours to fully charge/discharge the battery. A battery is often tested by changing C-rate through varying the current applied/drawn from the cell, to study its capacity at different charge/discharge rates.

Cycle life gives information about the lifetime of a battery, more precisely how many cycles it can make before its capacity starts dropping. A common convention is to say that a battery is at the end of its life when its capacity has dropped to 80% of its initial capacity [9], although Li-ion batteries at 80% of their full capacity can still be used for certain applications, e.g. in stationary storage, which is less stressful than for instance EV applications. [13]

Coulombic efficiency (CE) is the relation between the discharge- and charge capacity of a battery, as seen in Equation 2.1.4,

$$CE = \frac{Q_{dis}}{Q_{ch}}, \tag{2.1.4}$$

where Q_{dis} is the discharge capacity and Q_{ch} is the charge capacity. CE gives information about the reversibility of the cell reactions, and an average CE of around 99.8% is demanded for industrially viable batteries. [5]

2.1.2 Optimization of Li-ion batteries

An ideal Li-ion battery should be optimized in terms of the following parameters: [9]

- A high voltage difference between the electrodes, and a stable electrolyte in the whole voltage window.
- High specific and volumetric capacity of electrode materials to lower the weight and volume of batteries.
- Compatibility with high currents for high power applications.
- A low internal resistance, reducing irreversible losses and improving overall efficiency.
- Safety regarding short circuits and thermal runway.
- Highly stable long term cycling.
- Sustainability in terms of non-toxic components and recyclability.

2.2 Battery materials

The reaction $\mathrm{Li} \longrightarrow \mathrm{Li}^+ + \mathrm{e}^-$ and the flow of both electrons and lithium ions in a lithium ion battery means that both electronic and ionic conductivity are crucial properties for electrode materials. Electrodes are generally made of an active material, binder and conductive additive, attached to a current collector which conducts current to the external circuit. The active material is able to store and transport lithium ions. Many electrochemically active materials are not great electronic conductors, which is why a conductive additive is added, e.g. carbon black. The binder is added to physically hold the electrode together, and to ensure adhesion to the current collector. [12, 14]

Low cost, non-toxicity, sustainability and simple manufacture are key requirements for electrode materials. The electrode reactions should also be highly reversible, for an efficient charge and discharge of the battery. Phase changes and structure changes due to varying lithium content in the electrode is unwanted, as it is energy-wasting and possibly detrimental for the reversibility of electrode reactions. [12]

2.2.1 Anode materials

As of 2022, graphite is by far the most used anode material in lithium ion batteries, due to its abundancy, cycling stability, low cost and respectable theoretical capacity of $372\,\mathrm{mA\,h\,g^{-1}}$. In addition, graphite has a low delithiation potential versus lithium, a high diffusivity of Li^+ and a relatively low volume change during lithiation/delithiation. [15] In graphite anodes the active material is synthetic or natural graphite, the conductive additive is a carbon material, e.g. acetylene black, and polyvinylidene fluoride (PVDF) is a commonly used binder. [16]

Intercalation in graphite happens between graphene planes, which are bound together by weak van der Waals forces. Up to one lithium atom per six carbon atoms can be stored in graphite, following the reaction in Equation (2.2.1), [10]

$$6\,\mathrm{C} + \mathrm{e}^- + \mathrm{Li}^+ \rightleftharpoons \mathrm{LiC_6}. \tag{2.2.1}$$

An ideal anode for lithium ion batteries is simply lithium metal, which has the lowest negative electrochemical potential of all elements at $-3.040\,\mathrm{V}$ versus the standard hydrogen electrode. It also has a low density and an extremely high theoretical specific capacity of $3860\,\mathrm{mA\,h\,g^{-1}}$. There are two main problems with lithium metal anodes: dendrite formation on the electrode surface during charge, and a low Coulombic efficiency. This leads to safety problems due to dendrites causing short circuits and

increased surface area, giving rise to thermal runaway and explosion hazards. It also gives a short cycle life for the electrode, but lithium metal anodes are still an active domain of research. In parallel, lithium metal electrodes are used for electrode testing in half-cell configurations due to their stable reference potential. [17]

In addition to lithium metal and intercalated graphite, another type of lithium battery anodes are alloying anodes, which electrochemically alloy to form lithium compounds. Alloying materials can have very high specific capacities, but they are known for their large volume change during lithiation/delithiation. [15] Silicon is one of the lithium alloying materials which has received a lot of attention, due to its extremely high specific capacity and low average delithiation potential. Silicon as an anode material is further discussed in Section 2.3.

2.2.2 Cathode materials

Lithium ion batteries are generally assembled in a discharged state, which means that the cathode is the "lithium source" of the battery, supplying lithium ions that are needed for the charging reaction by lithiation of the graphite. Cathodes are thus lithiated compounds, and the vast majority of cathode materials are made of lithiated transition metal oxides or phosphates. The a transition metal can change valence during charge/discharge of the battery, which is necessary to compensate the lithiation/delithiation during cycling. [12]

As mentioned in Section 2.1, $LiCoO_2$ was the first commercialized cathode material, with a layered $\alpha-NaFeO_2$ structure. Other layered cathode materials have followed, e.g. $LiNi_xMn_yCo_{1-x-y}O_2$ (NMC), of which several compositions of Ni, Mn and Co are being studied. In addition to layered cathode materials, spinel and olivine crystal structures are two other main groups. $LiMnO_4$ and $LiFePO_4$ are examples of the most used spinel and olivine structured cathodes, respectively. [18] Cathodes are seen as the limiting component in terms of energy density, and it is also the most costly component in current batteries. Although NMC cathodes with specific capacities of more than $200\,mA\,h\,g^{-1}$ have been reported, [19,20] this is still lower than the specific capacity of commercial graphite anodes.

2.2.3 Electrolytes

The electrolyte is a critical component in a lithium ion battery. Because of a large potential difference between electrodes when cycling a lithium ion battery, aqueous electrolytes cannot be used. Alkyl carbonates have been identified as organic liquids with a sufficiently wide electrochemical stability window, with ethylene carbonate (EC), diethyl carbonate (DEC) and dimethyl carbonate (DMC) as examples. The "electrochemical window" for the electrolyte is determined by the energy gap between the highest occupied and lowest unoccupied molecular orbitals (HOMO and LUMO). [9] If the electrochemical potential of the cathode is lower than the HOMO of the electrolyte, the electrolyte will oxidize at the cathode. Similarly, unwanted reduction of the electrolyte would happen at the anode if the anode had higher electrochemical potential than the LUMO of the electrolyte.

Commercial liquid electrolytes are formed by mixing one or multiple of the components EC, DEC and DMC in a binary mixture with $LiPF_6$-salt. An example is 1M $LiPF_6$ solvated in a 1:1 mass ratio mixture of DMC and EC. [10] When using liquid electrolytes, a porous ion-conducting separator is added to the system to avoid short circuits between the anode and the cathode. As an alternative to organic liquids, solid-state electrolytes are being developed for increased safety and energy density. Insufficient ionic conductivity and a limited connectivity to electrode surfaces is delaying commercialization of solid-state electrolytes, but perovskites, sulfide-based inorganics and various types of polymer electrolytes (gel-, composite- and solvent-free-polymers) are promising candidates. [21]

2.3 Silicon as anode material

2.3.1 Overview

In the search for anode alternatives to graphite, silicon has received a lot of attention due to its extremely high theoretical capacity (around 3579 $\mathrm{mA\,h\,g^{-1}}$ for the lithiated alloy $Li_{15}Si_4$) [4], only lithium metal among other anode materials is comparable in terms of theoretical capacity. Si has a relatively low discharge voltage, at 0.4 V versus Li/Li^+. [16, 22] This delithiation voltage is higher than for graphite, which can help avoiding deposition of lithium metal on the electrode during fast charging [23]. Figure 2.3.1 shows potential versus Li/Li^+ as a function of specific capacity for various anodes, showing that alloying anodes like silicon can reach very high specific capacities compared to other technologies while still maintaining a low voltage versus Li/Li^+.

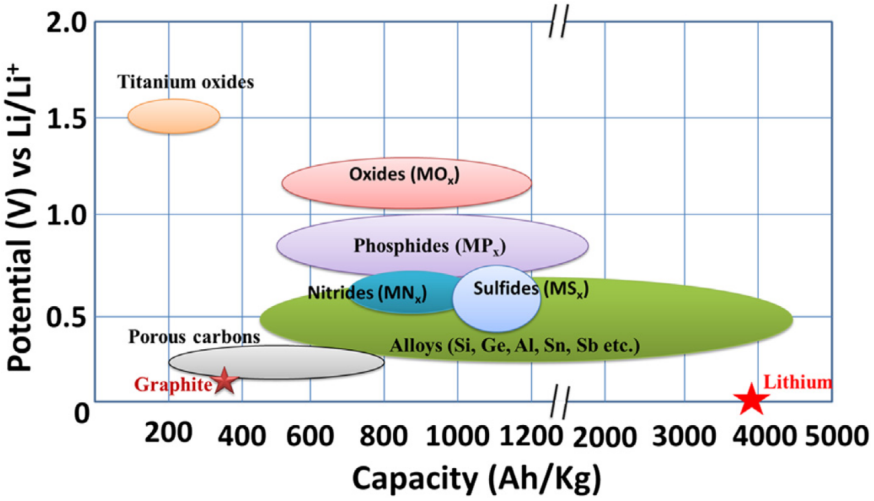

Figure 2.3.1: Potential versus Li/Li^+ as a function of specific capacity for several anode technologies. Adopted from [24].

Silicon is the second most abundant element in the earth's crust, it is non-toxic, cheap and due to its applications in chemistry, glassware, electronics and photovoltaics, a mature infrastructure for processing of the material already exists. [6] The increasing interest for silicon usage in batteries is clear when looking at Figure 2.3.2, showing the amount of publications from the Web of Science database including the keywords "battery" and "silicon" between 2005 and 2021. In this period, the amount of publications on this topic showed almost a ten-fold increase.

The main limitations when it comes to using silicon as anode material, are large volume variations during lithiation/delithiation and a relatively low electronic con-

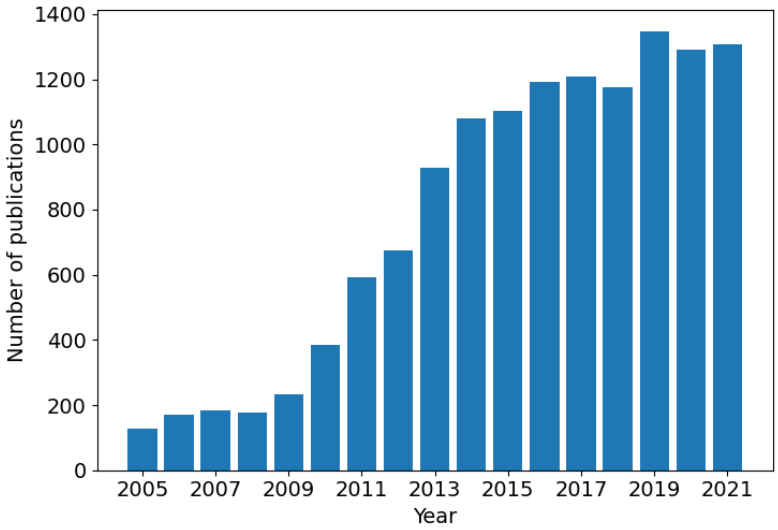

Figure 2.3.2: Chart showing the amount of publications on the use of silicon in batteries as a function of publication year. The data was obtained by the use of "battery" and "silicon" as search items in the Web of Science database.

ductivty and lithium diffusivity. [25–27] These issues result in pulverization, loss of electrical contact and capacity fading of the material, causing a detrimental effect on the cycle life of the battery. [4,5,8] Several approaches have been made to avoid these issues; addition of electrolyte additives and new binders to affect the SEI-layer, or design of silicon materials through porous structures, nanocomposites or nanostructures. [16,23]

2.3.2 Alloying mechanism - lithiation and delithiation of Si

In most commercial electrode materials, lithium is stored through intercalation. This way, the ions take interstitial positions in the host lattice and only small structural changes take place in the host material during repeated lithiation and delithiation. This gives the electrodes good cycle life, but at the same time the capacity is limited by the number of intercalation sites in the host. For alloying electrodes like silicon, breaking of bonds in the host lattice to form an alloy phase means that the capacity is not restricted by the number of sites in the silicon framework, making them able to reach ten times higher specific capacities than anodes based on intercalation. [28]

The silicon-lithium phase diagram in Figure 2.3.3 shows LiSi, $Li_{12}Si_7$, Li_7Si_3, $Li_{13}Si_4$ and $Li_{22}Si_5$ as some of the main Li-Si alloy phases with high lithium content. Equilibrium coulometric titration at 415 °C by Wen and Huggins [29] showed these

phases in a silicon electrode, suggesting that $Li_{22}Si_5$ is the most lithium-rich phase in the Si-Li system. According to the phase diagram, multiple phase transformations should take place during lithiation of silicon to reach the final phase of $Li_{22}Si_5$. This phase gives a theoretical specific capacity of $4200\,mA\,h\,g^{-1}$, but it is only reached at high temperature. [6, 23, 28] The composition with the highest lithium content at room remperature was observed by Obrovac and Christensen by using X-ray powder diffraction. [30] They observed $Li_{15}Si_4$, where Si atoms are isolated in equivalent crystallographic sites. This is a metastable phase, hence it is not visible in the equilibrium phase diagram.

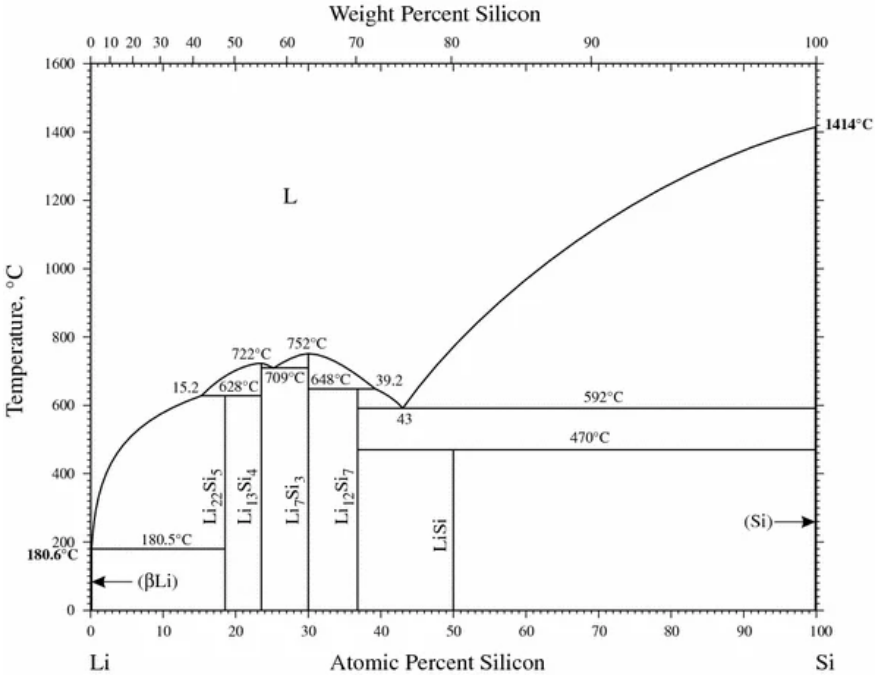

Figure 2.3.3: Phase diagram between silicon and lithium. Adopted from [31].

During cycling of crystalline silicon anodes at room temperature, silicon amorphizes during the first lithiation, giving a two-phase region of crystalline silicon and partly lithiated amorphous silicon. The two phases are separated by a sharp reaction front, most likely due to a high activation energy of breaking bonds in the crystalline silicon matrix. [28, 32] The lithium-silicon phases formed during lithiation is dependent on the lithiation potential. Various Li_xSi_y-phases are formed at around 0.1 V versus Li/Li^+, [33] and if the lithiation continues below 50 mV, the alloy suddenly crystallizes to $Li_{15}Si_4$. [23, 30, 34] The whole lithiation process progressively causes a volume increase of close to four times the original volume. [23, 35] This volume change can lead to failure through several mechanisms which will be discussed in Section 2.3.4. If the electrode potential is limited above 50 mV, the silicon will stay as

amorphous Li_xSi. Upon delithiation after crystallizing to $Li_{15}Si_4$, the silicon will go back to an amorphous phase, and stay amorphous throughout further cycling as long as the electrode potential is kept above 50 mV. Avoiding silicon crystallization could lead to a longer cycle life for the electrode, due to avoiding a two-phase region leading to higher internal stress and particle cracking. [22, 30, 34]

2.3.3 Solid Electrolyte Interphase layer

The Solid Electrolyte Interphase (SEI) is a passivation layer formed on the interface between the negative electrode and the electrolyte in a lithium ion battery. During the first charge of a battery, the negative electrode reaches a low potential at which the liquid electrolyte is unstable, and the SEI-layer is formed on the electrode due to an electrochemical decomposition of the electrolyte. [36] The onset voltage for SEI-layer formation is dependent on the electrolyte and electrode material, for commercial electrolytes and graphite the most reported value is around 0.8 V. [37] The SEI-layer consists of both organic and inorganic decomposition products, and acts as an electrically insulating layer between the electrode and the electrolyte. [38] The high electronic resistance limits the growth of the SEI layer. The transport of lithium through the SEI-layer is not as restricted, due to the exchange of ions between the electrolyte, SEI-compounds and lithium in the electrode. The cation transport number of the SEI-layer is ideally close to unity. This way, lithium ion batteries are capable of continuous charge/discharge cycling without a buildup of a too thick SEI-layer. [36, 37]

2.3.4 Failure mechanisms

The two main factors inhibiting cycling performance of silicon anodes are a low intrinsic electric conductivity [27] and the drastic volume change during lithiation/delithiation of the anode (close to 300% for $Li_{15}Si_4$). [23]

The volume changes induce large stresses in the material. As the particles expand and contract, the stress can cause cracks or flakes peeling off the particles, also known as pulverization. [39, 40] Cracking and pulverization lead to loss of electrical contact and therefore capacity fading and decreased rate performance. In addition to cracking and pulverization of the particles, volume changes in the anode can lead to problems at the level of the whole electrode by morphology changes at the micro/macro scale. This comes from particle size increasing upon lithiation, particles pushing each other away before decreasing in size, losing contact with each other. Another consequence could be a volume change of the whole electrode, with the risk for electrode peel-

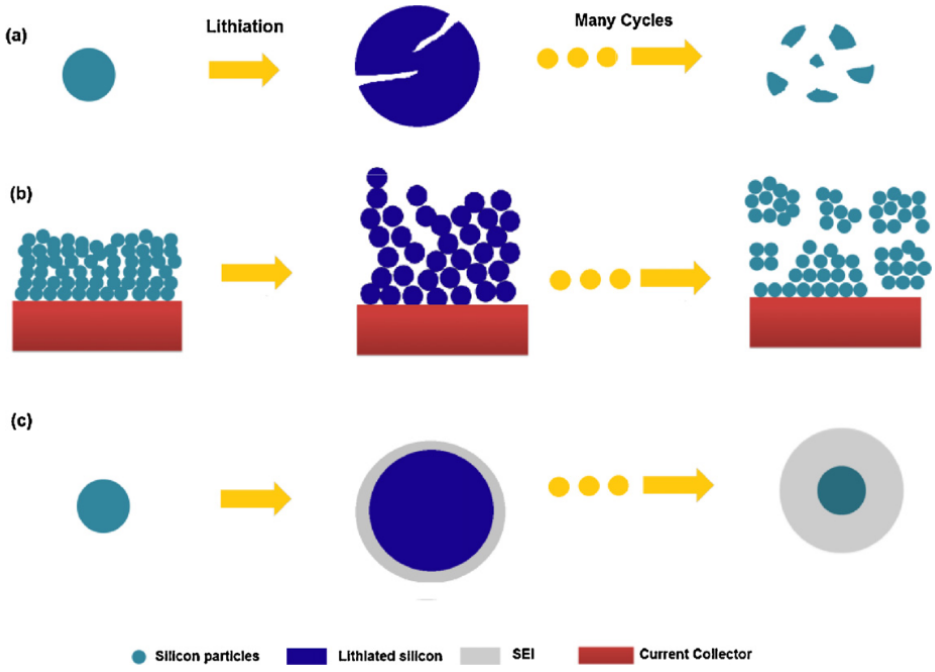

Figure 2.3.4: Illustration of failure mechanisms in silicon anodes. a) Shows particle pulverization, b) shows morphology changes in the electrode and c) shows SEI-layer growth. Adopted from Wu et. al. [6]

off, and thus loss of active material and contact with conductive additive and binder, causing capacity fade and detrimental effects on rate performance. [6] Particle pulverization and electrode morphology changes are illustrated in Figure 2.3.4a and 2.3.4b, respectively.

As the electrode is exposed to volume changes during cycling, the SEI-layer gets torn and stretched, causing cracks. New surface exposed to the electrolyte causes reformation of the SEI-layer. [23, 25] A continuous need to rebuild the SEI-layer causes electrolyte consumption and lithium loss, and it can also lead to a continuous buildup of the SEI-layer, illustrated in Figure 2.3.4c. [6] This leads to capacity fade of the battery. The importance of a strong and stable SEI-layer has already been discussed in Section 2.3.3, and a breakdown of this layer causes severe problems for the lifetime of the electrode and thus the whole battery.

2.3.5 Nanostructured silicon anodes

Significant efforts have been made to minimize the detrimental effects of silicon volume change during lithiation/delithiation, and decreasing the size of the material to the nano-scale has shown encouraging results when it comes to cyclability and rate performance of silicon anodes. [27, 41–43] Nanostructuring of silicon can provide the needed free volume to accomodate the large volume changes during cycling, and due to a more efficient stress relaxation, the nanomaterials are more resistant against fracture. [22] A high surface to volume ratio in nanostructured materials together with a decreased lithium ion diffusion length also tend to give improvements in terms of the rate capability of the material. [16] At the same time, a high surface area can lead to intensive reaction between particles and electrolyte, giving a decreased coulombic efficiency. [44] Increased cycle life for silicon anodes has been observed by using several different morphologies of nanostructured silicon, including silicon nanoparticles (SiNP) [45, 46], silicon nanotubes (SiNT) [47, 48], porous silicon nanostructures [49, 50] and silicon nanowires (SiNW) [6, 27, 33].

2.4 Silicon nanowires

2.4.1 Growth mechanism

There are several possible techniques for growing silicon nanowires, divided in two groups: Bottom-up and top-down approaches. Top-down is based on chemical etching of silicon wafers and is a simple and cost-effective method, although removing the silicon nanowires from the substrate without breaking them has proven to be a technical challenge. [25] Bottom-up methods include chemical vapor deposition (CVD), annealing in reactive atmosphere, SiO evaporation, molecular beam epitaxy (MBE), laser ablation (LA) and solution-based growth, with CVD as the most applied technique. [51]

Bottom-up approaches to SiNW synthesis are based on the vapor-liquid-solid (VLS) mechanism. This mechanism was first proposed by Wagner and Ellis in 1964, [52] and is a way of understanding how SiNW are grown. The name VLS comes from the pathway of silicon during the nanowire synthesis, going from vapor state, through liquid state and ending up as a solid wire. Wagner and Ellis identified metal impurities as necessary for the growth of silicon wires, and they observed that the metal impurity was located at the tip of the wires. They proposed that the metal impurity must be a preferred sink or a catalyst towards growth of the silicon wires. [52] Although the metal impurity is described as a catalyst in most of the literature, it does not necessarily lower the activation energy of the decomposition of the precursor, it thus mainly acts as a seed. [52, 53] However, some works have reported varying activation energies when introducing metal impurities, indicating that they are also capable of having a catalytic effect on SiNW growth. [54, 55] The two terms "catalyst" and "seed" are used interchangeably in this report.

Figure 2.4.1 illustrates the steps of the VLS-mechanism. The added metal impurity must be able to form an alloy with silicon. Metal seeds with a eutectic point with silicon are selected, such that intermixing occurs when heating towards certain temperatures. [53] With a sufficient silicon amount in the system, a liquid alloy droplet is formed at the eutectic point upon heating. By then introducing more silicon (e.g. a gaseous SiH_4-precursor in the case of CVD), precursor molecules crack on the surface of the alloy droplets, making the alloy droplet supersaturated with silicon. The excess silicon then precipitates at the solid-liquid interface, giving rise to the growth of a silicon nanowire. [51, 56]

Chemical vapor deposition (CVD) gets its name from the silicon source, that the silicon is provided through a gaseous phase. Common precursors are silane (SiH_4)

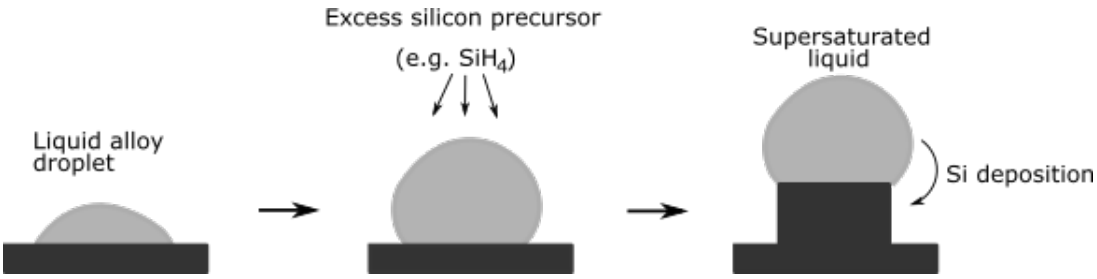

Figure 2.4.1: Illustration of the vapor-liquid-solid mechanism for silicon nanowire growth. As excess silicon makes the liquid alloy droplet supersaturated with silicon, it precipates a Si-rich solid phase leading to the growth of a silicon wire.

and silicon tetrachloride ($SiCl_4$), although they have significant safety issues. Silane decomposes from 350 °C, and can hence be cracked at the catalyst surface to give silicon and hydrogen. [56] CVD experiments can be performed in cylindrical hot-wall reactors to achieve the temperatures needed for precursor decomposition and the eutectic reaction to make a liquid alloy droplet of the catalyst and silicon. As silicon oxidizes easily when exposed to oxygen at higher temperatures, bringing the reactor to lower pressures before the growth reduces the amount of unwanted impurities and also helps SiNWs grow at lower temperatures. [51, 57]

The safety and practical issues with handling silane makes a demand for other silicon precursors. Lee et. al. [58] used phenylsilane and diphenylsilane to obtain an effective growth of silicon nanowires. Phenylsilane and diphenylsilane are liquids at room temperature and the organic part of the molecule stabilizes the compound towards air and water. Oreganosilanes are thus easier to handle than silane, and according to the reaction mechanism from diphenylsilane to silicon nanowire with gold catalyst proposed by Lee et. al. showed in Equation (2.4.1), silane is generated *in-situ* upon heating of the reactor, and can then act as a silicon precursor for the growth of silicon nanowires. [58]

$$\begin{aligned} 2\mathrm{SiPh_2H_2} &\longrightarrow \mathrm{SiPh_3H} + \mathrm{SiPhH_3} \\ \mathrm{SiPh_2H_2} + \mathrm{SiPhH_3} &\longrightarrow \mathrm{SiPh_3H} + \mathrm{SiH_4} \\ \mathrm{SiH_4} + \mathrm{Au} &\longrightarrow 2\,\mathrm{H_2} + \mathrm{Si/Au} \\ \mathrm{Si/Au} &\longrightarrow \mathrm{Si/NW} \\ \text{Total: } 2\,\mathrm{SiPh_2H_2} &\longrightarrow \mathrm{SiPh_4} + 2\,\mathrm{H_2} + \mathrm{Si/NW} \end{aligned} \tag{2.4.1}$$

In the first step, there is a disproportionation of diphenylsilane to monophenylsilane [59], before silane is formed in the second step. Then silane cracks on the catalyst

surface, which is gold in this example. In the fourth step, silicon precipitates as a wire from the supersaturated alloy droplet. The reaction equation shows that only 50% of the initially introduced Si is available for SiNW growth, a cost for safe handling. An interesting property that has been observed when using diphenylsilane as precursor for silicon nanowire synthesis is that the nanowires got covered in a thin organic surface layer consisting of phenyl groups, giving the nanowires a hydrophobic behavior. [60]

Silicon precursors with a higher amount of Si atoms per molecule tend to give a higher yield of silicon nanowires during CVD synthesis, according to Lu et al. [61] Between trisilane, iso/neo-pentasilane and cyclohexasilane (CHS), the latter gave the highest yield at almost 64%. They put this down to a ring-opening process, forming silylene intermediates which are highly reactive and easily captured by metal seeds for VLS growth.

2.4.2 Catalysts for silicon nanowire growth

Gold is the most used catalyst for growth of silicon nanowires in literature. It is a commonly used metal for electronic contacts, so it has a good availability, and gold colloid nanoparticles are widely produced for biomedical tests. [56] Gold is non-toxic and chemically stable, and when using it as catalyst for nanowire growth it is an advantage that it retains its purity by not oxidizing easily in air. [51] Figure 2.4.2a shows the phase diagram between gold and silicon. The eutectic point at 363 °C is at around 700 °C and 1000 °C below the melting points of pure gold and silicon, respectively. This is beneficial for the formation of a liquid alloy droplet needed for the VLS growth mechanism because the alloy melts at much lower temperature than the pure elements. A composition of 19 at% silicon at the eutectic shows that the silicon and gold mixture is favorable. With a high silicon amount in the eutectic, a lower pressure of silicon precursor is needed to force the silicon into the droplet for precipitation of a silicon wire. [51] As the droplet gets saturated with silicon, it will try to reduce its silicon concentration by precipitating a Si-rich solid. Since pure silicon is the closest phase boundary on the Si-rich side of the diagram, the precipitated wire is made of pure silicon. [56]

Figure 2.4.2b shows the phase diagram between silicon and tin, a cheaper alternative catalyst for silicon nanowire growth than gold. Similar to gold, tin also has an eutectic point with silicon, but at a lower temperature. The Sn-Si eutectic at 232 °C means that wire growth can happen at lower temperatures. At the same time, the eutectic has a low silicon fraction at less than 1%, which indicates that a higher silicon precursor pressure is needed to get silicon saturation of the Sn-Si alloy catalyst

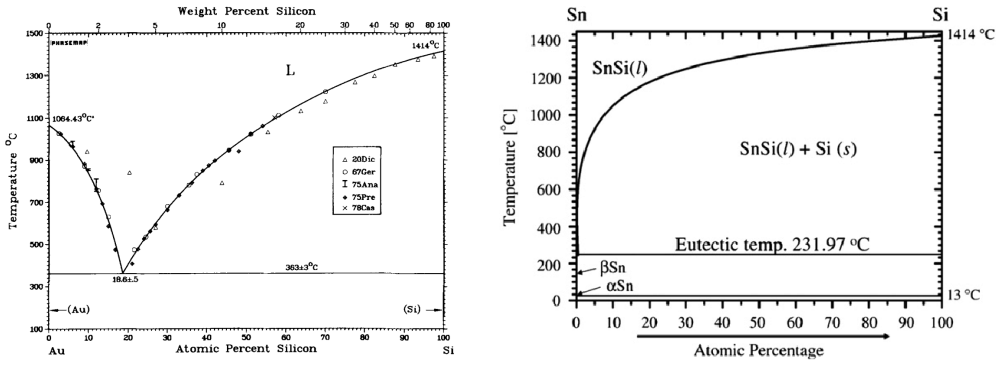

(a) (b)

Figure 2.4.2: Phase diagrams for (a) gold and silicon, adopted from [62] and (b) tin and silicon, adopted from [63].

droplets. [51] Nebolsin et al. [64] proposed that a low surface tension of droplets from elements like Sn, Ga, In and Bi could be detrimental for their ability to catalyze silicon nanowire growth. Despite the problem of a low surface tension, successful efforts to grow silicon nanowires from tin catalysts have been made. [65, 66] Tin is being researched as a possible anode material due to its ability to reversibly form alloys with lithium. Thus, using tin as catalyst can improve specific capacity compared to using catalysts that are inactive in the electrode reaction with Li. [67]

Tin metal particles, Sn(0), oxidize spontaneously in contact with air. [68] Hence, to obtain wire growth through the Sn-Si eutectic, tin particles need to either be protected from oxygen before reaction. Alternatively, tin particles can be generated *in-situ*. [69]

2.4.3 Cycling stability of silicon nanowires

As mentioned in Section 2.3.5, nanostructuration of silicon anodes is a way of avoiding failure due to the repeated volume expansions of silicon during cycling. Figure 2.4.3 illustrates the benefit of using nanowire anodes, and how their radial expansion during cycling can prevent fracture of the material [27]. By using *in-situ* transmission electron mictroscopy, a diameter of 300 nm has been identified as the critical value where larger nanowires lead to fracture. [70] Even though large volume changes in the material occur, only small stresses are created due to a fast lithium diffusion into the nanowires of smaller size. Through a mechanical numerical model, Ma et al. [71] predicted a critical size of 70 nm for silicon nanowires, and other studies proposed 30 nm as an ideal diameter for silicon nanowires in batteries. [72] Keller et al. [73] published a paper on the size effects of silicon nanoparticles and nanowires on their performance in lithium ion batteries, where small diameter nanowires (9 nm) saw the

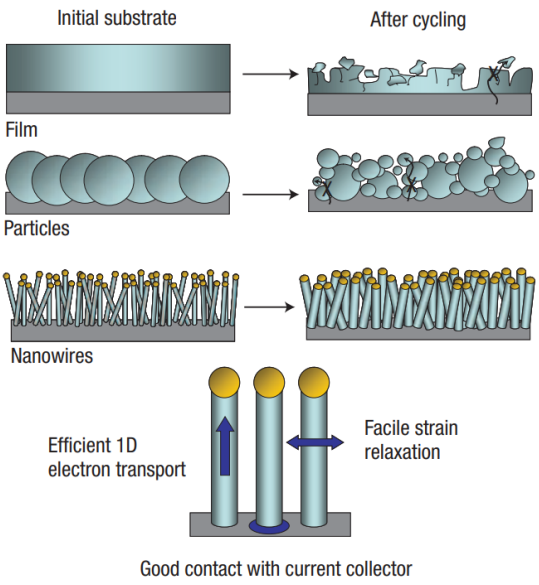

Figure 2.4.3: How cycling effects the structure of film-, particle- and nanowire-based silicon anodes. While film- and particle- based anodes experience pulverization and cracking of the material during cycling, the radial expansion of silicon nanowires helps avoiding the detrimental effects of silicon volume change during lithiation. Adopted from [27].

highest Coulombic efficiency and the best cycling stability compared to wires with 42 and 55 nm diameters, likely because of a fast Li^+ diffusion in the material. At the same time, they observed a linear increase in irreversible capacity loss with increasing specific area, indicating the formation of a similar SEI-layer independent of the silicon size giving a decrease in first Coulombic efficiency for smaller diameters.

2.4.4 Oxides in silicon nanowires

Silicon oxides (SiO, SiO_2, SiO_x) are viewed as promising anode materials, with many of the same strengths as anodes based on pure silicon. Yang et al. [74] did a study varying the oxygen content of SiO_x anodes, observing a high specific capacity of $1600\,mA\,h\,g^{-1}$ for $SiO_{0.8}$. They saw a decreasing capacity for increasing oxygen content, but at the same time a significantly improved cyclability when testing $SiO_{1.1}$ in comparison to $SiO_{0.8}$ and SiO. During the first lithiation of SiO, several lithium silicates are formed (Li_4SiO_4, $Li_2Si_2O_5$, $Li_6Si_2O_7$, Li_2SiO_3), in addition to Li_2O. [75] While the lithiation and delithiation of Li_xSi-alloys is reversible, lithium silicates and Li_2O are irreversible phases, causing buildup of the SEI-layer. These irreversible phases act as a buffer towards the strong volume expansion of silicon-based anodes during lithiation/delithiation, and could be an explanation to the improved cyclability

of SiO_x anodes with high oxygen contents. [75]

When it comes to nanowires of silicon, several studies have investigated the effect of oxygen on cycling performance. McDowell et al. [76] studied the impact of surface oxides on the volume expansion of silicon nanowires with various wire diameters through ex-situ TEM before and after lithiation. They found less volume expansion of silicon nanowires during cycling when an oxide layer was present, especially for nanowires with diameters of less than 50 nm. At the same time, the oxide layer leads to decreased first Coulombic efficiency and lower specific capacity.

Chen et al. [77] also reported a stabilizing oxide surface layer on silicon nanowires. The thin ($\approx$ 3 nm) surface layer consisting of mostly SiO_2 gave an average capacity drop of 0.04% per cycle over 560 cycles. They propose the oxide coating having a constraining effect on the silicon volume changes as the main reason behind the improved cyclability, avoiding pulverization issues in the electrode.

2.4.5 Efforts on carbon-silicon composite anodes

To exploit the high specific capacity of silicon without the cyclability-issues of pure silicon anodes, composites of graphite and silicon can be made. This way, carbon can provide electronically conducting networks and acts as a buffer against the volume expansion of silicon. Si/C composites can be sorted by the silicon structure, if it is 0D (nanoparticles), 1D (nanowires, nanotubes), 2D (nanosheets, thin films) or 3D porous silicon. [78]

Through a one-pot synthesis method, Karuppiah et al. [33] prepared silicon nanowires grown directly on graphite to create a composite anode with 32 wt% Si. The composite showed a specific capacity of $900\,\mathrm{mA\,h\,g^{-1}}$ and 72% capacity retention at 300 cycles, with graphite providing high electronic conductivity and accomodating silicon volume changes during cycling. Efforts to create composites with silicon nanowires and carbon nanotubes have also given a high specific capacity of $1500\,\mathrm{mA\,h\,g^{-1}}$ for 30 cycles. [79] Silicon nanolayer-embedded graphite/carbon has also been studied, giving a capacity retention of 96% after 100 cycles and a higher energy density in a full-cell system than with commercial graphite anodes. [80] More than 84% capacity retention over 300 cycles in a full cell was obtained by Li et al. [81] by using porous Si/C composite anodes.

2.5 Characterization

2.5.1 Scanning electron microscopy and Energy dispersive X-ray spectrometry

Scanning electron microscopy (SEM) exploits electrons' interactions with atoms to characterize materials. SEM can be used to obtain information about the chemical composition of samples, as well as imaging with resolutions between 1 µm to 1 nm depending on the instrument. [82] In a SEM, electrons are accelerated towards the sample by an applied voltage between 2 and 40 keV.

Multiple detectable signals result from the interaction between the electrons and the atoms in the sample, with the most prominent being secondary electrons, backscattered electrons and characteristic X-rays. [83] Secondary electrons arise from the ionization of specimen atoms close to the sample surface, with low energy (3-5 eV) electrons getting emitted. Secondary electrons are used for topographic imaging of samples, giving high resolution images of the sample surface. Backscattered electrons come from the interaction of incident electrons with atomic nuclei, getting scattered back out from the sample surface. These interactions come from deeper in the sample, with electrons of energies above 50 eV. Backscattered electrons give atomic contrast due to heavier elements giving stronger interactions between incident electrons and the atom nuclei. Therefore, backscattered electrons are useful for investigating the chemical composition of samples. [82, 83]

Energy dispersive X-ray spectroscopy (EDX) is an attachment to SEM for chemical composition analysis, making use of the characteristic X-ray signals from the sample. Characteristic X-rays are emitted when an incident electron knocks out an inner-shell electron, causing an outer-shell electron to move into the resulting empty slot and releasing energy in the form of X-rays. Electrons in higher energy shells will also jump to lower energy levels, each emitting characteristic X-rays. The EDX detector is then able to obtain information about the chemical composition of the sample through detection of the resulting X-rays with a penetration debth of 10-100 µm. [82] Using proper modeling of dense samples, EDX can give a quantitative analysis of the elemental composition in elements heavier than boron.

2.5.2 X-ray photoelectron Spectroscopy

X-ray photoelectron spectroscopy (XPS) is a technique for chemical analysis of the surface of materials. The analysis is conducted by irradiating the sample with monoenergetic soft X-rays and analyzing the emitted electrons from the photoelectric effect. A limited penetration power of the X-rays (1-10 nm), in addition to a low mean free path of electrons in solids means that only information about the surface of the sample is obtained.

The energy of the electrons emitted when X-rays hit the sample surface can be written as:

$$E_k = h\nu - E_b - \phi_s, \tag{2.5.1}$$

where E_k is kinetic energy, $h\nu$ is the energy of the incoming photon, E_b is the binding energy of the atomic orbital of the electron and ϕ_s is the spectrometer work function. The spectrometer work function is instrument-dependent and assumed constant. Because the incoming energy is calculated from the wavelength of the X-rays, and the kinetic energy is measured, the binding energy of the emitted electrons can be determined. Every element has a certain set of binding energies, thus the chemical composition and quantities of the elements in the surface can be determined. One of the main advantages with XPS is that it can distinguish energies for one element in various chemical environments due to a high resolution in energy, which means that information of the oxidation state of elements is obtained. [84]

2.5.3 Nuclear magnetic resonance spectroscopy

Nuclear magnetic resonance (NMR) spectroscopy is a characterization method based on the magnetic activity of atomic nuclei. Protons and neutrons in the nuclei are characterized by a nuclear spin quantum number (m) which takes the value of $1/2$ or $-1/2$ depending on their magnetic behavior. The magnetic characteristics of an atomic nuclei is hence described by the combined spin quantum number of protons and neutrons, the nuclear spin (I). When all opposite m are paired, $I = 0$, and the nuclei only has one spin state. Such nuclei are defined as magnetically inactive, and will not be directly detected during NMR-spectroscopy. [85]

Hydrogen is an example of an atom with a non-zero nuclear spin, having two different spin states (+1/2 and -1/2). These states are usually degenerate, but their energy levels split when the nuclei is exposed to an external magnetic field. The nuclei can thus exist in two different stationary states, and transitions between these

states can be triggered by a radiofrequency transmitter. The energy absorption is then detected by a radiofrequency detector, and recorded as a resonance signal. [86]

For a molecule containing multiple hydrogen atoms (or other atoms with non-zero nuclear spin, e.g. ^{19}F, ^{13}C or ^{15}N), a spectrum can be made based on the resonance signals given by the atomic nuclei because nuclei in different chemical environments give rise to different signals, separated by a *chemical shift*. The resonance signals have two important properties: 1) The area under the resonance signals is proportional to the number of atoms that create the signals. 2) Resonance signals are not all singlets, some peaks can be split into multiplets due to spin-spin coupling, internucleic magnetic interactions. Due these characteristic resonance signals, the structure of unknown molecules as well as their quantitative composition can be described. [86]

Doing NMR spectroscopy on solid samples can give wide peaks due to band broadening coming from anisotropic interactions, which leads to low resolution and loss of information compared to liquid state NMR. By Magic Angle Spinning (MAS) NMR spectroscopy, a solid sample is spun rapidly along its axis during data aquisition by a gas-driven turbine in a 54.74° angle to the magnetic field, to imitate the free movement and isotropic motion of molecules in a liquid. The magic angle spinning of the sample improves resolution due to a complete or partial averaging of the anisotropy of nuclear interactions depending on the spinning frequency, allowing for high resolution signals also for solid state samples. [87]

2.5.4 Cycling of Si anodes in half-cell configuration

When a silicon electrode gets placed in a coin cell opposite to a lithium metal electrode (a so-called "half-cell" configuration), the low electrochemical potential of the Li electrode makes silicon act as the positive electrode. When put into a battery against a regular cathode material, e.g. $LiFePO_4$, lithium ions move from the cathode to the anode during the first charge of the battery, causing a lithiation of the anode. When testing silicon anode materials in half-cell configuration, the battery is therefore first discharged (applying negative current) to simulate the lithiation of silicon that would happen during the first cycle of a full cell.

A common representation of battery cycling data is plotting the cell voltage versus specific capacity during both charge and discharge, e.g. as in Figure 2.5.1a, which shows the first cycle for a graphite-silicon composite anode in a half-cell. Two separate curves are shown for the charge and discharge of the battery, causing delithiation and lithiation of the anode, respectively. This representation allows for comparing the capacities upon charge and discharge of the battery.

Plateaus in the curve of voltage versus capacity (Figure 2.5.1a) indicates electrochemical reactions taking place at certain voltages which increases the amount of charge stored in the battery. By evaluating the charge added to the battery per voltage change, and plotting against the cell voltage, the plateaus in Figure 2.5.1a appear as peaks in the plot of differential capacity, shown in Figure 2.5.1b. This way, plots of dQ/dE versus voltage can help identifying which anode phases get created during cycling of the battery.

Silicon anodes form various Li_xSi_y-alloys during lithiation at close to 0.1 V, [33] which gives a plateau in Figure 2.5.1a and peak 2 in Figure 2.5.1b at this voltage. Graphite lithiates at similar voltages, and contributes to the same peak at 0.1 V. [88] The lithiation peak at less than 50 mV (peak 1) is normally attributed to lithiation of the crystalline phase $Li_{15}Si_4$, with a corresponding prominent peak at 0.45 V (peak 6) for delithiation of the same phase. [89] The three peaks between 0.1 and 0.25 V (peaks 3, 4, 5) in the delithiation curve are characteristic for graphite delithiation. [88]

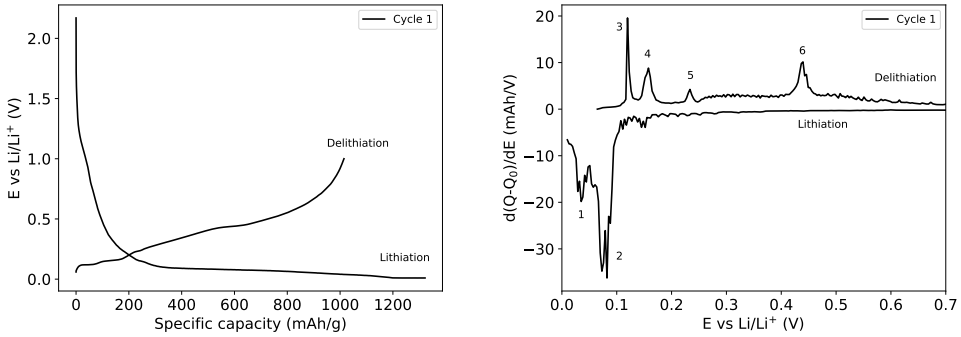

(a) (b)

Figure 2.5.1: Two ways of representing battery cycling data, with the voltage as a function of capacity in (a) and differential capacity versus voltage in (b). The two subfigures show first cycle data from a graphite-silicon composite anode in a half-cell configuration, with the lithiation and delithiation curves indicated in the figures.

Chapter 3

Experimental

3.1 Overview

The experimental work of this study can be divided in two main parts: 1) SnO_2 and SnS as tin seeds for synthesis of graphite-silicon nanowire (Gt-SiNW) composite anodes, and 2) Cyclohexasilane (CHS) as a new silicon precursor for VLS-growth of Si nanowires. A brief overview of the experimental procedure for each part is shown in Figure 3.1.1 and Figure 3.1.2 for tin catalysts and for CHS as precursor, respectively, before a full description of the experimental work in the following sections.

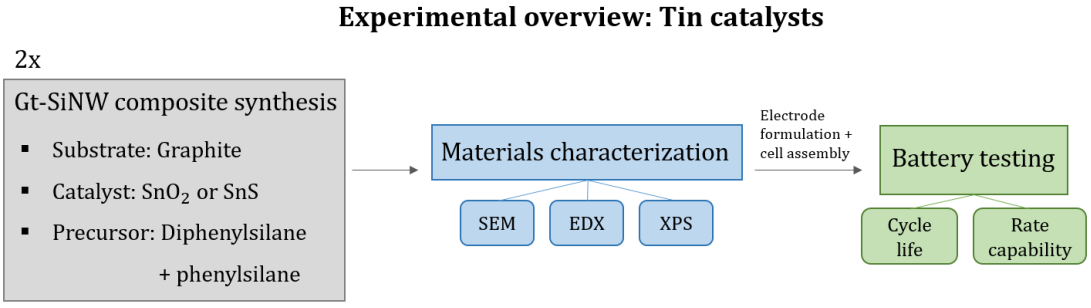

Figure 3.1.1: Simplified chart showing the main experimental steps for the study of SnO_2 and SnS for Gt-SiNW composite anodes.

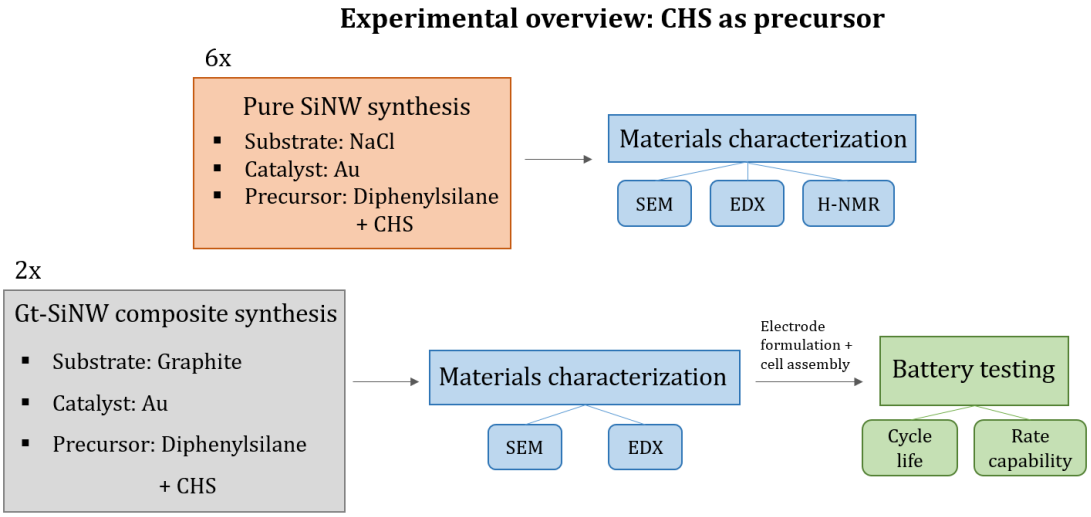

Figure 3.1.2: Simplified chart showing the main experimental steps for the study of cyclohexasilane as a precursor for SiNW growth.

3.2 Catalyst preparation

Gold

A dispersion of gold nanoparticles in chloroform was ready for use in the lab, previously made by following Brust's method. [90] By this method, $HAuCl_4 \cdot 3H_2O$ was dissolved in water before tetraoctylammonium bromide was used as a phase-transfer reagent to transfer $AuCl_4^-$ from aqueous solution to toluene. $AuCl_4^-$ then got reduced by $NaBH_4$ and stabilized with dodecanethiol. This gave gold nanoparticles with diameters of 1-3 nm, which were purified by precipitation in ethanol and then dispersed in chloroform to achieve a gold concentration of 43 mg/mL.

Tin oxide

Tin(IV) oxide (SnO_2) particles used as catalyst for silicon nanowire growth were a 15 wt% collodial dispersion in water, bought from Alfa Aesar.

Tin sulfide

SnS nanocrystals were synthesized by a similar method to the procedure of de Kergommeaux et al. [91] All chemicals were stored in an Argon-filled glove box with oxygen and water levels of less than 1 ppm. 380 mg $SnCl_2$, 5 mL octadecane, 3 mL trioctylphosphine and 4.5 mL oleic acid was added to a 100 mL conical flask (solution A). 75 mg thioacetamide, 5 mL oleyamine and 3 mL trioctylphosphine was added to a glass vial (solution B). The containers were sealed and transported to a fume hood.

A Schlenk line was used to limit the solutions exposure to air. The system was dried by connecting a conical flask to the Schlenk line, applying vacuum and then an argon flow for 5 minutes. The conical flask with solution A was then connected and degassed under vacuum for 1 hour at 60 °C, heated by an oil bath.

After degassing, argon flow was applied to both solutions A and B, and the temperature of the oil bath was increased to 120 °C. When 120 °C was reached, solution B was added to solution A quickly by using a syringe. The solution was left for exactly 5 minutes under fast stirring, before being immediately transferred to an ice bath.

The product was then cleaned by dissolving in 10 mL chloroform, and diluted in 20 mL ethanol to precipitate the SnS nanocrystals. The solution was then centrifuged for 3 minutes at 5000 rpm. This step was repeated twice. The resulting precipitate was dispersed in 10 mL chloroform and stored in a glass vial. To find the concentration of the solution, 100 µL was transferred to an open vial, and the chloroform was allowed to evaporate. The vial was then weighed to determine the weight of the remaining particles and thus the concentration of the created dispersion in mg/mL.

3.3 Silicon nanowire syntheses

3.3.1 Tin oxide and tin sulfide as catalysts

Silicon nanowires were grown directly on a graphite substrate to make Gt-SiNW composites through a one-pot synthesis method. The composites were synthesized by the use of two different tin seeds: SnO_2 and SnS. These two composites will be referred to as Gt-SnO_2-SiNW and Gt-SnS-SiNW from this point. The composites were not synthesized at the same time, but in series.

For the growth using SnO_2, 800 mg of graphite was mixed with 0.925 mL (160 mg) 15 wt% SnO_2 dispersed in water. This was grinded in a pre-heated mortar at 80 °C. Ethanol was added for improved mixing, and the mortar was placed on a heating plate at 100 °C to evaporate the solvents. The Gt-SnS substrate was prepared in a similar way, by mixing 800 mg graphite with 7.1 mL (100 mg) SnS in chloroform. No extra solvent was needed for mixing, due to the high volume of chloroform added with the SnS-solution.

When dry, the grinded substrate of graphite and SnO_2 or SnS was transferred to a crucible, and put in a stainless steel cylindrical reactor (imaged in Figure 3.3.1) with a volume of 300 mL. The crucible was covered with a lid, and 6 mL phenylsilane and 14 mL diphenylsilane was added to the bottom of the reactor. The reactor was

then sealed, and cleaned from air by five argon/vacuum cycles, before leaving it under vacuum, reaching a pressure of 30-40 mbar.

The reactor was heated to 380 °C, reaching target temperature within 30 minutes. The temperature was kept constant at 380 °C for five hours. After letting the reactor cool down, the product was cleaned in a Büchner filtration system by rinsing twice in 200 mL ethanol, then five times with 50 mL dichloromethane, then once with 200 mL ethanol. The product was then dried on a 100 °C heating plate for at least 15 minutes and stored in a glass vial.

Figure 3.3.1: The stainless steel reactor used for synthesis of silicon nanowires.

3.3.2 Cyclohexasilane as precursor

A series of 8 silicon nanowire growths were conducted to study the use of cyclohexasilane (CHS) as silicon precursor. Both pure CHS, pure diphenylsilane and mixtures with different molar ratios of CHS and diphenylsilane were used. NaCl was used as the substrate for the first 6 growths, as it can be washed away with water such that only the silicon product remains. Two growths were also conducted using graphite as substrate, with 46% and 100% CHS in the precursor. The two graphite-samples will be referred to as Gt-CHS46 and Gt-CHS100.

For all the CHS-based syntheses, gold nanoparticles (AuNPs) was used as catalyst. The gold was stored as a dispersion in chloroform, with a concentration of 43 mg mL^{-1}. To prepare the substrate for synthesis of pure nanowires, 5 g NaCl was mixed with 350 µL (15 mg) AuNP-solution in a hot mortar (80 °C), using 1:9 octadecane/hexane as solvent to ease the mixing. When using a graphite substrate, 680 mg and 700 mg graphite was used for Gt-CHS46 and Gt-CHS100, respectively, to optimize the growth for obtaining 20-25 wt% Si in the final composite. When dry, the grinded powder was transferred to a crucible and put inside a cylindrical stainless steel reactor with an inner volume of 75 mL. The reactor was then sealed and transferred to an argon-filled glove box with oxygen and water contents of less than 1 ppm.

Cyclohexasilane needs to be handled in an oxygen-free environment, as it combusts spontaneously in air. Thus, for the syntheses with CHS as a part of the precursor mix, the silicon precursors were added to the reactor inside the glove box. The desired amount of diphenylsilane was put under vacuum before being placed into the glovebox. The silicon precursors were introduced to the reactor by fitting a plastic tube through the reactor column valve, and adding the precursors with a syringe. The amount of precursor added for each synthesis is listed in Table 3.3.1. The experiments were designed such that the total added molar amount of silicon was constant at 21 mmol over all experiments.

After filling it with precursors, the reactor was heated to 430 °C for 2.5 hours. When cool, the reactor was opened and the product in the crucible was cleaned in a Büchner filtration system. If using NaCl as substrate, the product was rinsed twice in 100 mL dichloromethane, 10-15 times in 50 mL water and twice in 100 mL aceton. When using a graphite substrate, the product was rinsed using only 5x50 mL dichloromethane and 2x100 mL aceton. The remaining product was then dried at a 120 °C heating plate and stored in a glass vial.

Table 3.3.1: Quantities of precursors added to each synthesis of pure silicon nanowires in the study of CHS as a precursor for nanowire growth.

Sample	Diphenylsilane (µL)	CHS (µL)
0% CHS	3900	0
23% CHS	3000	150
46% CHS	2100	300
54% CHS	1800	350
77% CHS	900	500
100% CHS	0	650

3.4 Materials characterization

This section is dedicated to characterization of the products from the silicon nanowire growths, both for verifying the quality of the products in terms of silicon content, wire growth and purity, and for investigating the chemical composition of the samples.

3.4.1 SEM and EDX

A Zeiss Ultra 55 scanning electron microscope was used for imaging of the synthesized Gt-SiNW composites. A thin layer of powder was stuck directly on carbon tape to fix it on the sample holder. An accelerating voltage of 5 kV, working distance of 5 mm, aperture size of 30 µm and the InLens-detector was used to obtain high-resolution images of the samples.

For quantitative analysis of the samples through EDX, high-density pellets were made in a Specac manual hydraulic press, applying a pressure of 2 tonnes for one minute. Aperture size in the SEM was adjusted to 60 µm, the accelerating voltage to 10 kV and the working distance was kept at 7 mm. A SiC wafer was used as a reference to refer to a previous calibration of the EDX instrument with multi-element calibrants.

EDX spectroscopy was conducted on all syntheses of both pure silicon nanowire samples and Gt-SiNW composites. A quantitative analysis of each sample was made, through scans of wide zones ($\approx$ 0.5-1 mm²) to get an overview of the overall composition.

For the Gt-SiNW composites grown using tin catalysts (Gt-SnO_2-SiNW and Gt-SnS-SiNW), scans of narrow areas ($\approx$ 50-100 µm²) were made to obtain information about local differences in composition.

SEM images with high magnification (50K-200K X) were used to measure the size of silicon nanowires for the Gt-SnO_2-SiNW and Gt-SnS-SiNW samples. The wire diameters were measured manually with the software ImageJ, and at least 400 measurements was done for each sample to obtain the wire diameter distributions.

3.4.2 X-ray Photoelectron Spectroscopy

The samples used for XPS were prepared in the same way as the samples for EDX, by pressing the 2 mg of powder into a dense pellet by applying 2 tonnes in a Specac manual hydraulic press. The pellets were stuck to carbon tape and placed on a sample holder.

A Versa Probe II spectrometer (ULVAC-PHI) was used for the XPS analyses, equipped with a monochromated Al K_α source. Adventitious carbon (C 1s binding energy of 284.8 eV) was used as a reference for binding energies. A constant pass energy of 23.3 eV was used for recording of the core-level peaks.

3.4.3 Magic angle spinning H-NMR

Magic angle spinning ^{1}H-NMR was conducted on three SiNW syntheses with 0% CHS, 23% CHS and 100% CHS as precursor. Sample preparation consisted of packing 1.3 mm-diameter rotors with 1.8, 1.8 and 2.4 mg SiNW powder for 100% CHS, 23% CHS and 0% CHS, respectively, so that the samples were as dense as possible. Prior to data aquisition, the samples were dried overnight in an 80 °C oven. The ^{1}H-NMR measurements were made with a magnetic field strength of 4.7 T and a MAS frequency of 40 kHz. 512 scans were made for each sample, with a Hahn echo pulse sequence.

3.5 Battery manufacture

Only the silicon nanowire growths on graphite substrates were used for electrode formulation and battery tests, always following the same steps. This section describes the procedure of producing electrodes from the Gt-SiNW active material, coin cell assembly and the specifications of battery testing procedures.

3.5.1 Electrode formulation

All electrode inks were formulated with a composition of 80 wt% Gt-SiNW active material, 10 wt% carbon black super-P as conductive additive and 10 wt% carboxylmethyl cellulose (CMC) binder. A similar active material loading between the electrodes was necessary, and the targeted loading was reached by a trial-and-error method where the viscosity of each slurry was adjusted by adding distilled water droplets. The electrodes were made by the following steps:

1. 400 mg Gt-SiNW composite and 50 mg carbon black super-P was mixed in mortar using cyclohexane as solvent. When dry, it was put into a 10 mL beaker.
2. 1667 mg 3 wt% CMC diluted in distilled water was added. A certain amount of water droplets was added to adjust the viscosity of the slurry (see quantities in Table 3.5.1).
3. The slurry was mixed in a Dispermat mixer for 10 minutes at 2000 rpm.
4. Half of the slurry was tape casted onto a copper foil, using a doctor blade height of 100 µm.
5. Steps 3 and 4 were repeated after adding extra water to make two electrodes with different loadings.
6. The resulting inks were dried in an oven at 70 °C for at least 12 hours.
7. From each dry ink, 14 mm diameter discs were cut and calendered with the power of 1 tonne in a Specac hydraulic press.
8. The calendered discs were dried under vacuum at 80 °C for at least 48 hours before being transferred to a glove box for coin cell assembly.

Table 3.5.1: The number of water droplets added to each slurry, represented by the number added to the original slurry + the number added to the second half of the slurry. The electrodes presented are only those that would later get used for coin cell assembly and electrochemical tests.

Active material	Number of water droplets
Gt-SnO_2-SiNW	20
Gt-SnS-SiNW	20+16
Gt-CHS46	20+8
Gt-CHS100	20+8

3.5.2 Coin cell fabrication

CR2032 cells with an electrolyte of 1M $LiPF_6$ in 1:1 DEC and EC (vol%) with 2 wt% vinylenecarbonate 10 wt% fluorethylene carbonate were assembled in an argon-filled glove box with water and oxygen content of less than 1 ppm. Lithium metal foil with a diameter of 16 mm was used as a reference and counter electrode, and the separator was a Celgard 2400 polypropylene separator.

The coin cells were assembled in the following order: Bottom cap, plastic joint, 0.5 mm thick spacer, SiNW/Gt anode, Viledon porous filter, Celgard separator, 150 µL electrolyte, lithium foil connected to a 0.5 mm thick spacer, spring, top cap. Figure 3.5.1 illustrates the setup of the coin cells.

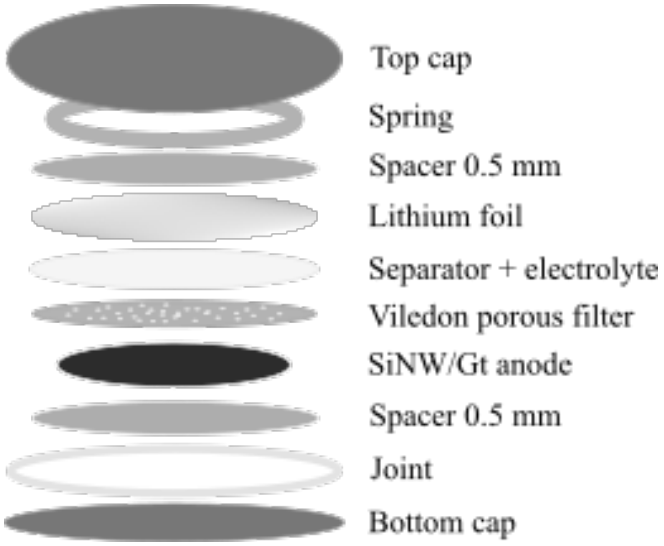

Figure 3.5.1: Illustration of the parts used in the CR2032 coin cells, and the order of which they were stacked.

3.5.3 Battery tests

Electrochemical testing of the constructed CR2032 coin cells was done in a Bio-Logic battery cycling system, through a galvanostatic cycling with potential limitation (GCPL) technique. Common for each procedure was a lower voltage limit of 0.010 V during discharge (negative current) and an upper limit of 1 V during charge (postitive current) of the battery. As the anode composites were tested in a half-cell configuration against lithium metal making the Gt-SiNW composites act as the positive electrode, the first cycle was started with a discharge step to simulate the lithiation of Gt-SiNW which would happen during the first charge of a full cell lithium ion battery.

To apply the correct current for cycling at different C-rates, a crude approximation of the Gt-SiNW electrodes' specific capacity was made based on the silicon content in the graphite. The specific capacity of a composite with 20-25 wt% Si was estimated to 1000 $\mathrm{mA\,h\,g^{-1}}$, and the C-rates were then calculated by using the active material mass of each electrode disc.

Long cycling

The applied settings for the long cycling program are described below:

1. Discharge at C/20 until lower voltage limit of 0.010 V is reached. Then the voltage is kept constant until a current limit correnspondingto a rate of C/100 is reached.
2. Charge at C/20 until the upper voltage limit of 1 V is reached. Then the cell is allowed to rest for 5 minutes without any applied current before the next discharge step.
3. The same procedure is followed, just with a current corresponding to a rate of C/5, and a current limit corresponding to C/50 during the constant voltage step.
4. Cycling at C/5 is repeated, with an upper limit of 300 cycles.

Rate performance

The rate performance of the formulated anode materials was tested through applying current to the cells corresponding to C-rates ranging from C/20 to 5C. The settings for the rate performance tests are described below:

1. Discharge at C/20 until lower voltage limit of 0.010 V is reached. Then the voltage is kept constant until a current limit correnspondingto a rate of C/100 is reached.
2. Charge at C/20 until the upper voltage limit of 1 V is reached. Then the cell is allowed to rest for 5 minutes without any applied current before the next discharge step.
3. The same steps are then repeated four times, giving a total of 5 cycles at C/20.
4. Five charge/discharge cycles at C/10 rate, and five cycles at C/5 are carried out, with the same setting except for a current limit corresponding to C/50.
5. Then five discharges at each rate of C/2, C, 2C, 5C with charge at C/5 was made.
6. Five cycles with charge and discharge at C/10 followed.
7. The procedure was finished with charging at C/5 and discharging at C for a maximum of 250 cycles.

Chapter 4

Results and discussion: Tin oxide and tin sulfide as catalysts

4.1 Results

4.1.1 Graphite-silicon nanowire composite synthesis

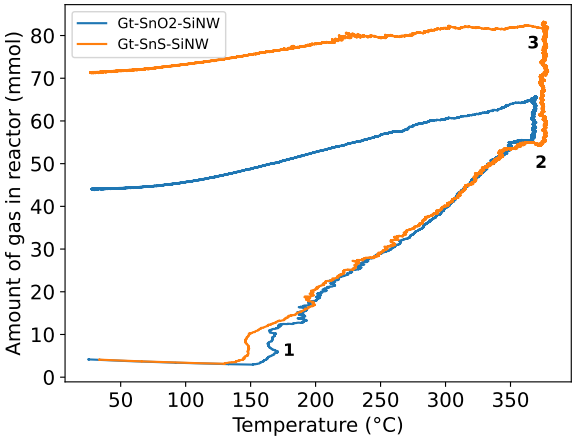

Figure 4.1.1: The amount of gas in the reactor during the syntheses of Gt-SnO_2-SiNW and Gt-SnS-SiNW, as a function of temperature. The gas amount was estimated by measuring the reactor pressure and using the ideal gas law.

The pressure evolution in the reactor as a function of temperature was used to calculate the amount of produced gas inside the reactor by use of the ideal gas law. The amount of gas in the reactor during synthesis of Gt-SnO_2-SiNW and Gt-SnS-SiNW is shown in Figure 4.1.1. The temperature was gradually increased until point 1 indicated on the figure, where the pressure started rising due to the formation of

gaseous products inside the reactor. The heating continued until point 2, where the temperature was kept constant until point 3. Then the heating was released and the reactor was allowed to cool down. The gas production during the two growths was similar, although during the synthesis of Gt-SnS-SiNW, the pressure in the reactor started increasing at a lower temperature than for the Gt-SnO_2-SiNW synthesis. The reactor was also heated for 30 extra minutes during the growth of Gt-SnS-SiNW, partly explaining why the gas production for that synthesis was higher at 380 °C.

4.1.2 Microstructure

Figure 4.1.2 shows SEM micrographs of the Gt-SnO_2-SiNW and Gt-SnS-SiNW composites. Micrometer-sized graphite grains covered in silicon nanowires were imaged in Figure 4.1.2a and Figure 4.1.2b. Graphite appeared in a matte, dark grey color, while silicon appeared brighter in the image due to a higher reflection of electrons. The silicon wires were more visible in Figure 4.1.2c and Figure 4.1.2d, showing a broad range of wire diameters. The catalyst particles were also observed on the tip of the wires as an expected result of the VLS growth mechanism. Even though two different tin catalysts were used for these two growths, there were no obvious differences in the microstructures of the resulting powders.

The distributions of wire diameters for Gt-SnO_2-SiNW and Gt-SnS-SiNW are shown in Figure 4.1.3a and 4.1.3b, respectively. Gt-SnO_2-SiNW had a more homogeneous size distribution, with a high amount of wires with diameters between 10 and 20 nm, and an average diameter of 27 nm. Gt-SnS-SiNW had more varied wire diameters, and an average diameter of 37 nm. The total amount of wires measured was 448 for Gt-SnO_2-SiNW and 442 for Gt-SnS-SiNW.

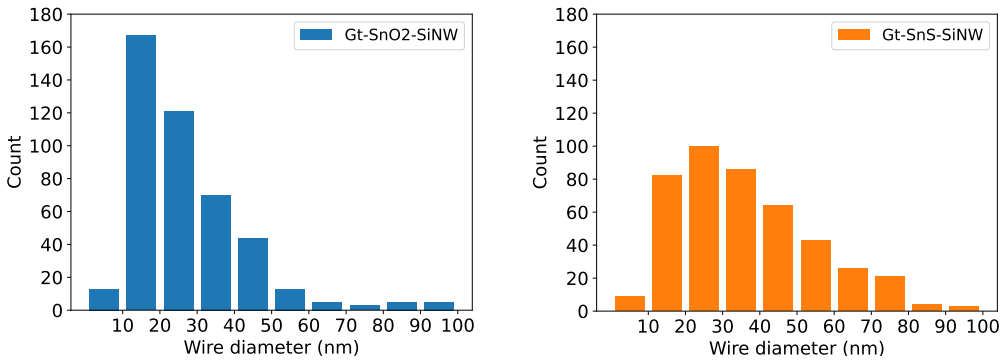

(a) (b)

Figure 4.1.3: Histrograms showing the distribution of wire diameters for Gt-SnO_2-SiNW (a) and Gt-SnS-SiNW (b).

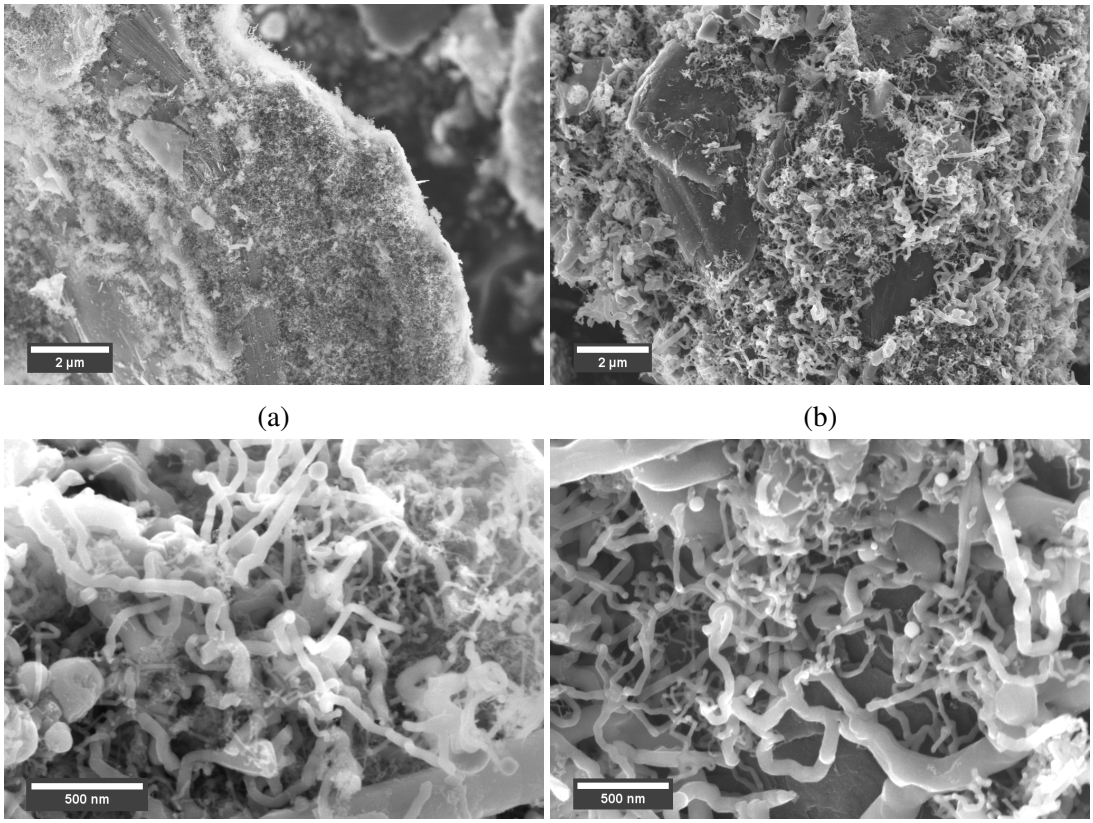

(a) (b)

(c) (d)

Figure 4.1.2: SEM micrographs showing both a global view of the graphite-silicon nanowire composites, as well as a closer look on the silicon wires. Gt-SnO_2-SiNW at different magnifications is shown in (a) and (c), while (b) and (d) show the Gt-SnS-SiNW sample.

4.1.3 Elemental composition and oxygen content

Energy dispersive X-ray analysis

EDX quantitative analysis by wide area scans gave the mass fractions of C, O, Si and Sn in Gt-SnO_2-SiNW and Gt-SnS-SiNW. The average mass fractions and their standard deviations are listed in Table 4.1.1. Gt-SnO_2-SiNW had an average silicon amount of 22.4%, while Gt-SnS-SiNW had an average silicon amount of 21.0%. The oxygen content was 2.3% and 1.3% for the SnO_2 and SnS catalysts, respectively. S and P were the main detected elements which are not listed in the table. Both samples contained close to 0.4% P as a contaminant from diphenylsilane, while 0.004% S was detected in Gt-SnO_2-SiNW and 0.01% S in Gt-SnS-SiNW. This amount of S was far below the amount of SnS added to the reactor, and it is assumed that S reacted with hydrogen to get expelled from the reactor as H_2S-gas.

Table 4.1.1: Average elemental composition of Gt-SnO_2-SiNW and Gt-SnS-SiNW based on mass. Obtained by quantitative EDX measurements.

Sample	C	O	Si	Sn
Gt-SnO_2-SiNW	69.3	2.3	22.4	5.2
Gt-SnS-SiNW	73.7	1.3	21.0	2.7

The results from narrow area scans of EDX quantitative analysis gave information about the local elemental composition throughout the surface of the samples. Local differences in composition gave information on the correlation between elements, if the amount of O in the sample increased with increasing Si concentration. The amount of oxygen in several narrow scans was hence plotted against the amount of silicon in the same scans to observe the correlation between these elements. Since the measured composition was given in percentages, a reference was needed to avoid bias. Hence, to obtain the correlation between Si and O, carbon was used as a reference through plotting the percentage of Si divided by the percentage of carbon (Si/C) versus the equivalent for oxygen (O/C). Four of these correlation plots from the narrow EDX scans are shown in Figure 4.1.4.

A plot of O/C vs Si/C for both Gt-SnO_2-SiNW and Gt-SnS-SiNW is shown in Figure 4.1.4a. There was a clear difference in the correlation between oxygen and silicon for the two samples, with an increase of oxygen with increasing silicon for Gt-SnO_2-SiNW, and no change of oxygen content in the Gt-SnS-SiNW sample with varying silicon amounts. The plot of O/C vs Sn/C in Figure 4.1.4b shows the similar trends for tin, with a constant oxygen amount upon an increase of tin for the SnS-sample and a clear correlation of oxygen and tin in the SnO_2-sample.

Figure 4.1.4c shows correlations between tin and silicon with a R^2-value close to 1.0, indicating a good spread of silicon across the tin seeds throughout the samples.

The intercepts with the vertical axis in Figure 4.1.4d are interpreted as a measure of the oxygen content when the carbon content decreases towards zero. The intercept of the curve for Gt-SnS-SiNW was very close to zero, while the intercept for Gt-SnO_2-SiNW had a significantly larger value, implying that oxygen was detected from other sources than carbon.

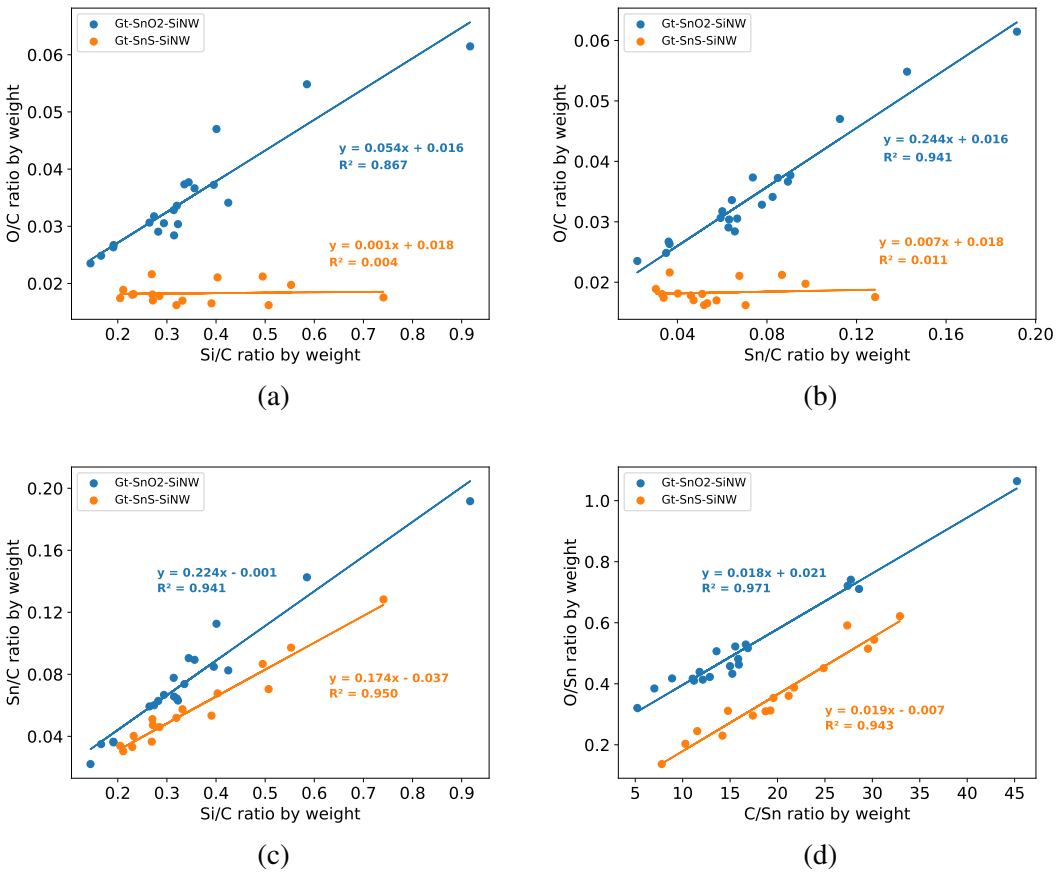

Figure 4.1.4: Correlations between elements based on plotting the weigth ratios of different components from quantitative EDX measurements. The four plots show oxygen versus silicon with carbon as referece in (a), oxygen versus tin with carbon as reference in (b), tin versus silicon with carbon as reference in (c) and oxygen versus carbon with tin as reference in (d).

As well as providing a visual representation of the correlation between the elements present in the samples, the correlation plots from EDX analysis were used to approximate maximum values for the oxygen to silicon ratio in the nanowires, $(O/Si)_{nw}$, and oxygen to tin ratio in the catalyst particles, $(O/Sn)_{cat}$. An example calculation for the determination of $(O/Si)_{nw}^{max}$ and $(O/Sn)_{cat}^{max}$ for the plot of O/C versus Si/C is shown below, and the full calculations in addition to the maximum values for all the plotted correlations can be found in Appendix A.1.

To estimate the maximum values for oxygen in the silicon nanowires and catalyst particles, an important assumption is that the only elements detectable from graphite is C and O, that the nanowires only consist of Si, C and O, and that the catalyst particles only consist of Sn and O. Equation (4.1.1) gives an overview of the expected elements to be found in graphite (gt), nanowires (nw) and catalyst particles (cat),

$$
\begin{aligned}
gt &= C_{gt} + O_{gt} \\
nw &= Si_{nw} + O_{nw} + C_{nw} \\
cat &= Sn_{cat} + O_{cat}.
\end{aligned}
\tag{4.1.1}
$$

The total oxygen to carbon ratio can be written as the sum of oxygen to carbon ratios from the different sources of oxygen as in Equation (4.1.2),

$$
(O/C)_{tot} = \frac{O_{gt}}{C_{tot}} + \frac{O_{cat}}{C_{tot}} + \frac{O_{nw}}{C_{tot}}, \tag{4.1.2}
$$

which can be rewritten to the expression in Equation (4.1.3):

$$
\begin{aligned}
(O/C)_{tot} &= \frac{(O/C)_{gt}}{1+(C_{nw}/C_{gt})} + (O/Sn)_{cat} * (Sn/Si)_{tot} * (Si/C)_{tot} + (O/Si)_{nw} * (Si/C)_{tot} \\
(O/C)_{tot} &= (Si/C)_{tot} * ((O/Sn)_{cat} * (Sn/Si)_{tot} + (O/Sn)_{nw}) + \frac{(O/C)_{gt}}{1+(C_{nw}/C_{gt})}.
\end{aligned}
\tag{4.1.3}
$$

From the final expression in Equation (4.1.3), the slope (b) and intercept with vertical axis (a) of the linear regression for the plot of O/C vs Si/C in Figure 4.1.4a can be expressed as in Equation (4.1.4),

$$
\begin{aligned}
(O/C)_{tot} &= (Si/C)_{tot} * a + b \\
a &= (O/Sn)_{cat} * (Sn/Si)_{tot} + (O/Si)_{nw}, \\
b &= \frac{(O/C)_{gt}}{1+(C_{nw}/C_{gt})} \approx (O/C)_{gt},
\end{aligned}
\tag{4.1.4}
$$

with the assumption that the amount of carbon in the nanowires is very low compared to the amount of carbon in graphite, such that $1+(C_{nw}/C_{gt}) \approx 1$. The numerical value of $(Sn/Si)_{tot}$ is obtained directly from the slope of the linear regression in Figure 4.1.4c because Si and Sn are only present from one source each (nanowires and catalyst particles, respectively). For Gt-SnO_2-SiNW, $(Sn/Si)_{tot} = 0.224$, while for Gt-SnS-SiNW, $(Sn/Si)_{tot} = 0.174$.

The numerical values of the slope and intercept with vertical axis can then be used to determine the maximum values of $(O/Si)_{nw}$ and $(O/Sn)_{cat}$. It is assumed that $(O/Si)_{nw}$ takes its maximum value when $(O/Sn)_{cat} = 0$ and vice versa. The standard

deviation in the slope and intercept is obtained from the regression error when using the least-squared linear regression method. For Gt-SnO_2-SiNW the numerical values are found in Equation (4.1.5):

$$\begin{aligned} b &\approx (O/C)_{gt} = 0.016 \pm 0.002 \\ a &= 0.054 \pm 0.005 = (O/Si)_{nw} + 0.224 * (O/Sn)_{cat} \\ &\underline{\Rightarrow (O/Si)_{nw} < 0.059, \;\; (O/Sn)_{cat} < 0.263,} \end{aligned} \tag{4.1.5}$$

while Equation (4.1.6) shows the numerical values for Gt-SnS-SiNW:

$$\begin{aligned} b &\approx (O/C)_{gt} = 0.018 \pm 0.001 \\ a &= 0.001 \pm 0.003 = (O/Si)_{nw} + 0.174 * (O/Sn)_{cat} \\ &\underline{\Rightarrow (O/Si)_{nw} < 0.004, \;\; (O/Sn)_{cat} < 0.023.} \end{aligned} \tag{4.1.6}$$

Thus, by using the numerical values of the linear regression slopes and vertical axis interceptions from the EDX correlation plots, the maximum percentage of oxygen to silicon in the nanowires ($(O/Si)_{nw}$) was determined to $5.8\% \pm 0.4\%$ for Gt-SnO_2-SiNW and $0.5\% \pm 0.1\%$ for Gt-SnS-SiNW, while the maximum percentage of oxygen to tin in the catalyst particles ($(O/Sn)_{cat}$) was $25.9\% \pm 1.7\%$ for Gt-SnO_2-SiNW and $2.7\% \pm 0.5\%$ for Gt-SnS-SiNW.

The given estimates are averages of the numerical values obtained from all correlation plots, shown in Table A.1.1 in the Appendix. The calculations indicate that the oxygen content in the tin seeds was much higher when SnO_2 was used as a catalyst compared to using SnS, and also that the silicon produced during SiNW growth has a higher oxygen content when SnO_2 was used as seed.

X-ray photoelectron spectroscopy

The Si 2p spectra obtained from X-ray photoelectron spectroscopy on Gt-SnO_2-SiNW and Gt-SnS-SiNW are plotted together in Figure 4.1.5. Two major peaks are visible, with the one at higher binding energy (102 eV) related to siloxanes and the highest peak at 99 eV related to Si(0). [92] A fit of which bonds contribute to the total Si 2p spectra is shown in Figure 4.1.6a for Gt-SnO_2-SiNW and in Figure 4.1.6b for Gt-SnS-SiNW.

Table 4.1.2 lists the elemental composition of the Gt-SiNW composites measured by XPS. The low penetration depth of XPS makes the measured composition specific

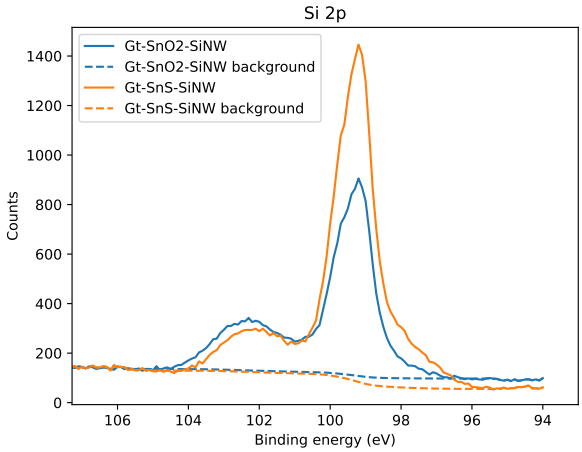

Figure 4.1.5: Comparison of the Si 2p XPS sprectra of Gt-SnO_2-SiNW and Gt-SnS-SiNW.

for the sample surface. The two composites had similar oxygen contents, but Gt-SnS-SiNW measured a significantly higher silicon content than Gt-SnO_2-SiNW, implying a higher oxygen content per silicon in Gt-SnO_2-SiNW as observed in Figure 4.1.5.

Table 4.1.2: Detected weight percentages of the elements in Gt-SnO_2-SiNW and Gt-SnS-SiNW by XPS measurements.

Sample	C	O	Si	Sn
Gt-SnO_2-SiNW	70.7	5.3	15.6	1.6
Gt-SnS-SiNW	66.3	5.7	24.8	3.2

Figure 4.1.6a shows the Si 2p XPS spectrum of Gt-SnO_2-SiNW. The peaks between 99 and 100 eV are attributed to Si(0), while the peaks at 102 and 102.5 eV are from siloxanes. [92] The peaks in the Si 2p spectra appear as doublets due to spin orbit coupling. The spectrum for Gt-SnS-SiNW in Figure 4.1.6b was similar to the spectrum for Gt-SnO_2-SiNW, but with two extra peaks around 98 eV, due to silicides [93], i.e. dissolution of Si in Sn. Another important difference is that the siloxane peak was significantly higher for Gt-SnO_2-SiNW than for Gt-SnS-SiNW, indicating a higher oxygen content in the silicon product when using a SnO_2 seed for silicon nanowire growth.

The C 1s XPS spectrum for Gt-SnS-SiNW is shown in Figure 4.1.6c, with graphite and C-C bonds giving rise to the most prominent peak. Several small peaks between 286 and 288 eV are present due to defects in graphite, with C-O and C=O as important signals. [94] The peak at 283.5 eV is due to carbides [95], so Si-C bonds possibly

originating from a phenyl layer on the nanowires when using diphenylsilane as precursor. [60] Figure 4.1.6d shows the O 1s spectrum for Gt-SnS-SiNW. The peak at 532 eV is attributed to either Si-O or C-O, and the peak at 530 eV is expected to originate from SnO_2. [96] Thus, even though SnS was used as seed, some SnO_2 was created when the Sn metal formed inside the reactor was exposed to air. Both the O 1s and C 1s spectra were similar for Gt-SnO_2−SiNW as for Gt-SnS-SiNW, and the complete collection of XPS data can be found in Appendix B.1.

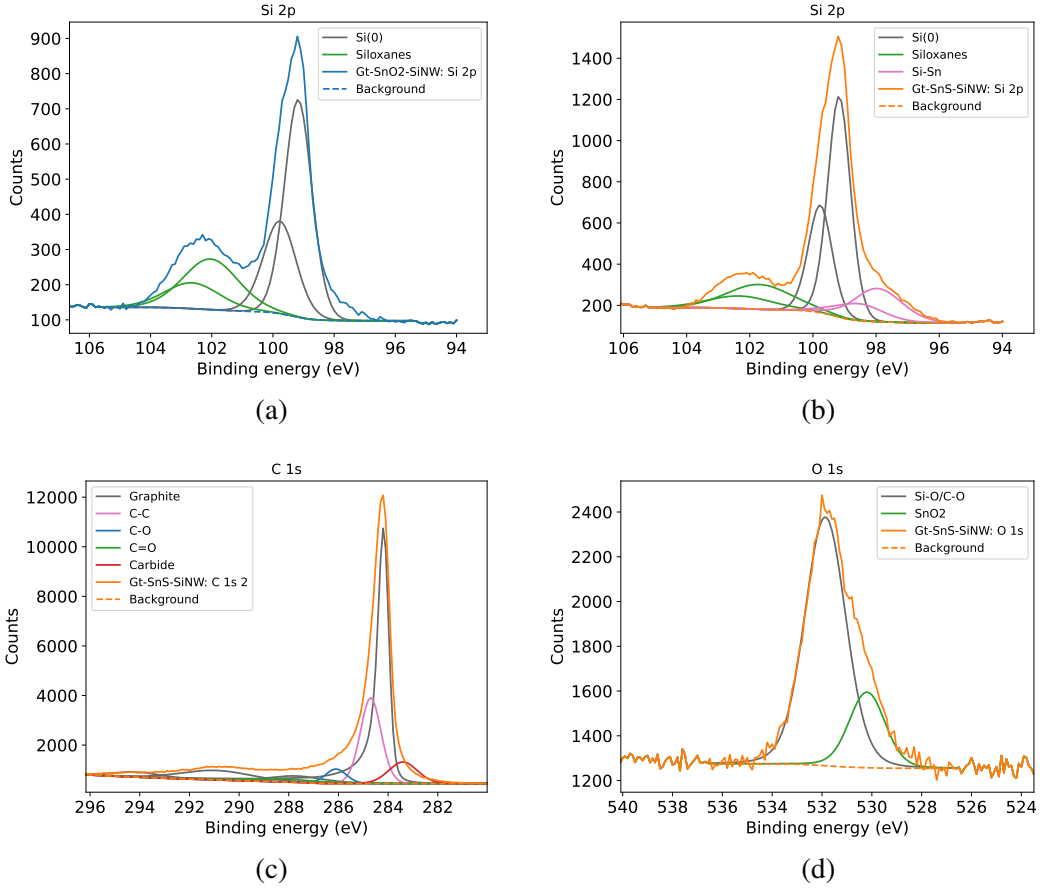

Figure 4.1.6: Si 2p XPS spectrum for Gt-SnO_2-SiNW in (a) and Si 2p, C 1s and O 1s spectra for Si-SnS-SiNW in (b), (c) and (d).

4.1.4 Battery performance

Charge/discharge curves

The charge/discharge curves for two selected cells are plotted as cell potential versus specific capacity for Gt-SnO_2-SiNW and Gt-SnS-SiNW, shown in Figure 4.1.7a and 4.1.7b, respectively. The charge/discharge curves were plotted for the first and second cycle, cycle 25, cycle 50 and cycle 100. The first cycle had a rate of C/20, while the following cycles had a rate of C/5.

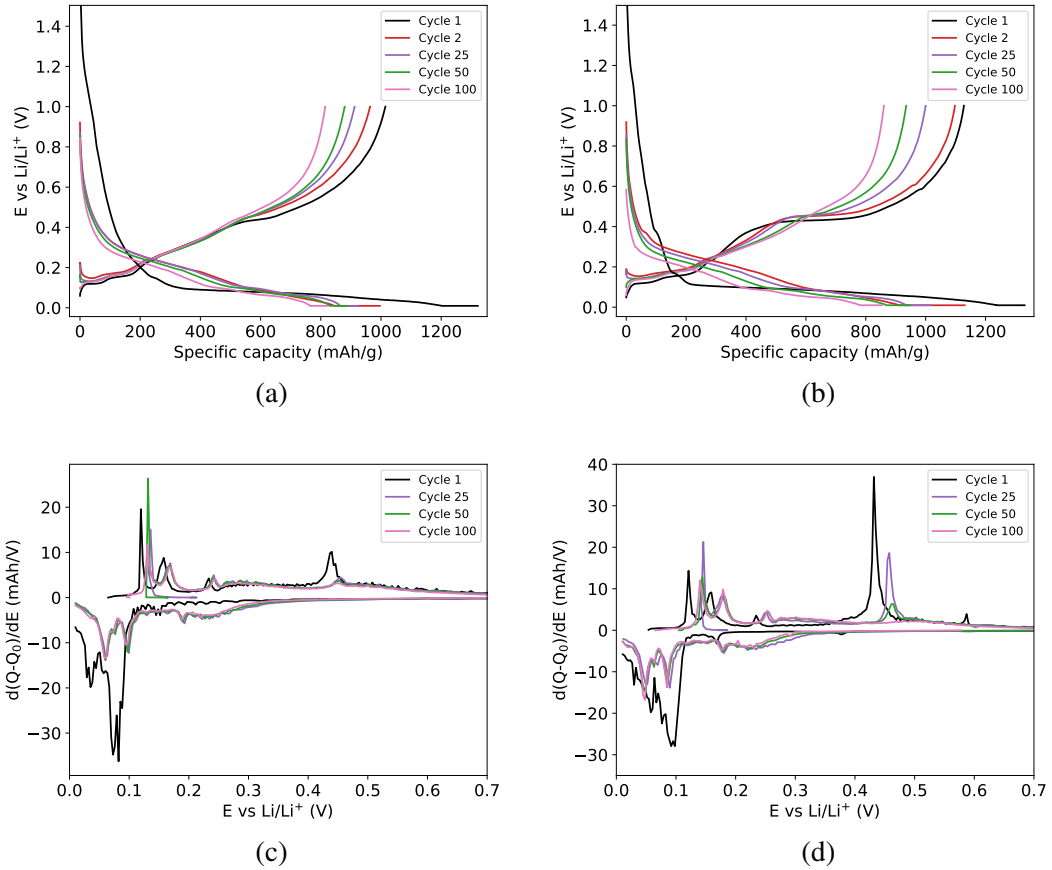

Figure 4.1.7: Charge and discharge profiles of (a) Gt-SnO_2-SiNW and (b) Gt-SnS-SiNW, with the differential capacity plotted versus voltage for the same composites in (c) and (d).

During the first lithiation for both composites the capacity increased for voltages higher than 0.5 V, which was not the case for the subsequent cycles. This was due to SEI-layer formation. [97] A long voltage plateau was observed at 0.1 V which is attributed to the formation of Li_xSi_y-alloys. [33] This was also visible as a peak at 0.1 V in Figure 4.1.7c and Figure 4.1.7d. The same peak was seen for the subsequent

cycles, but with a lower intensity. After the first cycle, a lithiation peak at 0.2-0.25 V appeared. This peak was attributed to lithiation of amorphous silicon. [97]

During delithiation there is no SEI formation, thus the difference between the first and the second cycle was lower than for the lithiation process. For both composites, there were three peaks between 0.1 and 0.25 V in the differential capacity plots indicating delithiation of graphite. [88] A significant peak at 0.4-0.5 V was seen for both composites, with a much higher intensity for Gt-SnS-SiNW. This peak comes from the delithiation of a crystalline $Li_{15}Si_4$-phase, [89] and decreased in strength during cycling. In addition, a small bump was observed around 0.6 V for the initial cycles of Gt-SnS-SiNW, but not for Gt-SnO_2-SiNW, at a potential characteristic for tin delithiation [98].

Cycle life

Figure 4.1.8a shows the specific discharge capacity of the constructed coin cells cycled with various durations, but all went through more than 170 cycles at a C/5-rate. Each composite was represented by two different coin cells with similar performance. The Gt-SnS-SiNW cells were almost identical in terms of specific capacity, while the Gt-SnO_2-SiNW had a capacity gap of around 50 $mA\,h\,g^{-1}$ between the two cells.

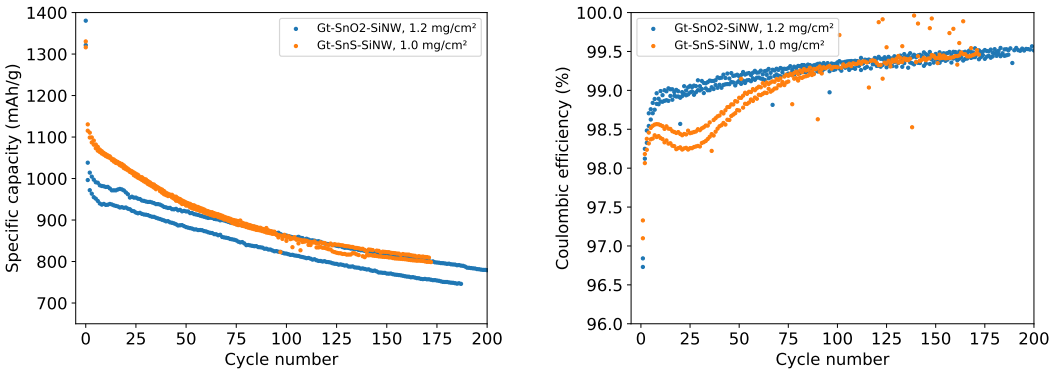

(a) (b)

Figure 4.1.8: Long cycling of two cells from each of Gt-SnO_2-SiNW and Gt-SnS-SiNW, with specific capacity plotted against cycle number in (a) and Coulombic efficiency as a function of cycle number in (b).

Gt-SnO_2-SiNW had a much higher capacity drop from the first to the second cycle than Gt-SnS-SiNW, and showed an initial capacity at 960-1020 $mA\,h\,g^{-1}$ for the first cycles. Gt-SnS-SiNW had an impressive specific capacity of around 1100 $mA\,h\,g^{-1}$ for the first cycles, but experienced a faster capacity loss than Gt-SnO_2-SiNW. At

cycle 70, both the best performing cell from Gt-SnO_2-SiNW and the cells from Gt-SnS-SiNW had a specific capacity of 900 $mA\,h\,g^{-1}$, which shows that Gt-SnS-SiNW had a significantly higher capacity loss during the first 70 cycles. From cycle 2 to cycle 150, Gt-SnO_2-SiNW had an average capacity drop of 223 $mA\,h\,g^{-1}$ (22% of the capacity at cycle 2) for both cells. In the same period, Gt-SnS-SiNW had an average capacity loss of 307 $mA\,h\,g^{-1}$ (27% of the capacity at cycle 2).

The Coulombic efficiency for cycles 2 to 200 are shown in Figure 4.1.8b. Gt-SnS-SiNW and Gt-SnO_2-SiNW had similar CE until cycle 5, where Gt-SnS-SiNW got a dip in CE before it started rising again after 25 cycles. For Gt-SnO_2-SiNW, the CE increased steadily, exceeding 99% at cycle 30. After 100 cycles, both Gt-SnO_2-SiNW and Gt-SnS-SiNW had the same CE at 99.30%, with the Coulombic efficiency still slowly increasing. One of the cells from Gt-SnS-SiNW started experiencing some disturbance around cycle 100, which is seen as noise in the CE-plot. The first CE for Gt-SnO_2-SiNW and Gt-SnS-SiNW were $76.8\% \pm 0.1$ and $85.1\% \pm 0.3$, respectively.

Rate capability

The results from rate capability tests are displayed in Figure 4.1.9, showing the specific capacity versus cycle number for rates between C/20 and 5C indicated on the figure. As C-rate increased, the specific capacity of the cells decreased slowly, both anode composites delivered a specific capacity of more than 900 $mA\,h\,g^{-1}$ at a rate of 1C, after previously going through 20 cycles at slower rates. At 5C all the cells experienced a capacity drop, but returned to a high specific capacity of more than 900 $mA\,h\,g^{-1}$ upon returning to slower rates (C/10 and 1C). Both Gt-SnO_2-SiNW and the Gt-SnS-SiNW with a loading of 0.9 $mg\,cm^{-2}$ had a relatively high specific capacity even at 5C (around 750 $mA\,h\,g^{-1}$), while the higher loaded SnS-grown composite showed lower capacities at high rates. For Gt-SnS-SiNW, the electrodes with lower loading kept a significantly higher specific capacity at 5C. This indicates that the thickness of the electrodes was more important for the high-rate performance than the structural and chemical differences between the composite materials.

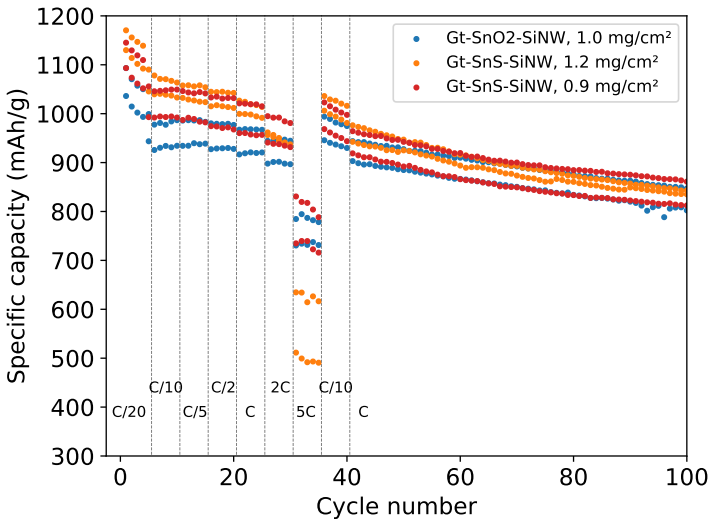

Figure 4.1.9: Specific capacity of Gt-SnO_2-SiNW and Gt-SnS-SiNW half cells when tested at rates between C/20 and 5C.

4.2 Discussion

4.2.1 Synthesis of nanowires using tin catalysts

As mentioned in Section 2.4.2, reduction of SnO_2 and SnS to Sn(0) is necessary for VLS-growth of silicon nanowires. SnS is stable until 350 °C [99], while SnO_2 is observed to withstand temperatures up to 1000 °C. [100] Despite this, the gas production in the reactor started increasing heavily around 150-170 °C for both catalysts (see Figure 4.1.1). High pressure conditions and the reducing properties of diphenylsilane vapors and hydrogen is likely to aid the reduction of SnO_2 and SnS to Sn(0) inside the reactor. The gas production starting at lower temperatures for SnS suggests that SnS is easier reduced to Sn(0), causing hydrogen to get produced at lower temperatures during the VLS wire-growth. Easier reduction of SnS is feasible when considering the oxidation states of Sn in the compounds, with Sn(+II) in SnS and Sn(+IV) in SnO_2.

The SEM images of the synthesized composites in Figure 4.1.2 show a widespread wire growth, an indication of a successful *in-situ* reduction of SnO_2 and SnS. The EDX correlation plot of Sn/C versus Si/C (Figure 4.1.4c) shows a linear correlation between Sn and Si for both composites, with a R^2-value close to 1.0 indicating an accurate fit. This suggests a homogeneous growth of silicon on tin seeds throughout the sample.

Another main takeaway from the EDX measurements is the correlation between oxygen and silicon (Figure 4.1.4a) for the two composites. While Gt-SnO_2-SiNW has a clear increase of oxygen with increasing silicon content, Gt-SnS-SiNW shows the same oxygen fraction regardless of variations in silicon. Calculations by using the slopes of the linear approximations gave an estimate of 5.8% O in silicon for Gt-SnO_2-SiNW and 0.5% O in silicon for Gt-SnS-SiNW, and the difference in oxygen content in the silicon nanowires of the two composites were confirmed by XPS. The Si 2p spectrum of Gt-SnO_2-SiNW gave a twice higher peak attributed to siloxanes than the same spectrum for Gt-SnS-SiNW, seen in Figure 4.1.5. During XPS analysis, 5.3 wt% and 5.7 wt% oxygen was measured for Gt-SnO_2-SiNW and Gt-SnS-SiNW, respectively, while during EDX the same samples gave 2.3 and 1.3 wt% oxygen. For both samples the oxygen content was significantly higher when measuring with the 1-10 nm penetration depth of XPS, than for EDX measurements with a penetration depth of 10-100 µm into the samples that were prepared in an equal way. This indicates that the oxygen is highly concentrated as a surface layer on the silicon nanowires. The two tin catalysts thus create growth of nanowires with different chemical compositions, mainly in terms of a small oxide layer for the wires grown with SnO_2 as seed particles. How this layer may affect the cycling behavior of anodes made from the composite

materials is discussed in Section 4.2.2.

In the XPS Si 2p spectra, a notable difference between Gt-SnO_2-SiNW and Gt-SnS-SiNW is that the bump at 98 eV is only present for Gt-SnS-SiNW. This peak is attributed to silicides. The very low Si concentration in the eutectic in the Sn-Si phase diagram in Figure 2.4.2b normally makes the silicon and tin phases separate, which makes the detection of silicides a surprising result. Due to the silicides only being observed for the Gt-SnS-SiNW sample, a hypothesis could be that the dissolution of Si in Sn increases when sulfur is present. Another interesting result from the XPS analysis was the carbide (Si-C) peak at a binding energy of 283.5 eV. This was observed for both composites. As seen in Figure 4.1.6c, the fitted peak is a bit overestimated, but it indicates the presence of silicon-carbon bonds. The source of these bonds could be the Si-C bond between the silicon wires and phenyl groups from the diphenylsilane or phenylsilane precursors, as thin phenyl layers already have been observed on the surface of Si nanowires with diphenylsilane precursors. [60]

4.2.2 Battery performance of tin-grown Gt-SiNW anodes

Measured through EDX, the silicon contents of the composites were very similar, at 22 wt% and 21 wt% silicon in Gt-SnO_2-SiNW and Gt-SnS-SiNW, respectively, indicating that the silicon content was well controlled by optimizing the amount of graphite substrate, catalyst seeds and silicon precursor added. A similar silicon content between the samples is crucial to be able to compare the electrochemical performance of electrodes made from the two composites. The XPS analysis gave a wider gap between the silicon contents of the samples, at 16% Si for Gt-SnO_2-SiNW and 25% for Gt-SnS-SiNW, but due to the limited penetration depth of XPS and a larger oxide layer on the surface of Gt-SnO_2-SiNW, a lower Si signal for Gt-SnO_2-SiNW from XPS measurements is expected.

As the voltage is decreased from open circuit voltage towards 0.2 V in the cycling profiles in Figure 4.1.7, the specific capacity increases to 200 $mA\,h\,g^{-1}$ for Gt-SnO_2-SiNW, while Gt-SnS-SiNW gets a smaller capacity increase. The specific capacity increase at these voltages during the first lithiation is due to SEI-layer formation, [23] which seems to be larger for Gt-SnO_2-SiNW. An increased oxide content in the silicon composite can lead to an increased SEI layer growth due to the formation of Li_2O and other lithium silicates, [75] which decreases first Coulombic efficiency of the battery. Gt-SnO_2-SiNW does have a lower first Coulombic efficiency than Gt-SnS-SiNW, with values of 78% and 85%, respectively. A high first cycle consumption of lithium is detrimental for the lifetime of the battery in a full cell with the Gt-SiNW anode coupled against a commercial cathode with limited lithium supply. When testing in half-cell configuration using lithium metal as counter electrode, the lithium supply is high and the damaging effect on the battery lifetime of the first cycle Li consumption is not as easily observed.

Figure 4.1.8a shows the capacity retention of the electrodes formulated from Gt-SnO_2-SiNW and Gt-SnS-SiNW during continuous cycling at C/5, where Gt-SnO_2-SiNW shows the best performance with a 5% lower capacity loss from cycle 2 to cycle 150 than Gt-SnS-SiNW. An important observation is that Gt-SnS-SiNW gets a high decrease in specific capacity during the first 50 cycles, but later seems to stabilize and get a similar capacity retention to Gt-SnO_2-SiNW. The oxide layer on Gt-SnO_2-SiNW could improve cycling stability by restricting the volume changes of the wires upon lithiation and delithiation, [77] and the observation of a higher initial capacity loss with a higher oxygen content in the silicon nanowire anode also fits with previous results. [76] At the same time, even though a difference in oxide content has been identified between Gt-SnO_2-SiNW and Gt-SnS-SiNW, a mass fraction of around 5

wt% oxygen for both samples during XPS is not a dominating amount in the surface of the two composites. This means that there are probably other factors contributing to the difference in cycling performance between the two composites.

As seen in Figure 4.1.3, Gt-SnS-SiNW has a 10 nm higher average nanowire diameter than Gt-SnO_2-SiNW, and better cycling stability for smaller diameter silicon nanowires have previously been reported. [73, 76] Thus, the wire diameter could be one of the main reasons for the improved capacity retention of Gt-SnO_2-SiNW. Smaller nanowires also give shorter Li^+-diffusion distances, [22] which is why Gt-SnO_2-SiNW is expected to have a higher capacity at high rates, as seen in Figure 4.1.9.

When continuing lithiation of silicon at voltages lower than 50 mV, crystalline $Li_{15}Si_4$ is expected to form. [23, 30] Since a constant voltage step is applied at 10 mV at the end of each lithiation, there is a high probability that some crystalline $Li_{15}Si_4$ is produced, and the prominent peak at 0.45 V in the differential capacity plots (Figure 4.1.7c and 4.1.7d) indeed demonstrates the presence of c-$Li_{15}Si_4$. [89] A first observation is that the peak is significantly higher for Gt-SnS-SiNW than for Gt-SnO_2-SiNW, where it almost disappears after the first cycle. This is probably due to the larger SiNW diameter of Gt-SnS-SiNW. Schott et al. [89] did a study on graphite/silicon composite anodes with silicon nanoparticles, and they also observed increased $Li_{15}Si_4$-crystallization for increased silicon nanoparticle size.

Crystallization of $Li_{15}Si_4$ has been reported as detrimental for cycling stability due to particle cracking and pulverization, [22, 30, 34] as well as a higher reactivity with the electrolyte [101], which could explain the increased capacity fade for the Gt-SnS-SiNW electrode. During cycling, the characteristic peak in differential capacity (Figure 4.1.7d) at 0.45 V during delithiation of c-$Li_{15}Si_4$ gradually disappears, being close to removed at cycle 50. After cycle 50, the capacity retention and the CE of Gt-SnO_2-SiNW starts improving. Thus, the increased formation of crystalline $Li_{15}Si_4$ might be the reason behind the lower cycle life of Gt-SnS-SiNW compared to Gt-SnO_2-SiNW.

The drop in Coulombic efficiency for Gt-SnS-SiNW seen in Figure 4.1.8b has also been reported for silicon nanoparticles by Keller et al. [73], with an increasily visible CE-drop for particles with increasing size. They attributed it to electrochemical sintering, leading to larger nanoparticles more susceptible to pulverization and thus causing a CE-loss. They also mentioned electrochemical sintering being favoured by deep lithiation due to large volume expansion of Si, connecting $Li_{15}Si_4$-formation to the loss in CE. The formation of c-$Li_{15}Si_4$ has also lead to reduced Coulombic

efficiency for SiNW in previous works. [102]

The rate performance of the electrodes showed in Figure 4.1.9 does not imply that nanowire diameter difference between the composites or a thin oxide layer on Gt-SnO_2-SiNW makes a huge impact on the capacity retention at high rates. Rather, the biggest difference is seen when varying the electrode thickness, as as shown for electrodes with loadings of 0.9 and 1.2 $mg\,cm^{-2}$ for Gt-SnS-SiNW. A thinner electrode with lower active material loading normally leads to higher rate performance, as reported in literature due to shorter Li^+ diffusion distances and faster charge transfer kinetics. [103]

Compared to graphite anodes (theoretical specific capacity of 372 $mA\,h\,g^{-1}$) the composites show a high specific capacity, with all cells above 750 $mA\,h\,g^{-1}$ at cycle 150. This is still not as high as some reported Gt-SiNW composites with around 30% Si made with gold catalysts, which had 900 $mA\,h\,g^{-1}$ after 300 cycles. [33] The most severe shortcomings compared to some other efforts on silicon-graphite composites with lower Si contents [80, 81] is not the obtained specific capacity, but rather the capacity retention. This makes sense, as the cycling stability is harder to improve when enhancing capacity through increasing the silicon content. [4, 5] Summarized, the tin-grown Gt-SiNW composite anodes show high energy density, with SnO_2 as the most practical seed due to its commercial availability, but the capacity retention and initial and average CE of the tested coin cells are not yet sufficient for industrial needs. [5]

Chapter 5

Cyclohexasilane as precursor

5.1 Results

5.1.1 Silicon nanowire syntheses

Pure silicon nanowires

A series of 6 pure silicon nanowire syntheses were made with varying precursor compositions: One with pure diphenylsilane ($C_{12}H_{12}Si$), one with pure cyclohexasilane (CHS, Si_6H_{12}), and four mixtures with varying ratio of diphenylsilane and cyclohexasilane. The yield of silicon from each synthesis was calculated by applying Equation (5.1.1),

$$Y_{Si} = \frac{m_{prod} - m_{Au}}{n_{Si} \cdot M_{Si}} \cdot 100\%, \tag{5.1.1}$$

where m_{prod} is the mass of the cleaned product from the synthesis, m_{Au} is the mass of gold nanoparticles added to the reactor, n_{Si} is the total amount of Si added to the reactor in mol and M_{Si} is the molar mass of silicon.

The yield of silicon as a function of the precursor composition is shown in Figure 5.1.1. The precursor composition is described by the fraction of Si coming from CHS based on the total molar amount of Si added to the reactor. The silicon yield was at its lowest (32%) for the growth using pure diphenylsilane as precursor, while when using 20%, 80% or pure CHS in the Si source, the yield was stabilized at close to 40%. In addition to silicon growth on the salt substrate, the pure CHS precursor left a significant amount of silicon crystals in the bottom of the reactor after synthesis, which was not observed for any other samples. When using 54% CHS in the precursor mixture, the resulting yield of silicon was very high, at 62%. This high yield was not

reproduced when testing 46% CHS in the precursor two times, both of which gave a silicon yield of 37%, but another occurrence of >60% has been previously observed in the laboratory for similar precursor compositions.

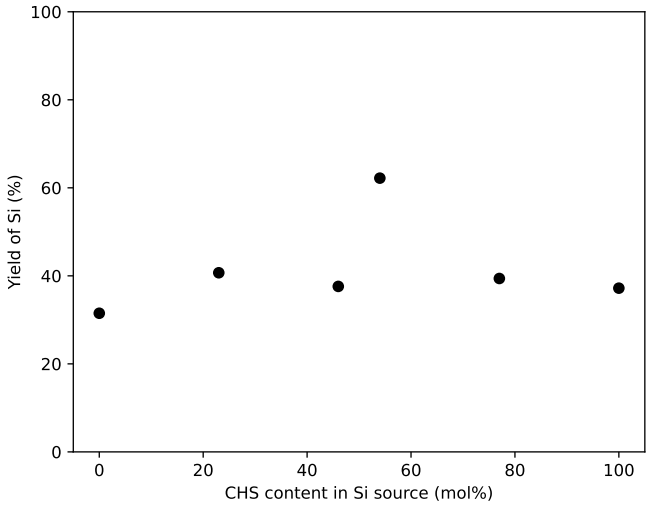

Figure 5.1.1: Yield of silicon during the SiNW syntheses on salt substrate, as a function of precursor composition. The precursor composition is given by the molar percentage of silicon in the precursor mix provided by cyclohexasilane (CHS).

The amount of gas produced in the reactor during each silicon nanowire synthesis is shown in Figure 5.1.2, except for the synthesis with 23% CHS in the silicon source, as technical problems lead to the pressure and temperature not being recorded. The synthesis with 54% CHS in the precursor and the highest yield was also the synthesis with the highest gas production during heating of the reactor. The pressure started increasing sharply at 250 °C, which was earlier than the syntheses with 46%, 77% and 100% CHS in the precursor. They started producing significant amounts of gas around 260 to 270 °C. During the synthesis using pure diphenylsilane, the gas production started at more than 300 °C. Another notable feature is that the sample with 100% CHS as precursor still produced gas after the heating has been turned off. This was not the case for any of the other samples, although for 77% CHS in the precursor the gas amount in the reactor kept stable during cooling. For all the samples with a lower CHS fraction than 77%, the amount of gas in the reactor decreased with cooling, as seen during the use of phenylsilane precursors in Figure 4.1.1.

At the eutectic point between gold and silicon (363 °C), an increase of the slope was observed in Figure 5.1.2 around this temperature for 0% CHS, 46% CHS, 54% CHS and 100% CHS in the precursor, while the sample with 77% CHS in the precursor

had a different behavior, with the sharpest pressure increase around 300 °C.

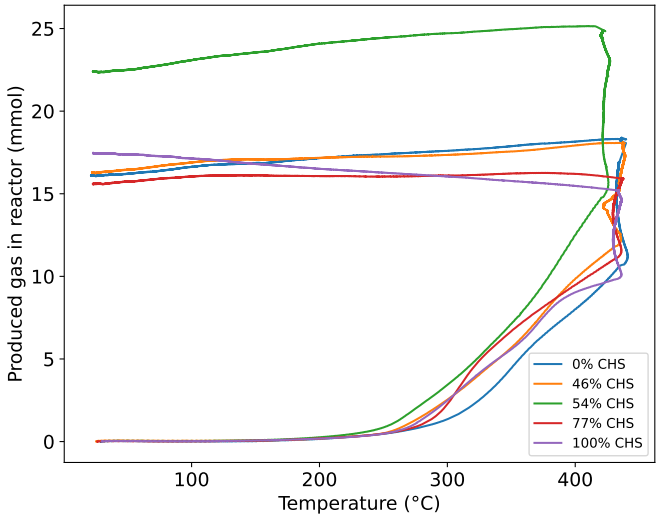

Figure 5.1.2: The molar amount of gas produced in the reactor for each synthesis of pure nanowires, calculated by the ideal gas law.

5.1.2 Microstructure and composition

Figure 5.1.3 shows the microstructure of the products from silicon nanowire synthesis with decreasing molar content of cyclohexasilane in the precursor going from Figure 5.1.3a to Figure 5.1.3e.

Figure 5.1.3a shows the product from using pure CHS as precursor, with flakes and chunks of silicon that have grown on salt particles before being left remaining after the salt was removed with water. No widespread silicon nanowire growth was observed for this synthesis. In Figure 5.1.3b where the precursor was made of 77% CHS wires are visible, but largely covered by chunks of silicon. Figure 5.1.3c and 5.1.3d with 54% and 46% of the total Si in the precursor coming from CHS show a large amount of silicon nanowires. A significant amount of silicon chunks are still present, but not as dominant as for the syntheses with higher CHS content in the precursor. Samples with 23% CHS and pure diphenylsilane precursors are shown in Figure 5.1.3e and Figure 5.1.3f. Those growths resulted in a lot of wires, and smaller silicon chunks than the samples with more CHS in the precursor.

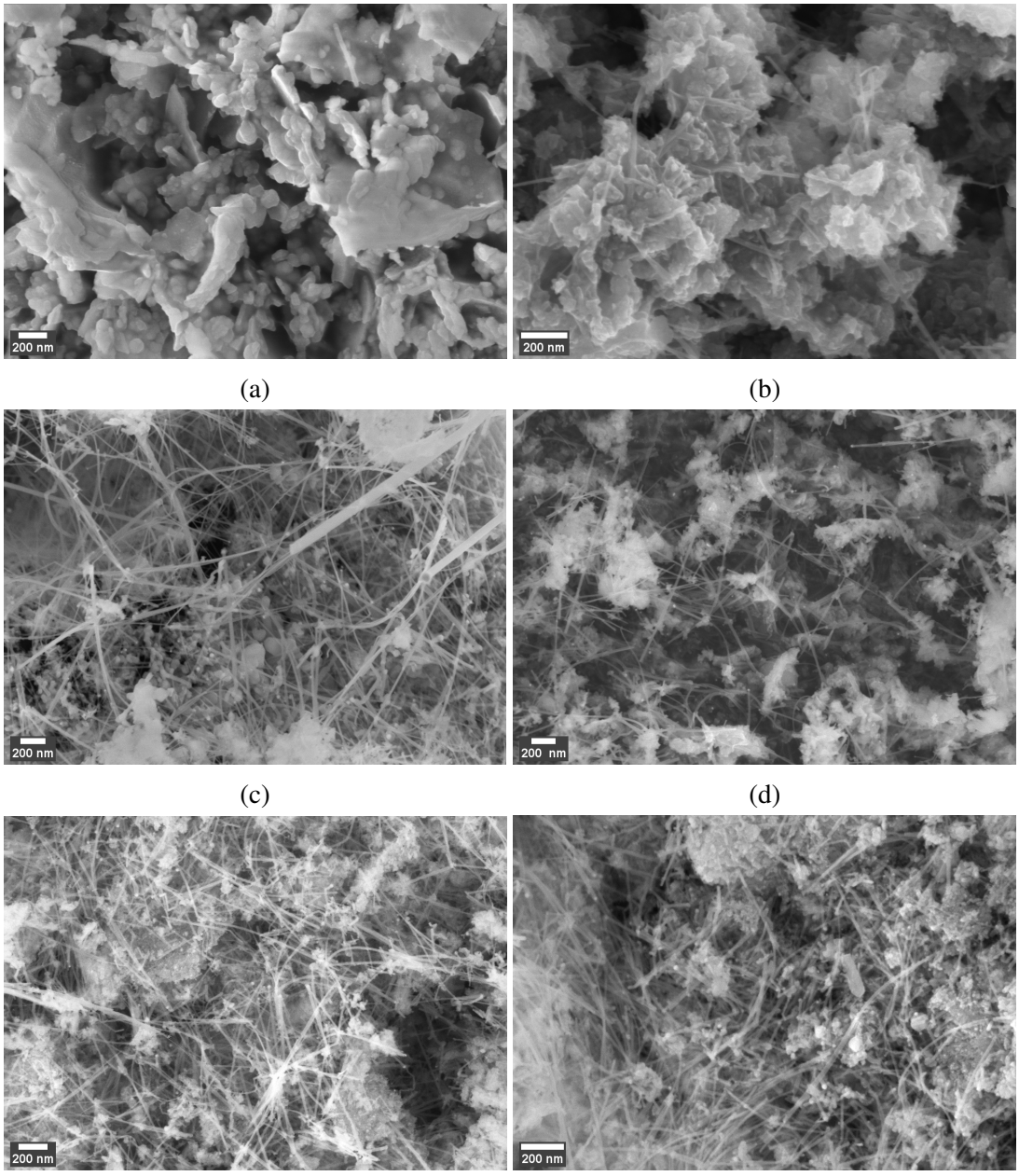

Figure 5.1.3: SEM images of silicon nanowire growths using various ratios of cyclohexasilane and diphenylsilane as precursor: (a) 100%, (b) 77%, (c) 54%, (d) 46%, (e) 23% and (f) 0% molar percentage of Si in the precursor mix coming from CHS.

The weight percentages of carbon and oxygen in the various growths of silicon nanowires on NaCl-substrate, obtained from quantitative EDX measurements, are shown in Figure 5.1.4a and Figure 5.1.4b, respectively. The carbon content decreased with increasing CHS-amount, due to less diphenylsilane and thus less carbon added to the reactor. The weight percent of oxygen got a significant increase when using pure CHS as precursor compared to the other precursor compositions, indicating that the silicon product from the reactor is more tolerant towards oxygen if a high percentage of CHS is used in the precursor. Most likely, the oxygen in the product is gained by oxidation of the silicon surface when opening the reactor and when washing the product in water.

Apart from the oxygen and carbon content, EDX measurements gave a 91-93 wt% Si content for all the nanowire samples. Sodium and chloride contents of less than 0.5 wt% were observed for all samples, indicating a successful salt removal.

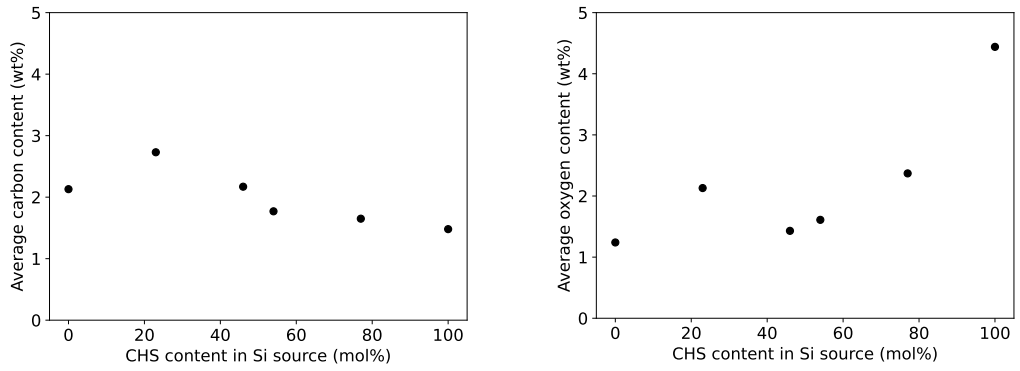

(a) (b)

Figure 5.1.4: Average weight fraction of (a) carbon, and (b) oxygen as a function of the precursor composition, obtained by quantitative EDX measurements on dense samples from SiNW growths on NaCl substrates.

5.1.3 H-NMR

The total spectra of magic angle spinning ^{1}H-NMR analysis are shown in Figure 5.1.5, together with the integrated area of the signal from each sample. The spectra were normalized with regards to sample mass, thus the area of each spectrum is interpreted as the total ^{1}H quantity in the samples, showing that with pure diphenylsilane as precursor, the total ^{1}H content was at its highest.

The sample with 0% CHS has a high peak at 7 ppm, which gradually decreases in strength as the CHS content in the precursor was increased. The peak at 7 ppm is

most likely related to phenyl groups, as they are expected to have a ^{1}H-NMR chemical shift of 6-8 ppm. The spectrum also shows other contributions at lower chemical shifts, with preliminary attributions to Si_nSiH_{4-n} (5.0 ppm), O_nSiH_{4-n} (3.4 ppm) and O_3Si-OH (1.1 ppm). [104]

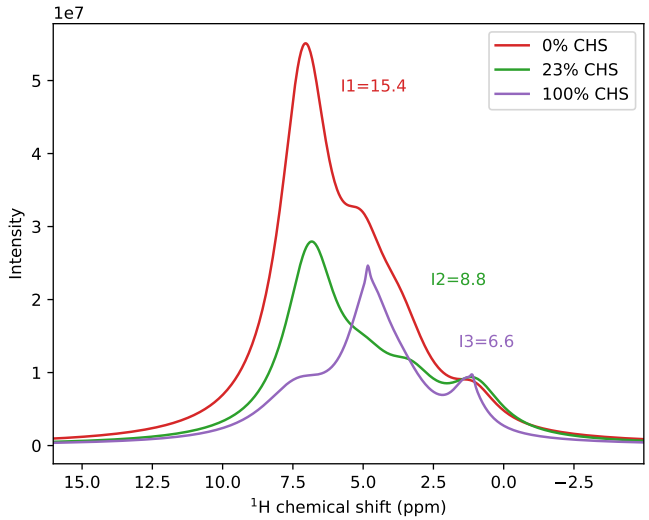

Figure 5.1.5: MAS ^{1}H-NMR spectra for 0%, 23% and 100% CHS in the precursor, normalized with regards to sample mass. The integrated area of each sample is given next to the spectra themselves.

5.1.4 Graphite-silicon nanowire composites

The compositions of the Gt-SiNW composite materials synthesized using CHS as precursor are found in Table 5.1.1, obtained by EDX quantitative analysis. The overall compositions of the two samples were similar, as well as the average silicon contents at 21.2% and 23.6% for Gt-CHS46 and Gt-CHS100, respectively.

Table 5.1.1: Average weight percentages of C, O, Si and Au in the two Gt-SiNW composite active materials grown by using 46% and 100% CHS in the precursor.

Sample	C	O	Si	Au
Gt-CHS46	76.8	1.1	21.2	0.8
Gt-CHS100	74.2	1.3	23.6	0.6

Figure 5.1.6a and Figure 5.1.6c show SEM images of the Gt-SiNW composite synthesized with 100% CHS in the precursor. The graphite grains were largely covered by silicon, but a growth of nanowires was not obtained. Rather, 50 to 100 nm particles

were tightly packed around the graphite grains, making structures resembling balls or short worms.

The Gt-SiNW composite synthesized by using 46% CHS in the precursor is imaged in Figure 5.1.6b and 5.1.6d, showing a notable difference in the wire growth compared to the composite made using a pure CHS precursor. Figure 5.1.6b shows how the nanowires covered the surface of graphite grains. When increasing the magnification, Figure 5.1.6d shows that silicon flakes and agglomerates were present among the wires.

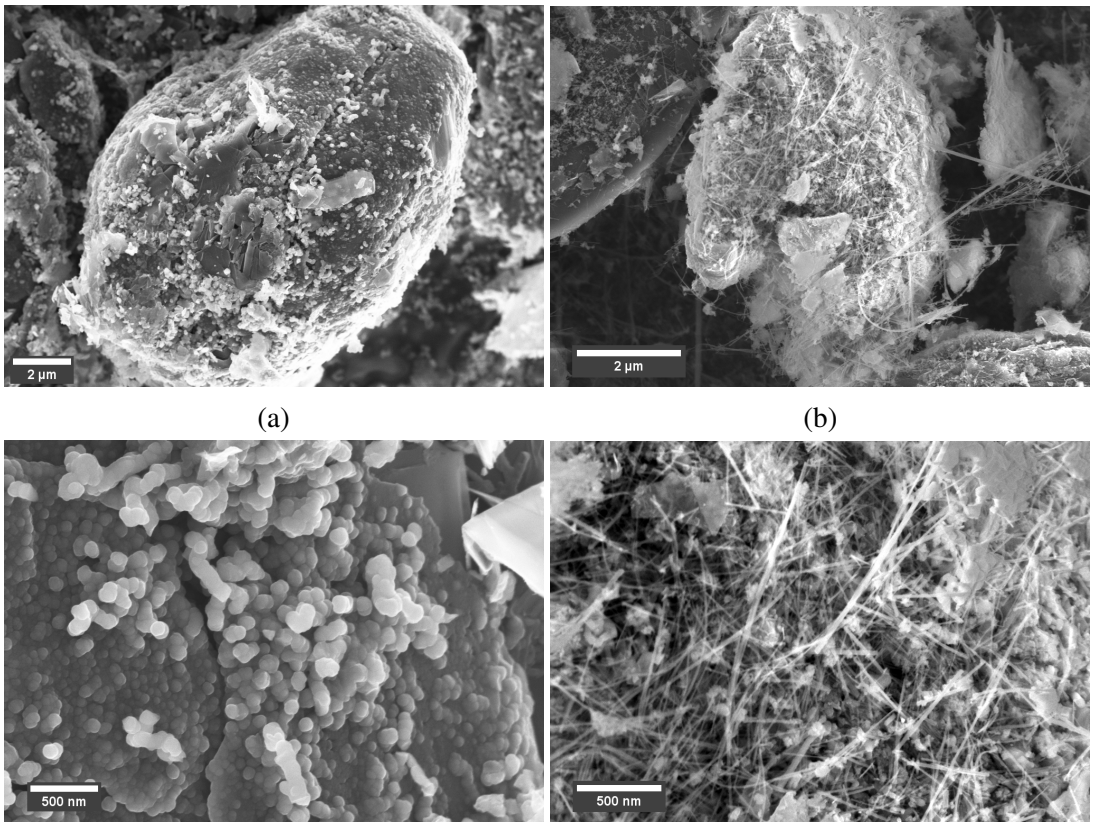

(a) (b)

(c) (d)

Figure 5.1.6: SEM micrographs of the Gt-SiNW composites with a precursor composition of 100% CHS in (a) and (c), and 46% CHS in (b) and (d). The images at the top row (a and b) show graphite grains covered in silicon of different shapes, while the images on the bottom row (c and d) show the same samples at a higher magnification.

5.1.5 Battery performance

Charge/discharge curves

Charge/discharge curves for selected cells of Gt-CHS100 and Gt-CHS46 are plotted in Figure 5.1.7a and 5.1.7b, respectively, as cell voltage versus specific capacity for the first and second cycle, cycle 25 and cycle 50. The first cycle had a rate of C/20, and the following cycles had rates of C/5. The shape of the cycling profiles were similar to the results for Gt-SnO_2-SiNW and Gt-SnS-SiNW seen in Section 4.1.4, showing several plateaus for (de)lithiation processes in graphite and silicon.

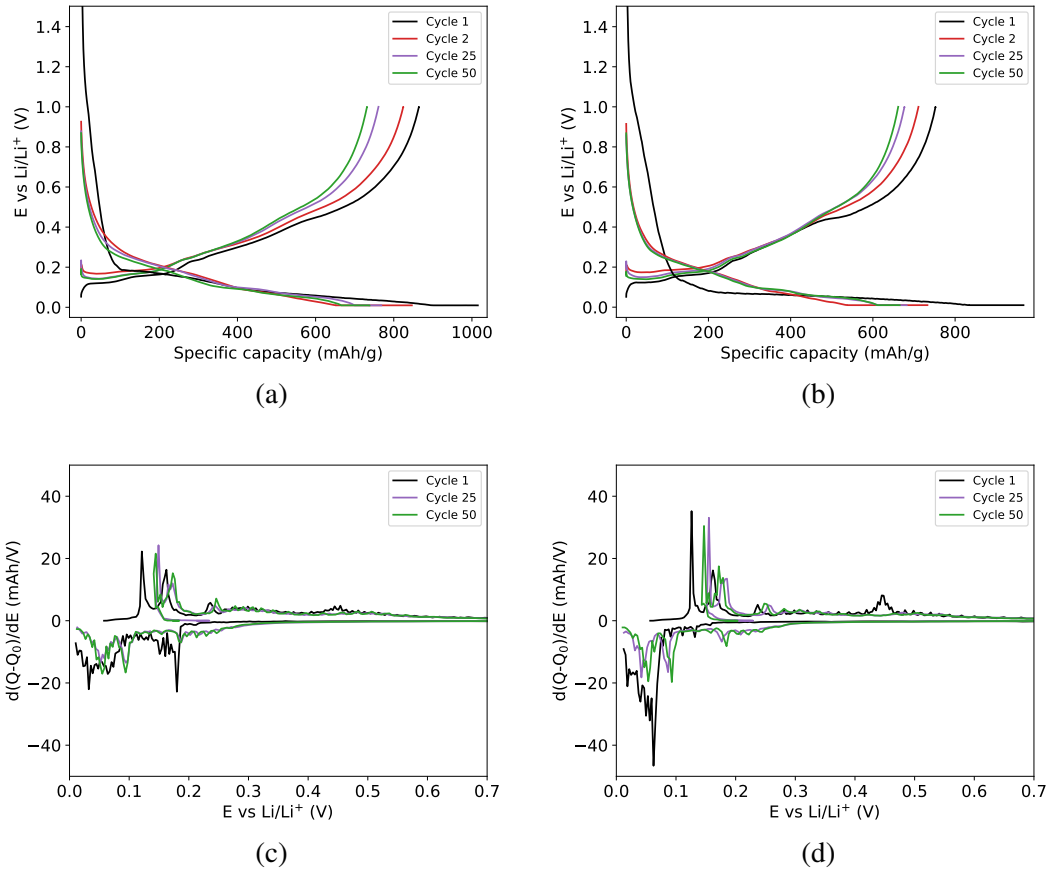

Figure 5.1.7: Charge and discharge profiles of (a) Gt-CHS100 and (b) Gt-CHS46, with the differential capacity plotted versus voltage for the same composites in (c) and (d).

The differential capacity of the two composites are shown in Figure 5.1.7c and 5.1.7d for Gt-CHS100 and Gt-CHS46, respectively. As for Gt-SnO_2-SiNW and Gt-SnS-SiNW, there are three graphite peaks at 0.1-0.3 V, and one peak at 0.4-0.5 V for c-$Li_{15}Si_4$ during delithiation of the anode. [88, 89] The peak of c-$Li_{15}Si_4$ for Gt-

CHS100 in Figure 5.1.7c is very small, and the same peak is more easily visible for Gt-CHS46. At the same time, the peak has already disappeared on cycle 25 for both composites. The lithiation curves of both composites has wide peaks at less than 0.1 V, attributed to lithiation of c-$Li_{15}Si_4$ (at less than 50 mV) and lithiation of Li_xSi_y alloys together with graphite lithiation. Gt-CHS100 has a lithiation peak at 0.2 V attributed to amorphous Si at the first cycle, which is different from all the other Gt-SiNW composites in this work. At cycle 25, both Gt-CHS100 and Gt-CHS46 show small peaks around 0.2 V for lithiation of amorphous Si. The differential capacity curve does not change significantly between cycle 25 and cycle 50 for either of the materials.

Cycle life

Specific capacity as a function of cycle number is shown for Gt-CHS100 and Gt-CHS46 in Figure 5.1.8a, with both composites represented by two cells with similar performance. Both composites had average specific capacities of between 1050 and 1100 $mA\,h\,g^{-1}$ for the first cycle, but Gt-CHS100 had the lowest capacity loss from the first to the second cycle, decreasing to 900 $mA\,h\,g^{-1}$. The second cycle capacity of Gt-CHS46 was around 800 $mA\,h\,g^{-1}$. From cycle 2 to cycle 50, Gt-CHS100 experienced an average specific capacity loss of 109 $mA\,h\,g^{-1}$ (12% of the capacity at cycle 2) while Gt-CHS46 experienced an average loss of 92 $mA\,h\,g^{-1}$ (11% of the capacity at cycle 2) across the two cells. A higher initial capacity loss for Gt-CHS46 indicates more SEI formation during the first lithiation. [97]

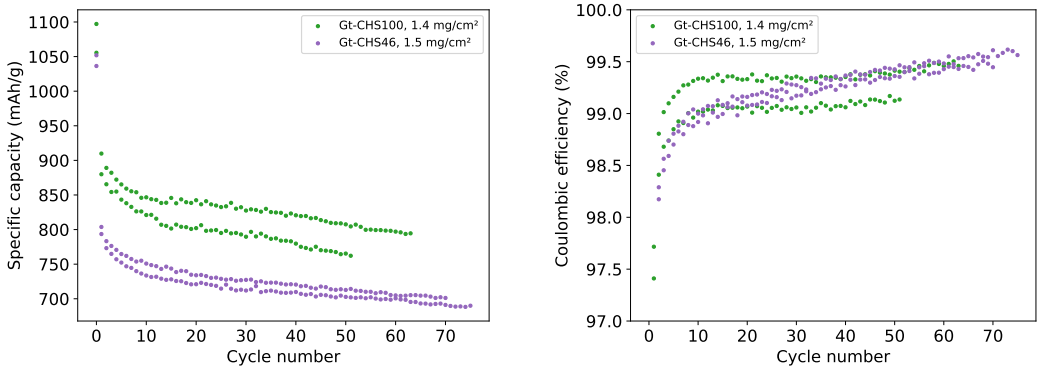

(a) (b)

Figure 5.1.8: Long cycling at C/5 of two cells from each of Gt-CHS100 and Gt-CHS46, with specific capacity plotted against cycle number in (a) and Coulombic efficiency as a function of cycle number in (b).

The Coulombic efficiency of the same cells are shown in Figure 5.1.8b, except for the first CE, which was 85.6 ± 0.4 for Gt-CHS100 and 78.2 ± 0.1 for Gt-CHS46. The Coulombic efficiency for the most efficient cell of Gt-CHS100 increased rapidly up to a high value of 99.4% already after 10 cycles, while the other cell reached 99% at cycle 10 and stabilized at a lower CE. Gt-CHS46 had a slower CE increase, and reached a CE of 99.4% at cycle 40, and continuing to increase towards higher values.

Rate performance

The rate performance of Gt-CHS100 and Gt-CHS46 is shown in Figure 5.1.9. Both composites had an almost constant specific capacity until a rate of 2C, while at 5C the specific capacity got a drastic drop until $285\,\mathrm{mA\,h\,g^{-1}}$ for Gt-CHS100 and and average of $200\,\mathrm{mA\,h\,g^{-1}}$ for Gt-CHS46. After the rate increase, the anodes regained their capacity at C/10, with specific capacities of more than $700\,\mathrm{mA\,h\,g^{-1}}$. There is not a big difference in the performance of the two composites at high rates, Gt-CHS100 only had a slightly superior capacity retention at 5C than Gt-CHS46.

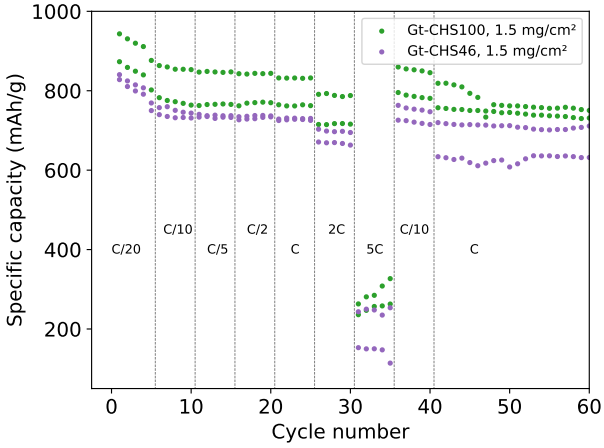

Figure 5.1.9: Specific capacity of Gt-CHS100 and Gt-CHS46 half cells when tested at rates between C/20 and 5C.

5.2 Discussion

5.2.1 Synthesis of silicon nanowires with a cyclohexasilane precursor

It is clear from the SEM images of the pure nanowire growths in Figure 5.1.3 that the amount of silicon nanowires decreases as the fraction of CHS in the precursor increases, indicating that diphenylsilane is a better silicon source than cyclohexasilane in terms of growing nanowires homogeneously throughout the sample. An interesting observation is that for the Gt-SiNW composite, where the substrate is not removed after synthesis in the reactor, a pure CHS precursor gives a different microstructure with nano-sized balls/worms spread across the graphite flakes. Although there are also traces of these "nanoballs" for the growth on salt (Figure 5.1.3a), the balls are much easier identified on the graphite sample (Figure 5.1.6c), not being covered by large flakes and chunks of silicon.

The yield based on the product mass from the reactor in Figure 5.1.1 shows that mixing CHS with diphenylsilane improved the overall silicon yield from the syntheses with around 25%. The pure diphenylsilane growth was the one with the lowest yield. Adding CHS as a precursor complicates the synthesis process because of CHS spontaneously combusting in air, so the initial results of increased Si yield comes with a cost in terms of safety issues. The highest yield at more than 60% could not yet be intentionally reproduced, but the appearance of such high yields more than once proves that it is obtainable with the right growth conditions. During this high-yield growth, the final pressure in the reactor was high (see Figure 5.1.2), which also confirms a high silicon yield as hydrogen gas and other gaseous silane byproducts are expected to be formed during nanowire growth. [58] The reason why these high-yield cases occured is not obvious, and needs to be investigated further.

The gas production in the reactor starts at lower temperatures when CHS is added, showing that the overall reactivity increases. Whether this is from silicon nanowires growing and hydrogen getting produced from silane, or if there are gaseous subproducts from cyclohexasilane is not easy to conclude. Still, compared to changing the catalyst from gold to tin, reducing the catalyst-silicon eutectic temperature, the reduction in temperature for the initial gas production when using CHS as precursor is low. As commented in Section 5.1.1, the amount of gas in the reactor drops during cooling in most of the cases. This is an effect of the condensation of vapors inside the reactor. For the pure cyclohexasilane sample, an opposite trend is observed, as the amount of gas keeps increasing during cooling, even at very low temperatures

(<50 °C). This is probably due to some low-temperature decomposition of cyclohexasilane or its subproducts. The high amount of silicon chunks observed when using a pure CHS precursor (Figure 5.1.3a), together with crystalline Si in the bottom of the reactor indicates that the decomposition of CHS might happen at too low temperatures compared to the formation of the Si-Au eutectic. This leads to reactive silanes from CHS depositing Si on the reactor walls and bottom already before the catalyst drops are ready for nanowire growth.

As the fraction of CHS in the precursor increases, the detected carbon content decreases steadily. This is expected as CHS simply does not add any carbon to the system, while for a phenylsilane precursor, a thin phenyl layer deposits on the wires, as mentioned in previous works. [60] The oxygen content gets a significant increase when using a 100% CHS precursor. A possible explanation would be that phenyls on the surface of silicon nanowires block the absorption of oxygen by turning the surface hydrophobic, and thus avoiding contact of Si-H bonds with water. The normalized total ^{1}H-NMR-spectra in Figure 5.1.5 shows a peak at 7 ppm that could be attributed to phenyls, which decreases in intensity as the CHS content in the precursor increases. This indicates that the wires grown from pure CHS are likely to not have the same phenyl layer as wires grown from diphenylsilane. The values of the integrals over the NMR-spectra could serve as a quantitative measure of the amount of ^{1}H in the samples, showing that the total hydrogen amount decreases when CHS is used, also indicating less presence of phenyls. The gradual decrease of the phenyl peak from ^{1}H-NMR is similar to the gradual decrease in oxygen content from EDX measurements, demonstrating the possible correlation between the phenyl and oxygen contents in the composites.

5.2.2 Battery performance of Gt-SiNW with CHS as Si source

The aim of reaching 20-25 wt% Si in the Gt-SiNW composites was successful, with Si contents of 21 wt% for Gt-CHS46 and 24% for Gt-CHS100. Thus, differences in their electrochemical performance can be assumed to be independent of the amount of Si in each sample. The EDX analysis of the graphite composites with mass fractions of each element given in Table 5.1.1 does not show a high oxygen contrast between 46% CHS and 100% CHS as observed for the pure SiNW syntheses (Figure 5.1.4b). This is probably because a high amount of graphite is present, giving a lower overall Si percentage, thus making the oxygen difference in Si less detectable.

The evolution of specific capacity during cycling (Figure 5.1.8a) shows a higher initial capacity loss for Gt-CHS46 than for Gt-CHS100. The nanowires in Gt-CHS46 have small diameters, which could be the reason for a higher initial capacity loss during the first cycle due to a higher surface area [73], this was also previously observed for the small-sized Gt-SnO_2-SiNW. Gt-CHS100 has the highest first Coulombic efficiency of the two composites, and the CE stabilizes at 99.4% and 99% for the two Gt-CHS100 cells after 10 cycles, while Gt-CHS46 starts at 99% after 10 cycles and increases towards 99.5% after 60 cycles. The same gradual increase in Coulombic efficiency was observed for the tin-grown Gt-SiNW composites in Figure 4.1.8b, so there is a difference in the evolution of Coulombic efficiency when comparing silicon nanowires to the silicon "nanoballs" in Gt-CHS100. The decreasing amount of c-$Li_{15}Si_4$ during cycling, seen by the disappearing peak at 0.45 V between cycle 1 and cycle 25 in the differental capacity plot in Figure 5.1.7d could be one of the reasons for the steadily increasing CE of Gt-CHS46. [102] When looking at the rate capability of the composites in Figure 5.1.9, both composites have a respectable specific capacity of more than $650\,mA\,h\,g^{-1}$ at 2C and more than $200\,mA\,h\,g^{-1}$ at 5C. There are no big differences between their capacity loss at higher rates up to 5C, indicating that the structure and size differences do not have a big impact on the capacity retention at high rates.

Gt-CHS100 has a strong lithiation peak at close to 0.2 V in the differential capacity plot shown in Figure 5.1.7c already for the first cycle. This is not observed for any other Gt-SiNW composite in this work. Lithiation peaks around this voltage are normally attributed to lithiation of amorphous silicon, [97] suggesting that the silicon "nanoballs" are amorphous even before cycling has started. No big peak at 0.45 V during delithiation indicates almost no c-$Li_{15}Si_4$ being formed, which could be benefitial for the cycle life of the battery, due to higher lithium mobility in amorphous Si, allowing lithium ions to access larger portions of the electrode and hence increasing

the capacity. [22]

Although the silicon "nanoballs" in Gt-CHS100 have a relatively big size (50-100 nm diameter), they do not have the same drop in Coulombic efficiency observed in similar sized silicon nanoparticles by Keller et al. [73] or as the large diameter nanowires in Gt-SnS-SiNW. It was discussed in Section 4.2.2 that the CE-drop was connected to the formation of c-$Li_{15}Si_4$, and the absence of both a CE-drop and a c-$Li_{15}Si_4$ phase for Gt-CHS100 supports this theory.

The ^{1}H-NMR measurements suggest that there should be a thin phenyl layer on the silicon nanowires in Gt-CHS46 due to the use of diphenylsilane in the precursor, while no phenyl layer on Gt-CHS100. Because of the difference in both size and morphology of the silicon structures in Gt-CHS46 and Gt-CHS100, is is not easy to say whether the phenyl layer has an effect on the electrochemical performance of the composite anodes. As discussed in Section 5.2.1, a protective phenyl layer can impede silicon oxidation, but a high oxygen contrast was not observed by EDX (1.1 and 1.3 wt% O in Gt-CHS46 and Gt-CHS100, respectively). Neither the expected decreased first Coulombic efficiency [75] was observed for Gt-CHS100, as it actually had 7% higher first Coulombic efficiency than Gt-CHS46. This indicates that a contrast in oxygen content did not heavily influence the electrochemical performance of the composites.

Both Gt-CHS100 and Gt-CHS46 had impressive specific capacities compared to conventional graphite anodes, but they achieved a lower average specific capacity than Gt-SnO_2-SiNW and Gt-SnS-SiNW. The best tin-grown composite in terms of capacity retention (Gt-SnO_2-SiNW) only reaches a Coulombic efficiency of 99.5% at around 200 cycles, while Gt-CHS46 reaches the same Coulombic efficiency before cycle 60, which is promising for the cycle life of the electrode, but still not close to the desired average Coulombic efficiency of 99.8% for industrial applications. [5]

Chapter 6

Conclusion

Silicon nanowires were successfully grown on graphite using SnO_2 or SnS as catalysts, and characterized in terms of their microstructure, chemical composition and electrochemical performance as a composite anode active material with 21-22 wt% Si. The study on tin catalysts showed that SnO_2 formed nanowires with smaller average size, and with an additional oxide layer on the silicon surface, revealed by EDX and XPS analyses. This gave a higher initial capacity loss but a better capacity retention for Gt-SnO_2-SiNW than for Gt-SnS-SiNW. The oxide effect on electrochemical performance was not strong and difficult to distinguish from the size effects.

Six pure SiNW growths using various amounts of cyclohexasilane in mixture with diphenylsilane as precursor showed the effect of CHS on the wire growth and their chemical composition, and two SiNW growths on graphite with 46% and 100% CHS in the precursor were used for anode fabrication and tested in batteries.

Using CHS as precursor resulted in less nanowires and more silicon chunks in the samples, although large amounts of wires were observed for up to 54% CHS in the precursor mixture. Less phenyl groups and more oxygen was identified in the SiNWs grown using CHS-rich precursors, by ^{1}H-NMR and EDX. Silicon yield was improved by 25% when CHS was used in the precursor mix, and an extreme case with more than 60% Si yield was measured but not reproduced. The growth temperature of SiNW was only slightly reduced when using CHS as precursor. When using graphite substrates, 21-24 wt% Si was obtained in the CHS-based Gt-SiNW composites. Gt-CHS100 gave nano-sized balls of Si, while Gt-CHS46 gave thin nanowires, resulting in a higher initial capacity loss for Gt-CHS46 as active material, but at the same time a higher CE. The effect on electrochemical performance due to variations in phenyl- and oxygen content was most probably small compared to the effect of the large difference in size and morphology of the silicon structures in Gt-CHS46 and Gt-CHS100.

Chapter 7

Further Work

Although tin oxide or tin sulfide work well as tin catalysts for SiNW growth, there are other tin compounds to explore. $SnCl_2$ is an example of a commercial Sn(+II) compound that could be tested, to check if the resulting silicon nanowires are similar to the ones grown with SnS, the Sn(+II) compound tested in this work, and to see if Cl being introduced to the reactor has a different effect on the SiNW growth than O or S.

The reasons behind the occurrence of >60% silicon yield for SiNW growth using a mixture of diphenylsilane and cyclohexasilane is something from this work that still needs to be investigated. The moisture of the substrate powder introduced into the reactor is not well controlled other than a drying step on a heating plate before placing the crucible inside the reactor. To find out if the water content is important for the total yield, several SiNW growths with a constant precursor composition could be made while varying the wetting of the substrate powder.

To understand better the mix of diphenylsilane and cyclohexasilane, the mixture of the two could be characterized using liquid ^{1}H-NMR to look at which compounds get formed during mixing of the precursor before addition to the reactor. Another idea is to cut off the heating of the reactor when it has reached different pressures, and let some gas out into a container, before condensating the product and characterizing by ^{1}H-NMR. Like this, more information of what compounds get formed inside the reactor during synthesis could be obtained.

A logical continuation of this work would be to combine the two main parts, making graphite-silicon nanowire composite anodes with a tin catalyst and cyclohexasilane precursor. Possibly, the oxygen or sulfur added through tin oxide or tin sulfide particles could affect the silicon wire growth to give different chemical compositions or morphologies/sizes of the wires when combined with cyclohexasilane.

Bibliography

[1] J. Y. Yong, V. K. Ramachandaramurthy, K. M. Tan, and N. Mithulananthan, "A review on the state-of-the-art technologies of electric vehicle, its impacts and prospects," *Renewable and sustainable energy reviews*, vol. 49, pp. 365–385, 2015.

[2] D. Larcher and J.-M. Tarascon, "Towards greener and more sustainable batteries for electrical energy storage," *Nature chemistry*, vol. 7, no. 1, pp. 19–29, 2015.

[3] L. Lu, X. Han, J. Li, J. Hua, and M. Ouyang, "A review on the key issues for lithium-ion battery management in electric vehicles," *Journal of power sources*, vol. 226, pp. 272–288, 2013.

[4] Y. Jin, B. Zhu, Z. Lu, N. Liu, and J. Zhu, "Challenges and recent progress in the development of si anodes for lithium-ion battery," *Advanced Energy Materials*, vol. 7, no. 23, p. 1700715, 2017.

[5] P. Li, G. Zhao, X. Zheng, X. Xu, C. Yao, W. Sun, and S. X. Dou, "Recent progress on silicon-based anode materials for practical lithium-ion battery applications," *Energy Storage Materials*, vol. 15, pp. 422–446, 2018.

[6] H. Wu and Y. Cui, "Designing nanostructured si anodes for high energy lithium ion batteries," *Nano today*, vol. 7, no. 5, pp. 414–429, 2012.

[7] C.-H. Yim, S. Niketic, N. Salem, O. Naboka, and Y. Abu-Lebdeh, "Towards improving the practical energy density of li-ion batteries: optimization and evaluation of silicon: graphite composites in full cells," *Journal of The Electrochemical Society*, vol. 164, no. 1, p. A6294, 2016.

[8] X. Shen, Z. Tian, R. Fan, L. Shao, D. Zhang, G. Cao, L. Kou, and Y. Bai, "Research progress on silicon/carbon composite anode materials for lithium-ion battery," *Journal of Energy Chemistry*, vol. 27, no. 4, pp. 1067–1090, 2018.

[9] J. Goodenough and K.-S. Park, "The Li-ion rechargeable battery: A perspective," *Journal of the American Chemical Society*, vol. 135, no. 4, pp. 1167–1176, 2013.

[10] V. Etacheri, R. Marom, R. Elazari, G. Salitra, and D. Aurbach, "Challenges in the development of advanced li-ion batteries: a review," *Energy Environ. Sci.*, vol. 4, pp. 3243–3262, 2011.

[11] A. Yoshino, "The birth of the lithium-ion battery," *Angewandte Chemie International Edition*, vol. 51, no. 24, pp. 5798–5800, 2012.

[12] M. S. Whittingham, "Lithium batteries and cathode materials," *Chemical reviews*, vol. 104, no. 10, pp. 4271–4302, 2004.

[13] M. Chen, X. Ma, B. Chen, R. Arsenault, P. Karlson, N. Simon, and Y. Wang, "Recycling end-of-life electric vehicle lithium-ion batteries," *Joule*, vol. 3, no. 11, pp. 2622–2646, 2019.

[14] H. Zheng, R. Yang, G. Liu, X. Song, and V. S. Battaglia, "Cooperation between active material, polymeric binder and conductive carbon additive in lithium ion battery cathode," *The Journal of Physical Chemistry C*, vol. 116, no. 7, pp. 4875–4882, 2012.

[15] N. Nitta, F. Wu, J. T. Lee, and G. Yushin, "Li-ion battery materials: present and future," *Materials today*, vol. 18, no. 5, pp. 252–264, 2015.

[16] Z. Bitew, M. Tessema, Y. Beyene, and M. Amare, "Nano structured silicon and silicon based composites as anode materials for lithium ion batteries: recent progress and perspectives," *Sustainable Energy & Fuels*, 2022.

[17] W. Xu, J. Wang, F. Ding, X. Chen, E. Nasybulin, Y. Zhang, and J.-G. Zhang, "Lithium metal anodes for rechargeable batteries," *Energy & Environmental Science*, vol. 7, no. 2, pp. 513–537, 2014.

[18] A. Manthiram, "An outlook on lithium ion battery technology," *ACS central science*, vol. 3, no. 10, pp. 1063–1069, 2017.

[19] Y.-K. Sun, Z. Chen, H.-J. Noh, D.-J. Lee, H.-G. Jung, Y. Ren, S. Wang, C. S. Yoon, S.-T. Myung, and K. Amine, "Nanostructured high-energy cathode materials for advanced lithium batteries," *Nature materials*, vol. 11, no. 11, pp. 942–947, 2012.

[20] H.-J. Noh, Z. Chen, C. S. Yoon, J. Lu, K. Amine, and Y.-K. Sun, "Cathode material with nanorod structure an application for advanced high-energy and safe lithium batteries," *Chemistry of Materials*, vol. 25, no. 10, pp. 2109–2115, 2013.

[21] W. Zhao, J. Yi, P. He, and H. Zhou, "Solid-state electrolytes for lithium-ion batteries: fundamentals, challenges and perspectives," *Electrochemical Energy Reviews*, vol. 2, no. 4, pp. 574–605, 2019.

[22] S. Jin and J. Szczech, "Nanostructured silicon for high capacity lithium battery anodes," *Energy & Environmental Science*, vol. 4, pp. 56–72, Dec. 2010.

[23] M. Ashuri, Q. He, and L. L. Shaw, "Silicon as a potential anode material for li-ion batteries: where size, geometry and structure matter," *Nanoscale*, vol. 8, no. 1, pp. 74–103, 2016.

[24] S. Goriparti, E. Miele, F. De Angelis, E. Di Fabrizio, R. P. Zaccaria, and C. Capiglia, "Review on recent progress of nanostructured anode materials for li-ion batteries," *Journal of power sources*, vol. 257, pp. 421–443, 2014.

[25] X. Su, Q. Wu, J. Li, X. Xiao, A. Lott, W. Lu, B. W. Sheldon, and J. Wu, "Silicon-based nanomaterials for lithium-ion batteries: a review," *Advanced Energy Materials*, vol. 4, no. 1, p. 1300882, 2014.

[26] J. Besenhard, J. Yang, and M. Winter, "Will advanced lithium-alloy anodes have a chance in lithium-ion batteries?," *Journal of Power Sources*, vol. 68, no. 1, pp. 87–90, 1997.

[27] C. K. Chan, H. Peng, G. Liu, K. McIlwrath, X. F. Zhang, R. A. Huggins, and Y. Cui, "High-performance lithium battery anodes using silicon nanowires," *Nature nanotechnology*, vol. 3, no. 1, pp. 31–35, 2008.

[28] M. T. McDowell, S. W. Lee, W. D. Nix, and Y. Cui, "25th anniversary article: understanding the lithiation of silicon and other alloying anodes for lithium-ion batteries," *Advanced Materials*, vol. 25, no. 36, pp. 4966–4985, 2013.

[29] C. J. Wen and R. A. Huggins, "Chemical diffusion in intermediate phases in the lithium-silicon system," *Journal of solid state chemistry*, vol. 37, no. 3, pp. 271–278, 1981.

[30] M. Obrovac and L. Christensen, "Structural changes in silicon anodes during lithium insertion/extraction," *Electrochemical and solid-state letters*, vol. 7, no. 5, p. A93, 2004.

[31] H. Okamoto, "Li-si (lithium-silicon)," *Journal of Phase Equilibria and Diffusion*, vol. 30, no. 1, pp. 118–119, 2009.

[32] X. H. Liu, J. W. Wang, S. Huang, F. Fan, X. Huang, Y. Liu, S. Krylyuk, J. Yoo, S. A. Dayeh, A. V. Davydov, *et al.*, "In situ atomic-scale imaging of electrochemical lithiation in silicon," *Nature nanotechnology*, vol. 7, no. 11, pp. 749–756, 2012.

[33] S. Karuppiah, C. Keller, P. Kumar, P.-H. Jouneau, D. Aldakov, J.-B. Ducros, G. Lapertot, P. Chenevier, and C. Haon, "A scalable silicon nanowires-grown-on-graphite composite for high-energy lithium batteries," *ACS nano*, vol. 14, no. 9, pp. 12006–12015, 2020.

[34] J. Li and J. Dahn, "An in situ x-ray diffraction study of the reaction of li with crystalline si," *Journal of The Electrochemical Society*, vol. 154, no. 3, p. A156, 2007.

[35] M. Obrovac and L. Krause, "Reversible cycling of crystalline silicon powder," *Journal of the Electrochemical Society*, vol. 154, no. 2, p. A103, 2006.

[36] E. Peled and S. Menkin, "Sei: past, present and future," *Journal of The Electrochemical Society*, vol. 164, no. 7, p. A1703, 2017.

[37] P. Verma, P. Maire, and P. Novák, "A review of the features and analyses of the solid electrolyte interphase in li-ion batteries," *Electrochimica Acta*, vol. 55, no. 22, pp. 6332–6341, 2010.

[38] M. Winter, "The solid electrolyte interphase–the most important and the least understood solid electrolyte in rechargeable li batteries," *Zeitschrift für physikalische Chemie*, vol. 223, no. 10-11, pp. 1395–1406, 2009.

[39] J. H. Ryu, J. W. Kim, Y.-E. Sung, and S. M. Oh, "Failure modes of silicon powder negative electrode in lithium secondary batteries," *Electrochemical and solid-state letters*, vol. 7, no. 10, p. A306, 2004.

[40] W.-J. Zhang, "A review of the electrochemical performance of alloy anodes for lithium-ion batteries," *Journal of Power Sources*, vol. 196, no. 1, pp. 13–24, 2011.

[41] Y. Yao, M. T. McDowell, I. Ryu, H. Wu, N. Liu, L. Hu, W. D. Nix, and Y. Cui, "Interconnected silicon hollow nanospheres for lithium-ion battery anodes with long cycle life," *Nano letters*, vol. 11, no. 7, pp. 2949–2954, 2011.

[42] D. Wang, M. Gao, H. Pan, J. Wang, and Y. Liu, "High performance amorphous-si@ siox/c composite anode materials for li-ion batteries derived from ball-milling and in situ carbonization," *Journal of Power Sources*, vol. 256, pp. 190–199, 2014.

[43] Z. Guo, J. Wang, H. Liu, and S. Dou, "Study of silicon/polypyrrole composite as anode materials for li-ion batteries," *Journal of Power Sources*, vol. 146, no. 1-2, pp. 448–451, 2005.

[44] W. Tao, P. Wang, Y. You, K. Park, C.-Y. Wang, Y.-K. Li, F.-F. Cao, and S. Xin, "Strategies for improving the storage performance of silicon-based anodes in lithium-ion batteries," *Nano Research*, vol. 12, no. 8, pp. 1739–1749, 2019.

[45] N. Liu, Z. Lu, J. Zhao, M. T. McDowell, H.-W. Lee, W. Zhao, and Y. Cui, "A pomegranate-inspired nanoscale design for large-volume-change lithium battery anodes," *Nature nanotechnology*, vol. 9, no. 3, pp. 187–192, 2014.

[46] J. K. Lee, K. B. Smith, C. M. Hayner, and H. H. Kung, "Silicon nanoparticles–graphene paper composites for li ion battery anodes," *Chemical communications*, vol. 46, no. 12, pp. 2025–2027, 2010.

[47] T. Song, J. Xia, J.-H. Lee, D. H. Lee, M.-S. Kwon, J.-M. Choi, J. Wu, S. K. Doo, H. Chang, W. I. Park, *et al.*, "Arrays of sealed silicon nanotubes as anodes for lithium ion batteries," *Nano letters*, vol. 10, no. 5, pp. 1710–1716, 2010.

[48] H. Wu, G. Chan, J. W. Choi, I. Ryu, Y. Yao, M. T. McDowell, S. W. Lee, A. Jackson, Y. Yang, L. Hu, *et al.*, "Stable cycling of double-walled silicon nanotube battery anodes through solid–electrolyte interphase control," *Nature nanotechnology*, vol. 7, no. 5, pp. 310–315, 2012.

[49] X. Li, M. Gu, S. Hu, R. Kennard, P. Yan, X. Chen, C. Wang, M. J. Sailor, J.-G. Zhang, and J. Liu, "Mesoporous silicon sponge as an anti-pulverization structure for high-performance lithium-ion battery anodes," *Nature communications*, vol. 5, no. 1, pp. 1–7, 2014.

[50] H. Jia, X. Li, J. Song, X. Zhang, L. Luo, Y. He, B. Li, Y. Cai, S. Hu, X. Xiao, *et al.*, "Hierarchical porous silicon structures with extraordinary mechanical

strength as high-performance lithium-ion battery anodes," *Nature communications*, vol. 11, no. 1, pp. 1–9, 2020.

[51] V. Schmidt, J. V. Wittemann, S. Senz, and U. Gösele, "Silicon nanowires: a review on aspects of their growth and their electrical properties," *Advanced Materials*, vol. 21, no. 25-26, pp. 2681–2702, 2009.

[52] a. R. Wagner and s. W. Ellis, "Vapor-liquid-solid mechanism of single crystal growth," *Applied physics letters*, vol. 4, no. 5, pp. 89–90, 1964.

[53] S. Barth, F. Hernandez-Ramirez, J. D. Holmes, and A. Romano-Rodriguez, "Synthesis and applications of one-dimensional semiconductors," *Progress in Materials Science*, vol. 55, no. 6, pp. 563–627, 2010.

[54] M. A. Verheijen, G. Immink, T. de Smet, M. T. Borgström, and E. P. Bakkers, "Growth kinetics of heterostructured gap- gaas nanowires," *Journal of the American Chemical Society*, vol. 128, no. 4, pp. 1353–1359, 2006.

[55] S. Kodambaka, J. Tersoff, M. Reuter, and F. Ross, "Diameter-independent kinetics in the vapor-liquid-solid growth of si nanowires," *Physical review letters*, vol. 96, no. 9, p. 096105, 2006.

[56] V. Schmidt, J. Wittemann, and U. Gosele, "Growth, thermodynamics, and electrical properties of silicon nanowires," *Chemical reviews*, vol. 110, no. 1, pp. 361–388, 2010.

[57] S. Akhtar, K. Usami, Y. Tsuchiya, H. Mizuta, and S. Oda, "Vapor–liquid–solid growth of small-and uniform-diameter silicon nanowires at low temperature from si2h6," *Applied physics express*, vol. 1, no. 1, p. 014003, 2008.

[58] D. C. Lee, T. Hanrath, and B. A. Korgel, "The role of precursor-decomposition kinetics in silicon-nanowire synthesis in organic solvents," *Angewandte Chemie*, vol. 117, no. 23, pp. 3639–3643, 2005.

[59] H. Gilman and D. Miles, "Communications-disproportionation reaction of diphenylsilane in the absence of any added catalyst," *The Journal of Organic Chemistry*, vol. 23, no. 2, pp. 326–328, 1958.

[60] O. Burchak, C. Keller, G. Lapertot, M. Salaün, J. Danet, Y. Chen, N. Bendiab, B. Pépin-Donat, C. Lombard, J. Faure-Vincent, *et al.*, "Scalable chemical synthesis of doped silicon nanowires for energy applications," *Nanoscale*, vol. 11, no. 46, pp. 22504–22514, 2019.

[61] X. Lu, K. J. Anderson, P. Boudjouk, and B. A. Korgel, "Low temperature colloidal synthesis of silicon nanorods from isotetrasilane, neopentasilane, and cyclohexasilane," *Chemistry of Materials*, vol. 27, no. 17, pp. 6053–6058, 2015.

[62] H. Okamoto and T. Massalski, "The au- si (gold-silicon) system," *Bulletin of Alloy Phase Diagrams*, vol. 4, no. 2, pp. 190–198, 1983.

[63] R. Wagner, "The vapor-liquid-solid mechanism of crystal growth and its application to silicon," *Trans. Metallur. Soc. AIME*, vol. 233, pp. 1053–1064, 1965.

[64] V. Nebol'Sin and A. Shchetinin, "Role of surface energy in the vapor–liquid–solid growth of silicon," *Inorganic materials*, vol. 39, no. 9, pp. 899–903, 2003.

[65] M. Jeon and K. Kamisako, "Synthesis and characterization of silicon nanowires using tin catalyst for solar cells application," *Materials Letters*, vol. 63, no. 9-10, pp. 777–779, 2009.

[66] G. E. Poinern, Y.-J. Ng, and D. Fawcett, "Fine-tuning of catalytic tin nanoparticles by the reverse micelle method for direct deposition of silicon nanowires by a plasma-enhanced chemical vapour technique," *Journal of colloid and interface science*, vol. 352, no. 2, pp. 259–264, 2010.

[67] F. Xin and M. S. Whittingham, "Challenges and development of tin-based anode with high volumetric capacity for li-ion batteries," *Electrochemical Energy Reviews*, vol. 3, no. 4, pp. 643–655, 2020.

[68] E. Sutter, F. Ivars-Barcelo, and P. Sutter, "Size-dependent room temperature oxidation of tin particles," *Particle & Particle Systems Characterization*, vol. 31, no. 8, pp. 879–885, 2014.

[69] A. M. Chockla, K. C. Klavetter, C. B. Mullins, and B. A. Korgel, "Tin-seeded silicon nanowires for high capacity li-ion batteries," *Chemistry of Materials*, vol. 24, no. 19, pp. 3738–3745, 2012.

[70] I. Ryu, J. W. Choi, Y. Cui, and W. D. Nix, "Size-dependent fracture of si nanowire battery anodes," *Journal of the Mechanics and Physics of Solids*, vol. 59, no. 9, pp. 1717–1730, 2011.

[71] Z. Ma, T. Li, Y. Huang, J. Liu, Y. Zhou, and D. Xue, "Critical silicon-anode size for averting lithiation-induced mechanical failure of lithium-ion batteries," *Rsc Advances*, vol. 3, no. 20, pp. 7398–7402, 2013.

[72] F. Sun, Z. Tan, Z. Hu, J. Chen, J. Luo, X. Wu, G. Cheng, and R. Zheng, "Ultrathin silicon nanowires produced by a bi-metal-assisted chemical etching method for highly stable lithium-ion battery anodes," *Nano*, vol. 15, no. 06, p. 2050076, 2020.

[73] C. Keller, A. Desrues, S. Karuppiah, E. Martin, J. P. Alper, F. Boismain, C. Villevieille, N. Herlin-Boime, C. Haon, and P. Chenevier, "Effect of size and shape on electrochemical performance of nano-silicon-based lithium battery," *Nanomaterials*, vol. 11, no. 2, p. 307, 2021.

[74] J. Yang, Y. Takeda, N. Imanishi, C. Capiglia, J. Xie, and O. Yamamoto, "Siox-based anodes for secondary lithium batteries," *Solid State Ionics*, vol. 152, pp. 125–129, 2002.

[75] Z. Liu, Q. Yu, Y. Zhao, R. He, M. Xu, S. Feng, S. Li, L. Zhou, and L. Mai, "Silicon oxides: a promising family of anode materials for lithium-ion batteries," *Chemical Society Reviews*, vol. 48, no. 1, pp. 285–309, 2019.

[76] M. T. McDowell, S. W. Lee, I. Ryu, H. Wu, W. D. Nix, J. W. Choi, and Y. Cui, "Novel size and surface oxide effects in silicon nanowires as lithium battery anodes," *Nano Letters*, vol. 11, no. 9, pp. 4018–4025, 2011.

[77] Y. Chen, L. Liu, J. Xiong, T. Yang, Y. Qin, and C. Yan, "Porous si nanowires from cheap metallurgical silicon stabilized by a surface oxide layer for lithium ion batteries," *Advanced Functional Materials*, vol. 25, no. 43, pp. 6701–6709, 2015.

[78] F. Dou, L. Shi, G. Chen, and D. Zhang, "Silicon/carbon composite anode materials for lithium-ion batteries," *Electrochemical Energy Reviews*, vol. 2, no. 1, pp. 149–198, 2019.

[79] C. K. Chan, R. N. Patel, M. J. O'connell, B. A. Korgel, and Y. Cui, "Solution-grown silicon nanowires for lithium-ion battery anodes," *ACS nano*, vol. 4, no. 3, pp. 1443–1450, 2010.

[80] M. Ko, S. Chae, J. Ma, N. Kim, H.-W. Lee, Y. Cui, and J. Cho, "Scalable synthesis of silicon-nanolayer-embedded graphite for high-energy lithium-ion batteries," *Nature Energy*, vol. 1, no. 9, pp. 1–8, 2016.

[81] X. Li, P. Yan, X. Xiao, J. H. Woo, C. Wang, J. Liu, and J.-G. Zhang, "Design of porous si/c–graphite electrodes with long cycle stability and controlled

swelling," *Energy & Environmental Science*, vol. 10, no. 6, pp. 1427–1434, 2017.

[82] K. Vernon-Parry, "Scanning electron microscopy: an introduction," *III-Vs Review*, vol. 13, no. 4, pp. 40–44, 2000.

[83] W. Zhou, R. Apkarian, Z. L. Wang, and D. Joy, "Fundamentals of scanning electron microscopy (sem)," in *Scanning microscopy for nanotechnology*, pp. 1–40, Springer, 2006.

[84] J. Chastain and R. C. King Jr, "Handbook of x-ray photoelectron spectroscopy," *Perkin-Elmer Corporation*, vol. 40, p. 221, 1992.

[85] A. Tampieri, M. Szabó, F. Medina, and H. Gulyás, "A brief introduction to the basics of nmr spectroscopy and selected examples of its applications to materials characterization," *Physical Sciences Reviews*, vol. 6, no. 1, 2021.

[86] H. Gunther and H. Gunther, *NMR spectroscopy: basic principles, concepts, and applications in chemistry*. John Wiley & Sons Chichester, UK, 1994.

[87] T. Polenova, R. Gupta, and A. Goldbourt, "Magic angle spinning nmr spectroscopy: a versatile technique for structural and dynamic analysis of solid-phase systems," 2015.

[88] C. Gan, C. Zhang, W. Wen, Y. Liu, J. Chen, Q. Xie, and X. Luo, "Enhancing delithiation reversibility of li15si4 alloy of silicon nanoparticles-carbon/graphite anode materials for stable-cycling lithium ion batteries by restricting the silicon particle size," *ACS Applied Materials & Interfaces*, vol. 11, no. 39, pp. 35809–35819, 2019.

[89] T. Schott, R. Robert, S. Pacheco Benito, P. A. Ulmann, P. Lanz, S. Zurcher, M. E. Spahr, P. Novak, and S. Trabesinger, "Cycling behavior of silicon-containing graphite electrodes, part b: effect of the silicon source," *The Journal of Physical Chemistry C*, vol. 121, no. 46, pp. 25718–25728, 2017.

[90] M. Brust, M. Walker, D. Bethell, D. J. Schiffrin, and R. Whyman, "Synthesis of thiol-derivatised gold nanoparticles in a two-phase liquid–liquid system," *Journal of the Chemical Society, Chemical Communications*, no. 7, pp. 801–802, 1994.

[91] A. de Kergommeaux, J. Faure-Vincent, A. Pron, R. de Bettignies, B. Malaman, and P. Reiss, "Surface oxidation of tin chalcogenide nanocrystals revealed by 119sn–mossbauer spectroscopy," *Journal of the American Chemical Society*, vol. 134, no. 28, pp. 11659–11666, 2012.

[92] R. Alfonsetti, L. Lozzi, M. Passacantando, P. Picozzi, and S. Santucci, "Xps studies on siox thin films," *Applied Surface Science*, vol. 70, pp. 222–225, 1993.

[93] R. Würz, M. Schmidt, A. Schöpke, and W. Fuhs, "Solid-phase epitaxy of casi2 on si (1 1 1) and the schottky-barrier height of casi2/si (1 1 1)," *Applied surface science*, vol. 190, no. 1-4, pp. 437–440, 2002.

[94] R. Blyth, H. Buqa, F. Netzer, M. Ramsey, J. Besenhard, P. Golob, and M. Winter, "Xps studies of graphite electrode materials for lithium ion batteries," *Applied Surface Science*, vol. 167, no. 1-2, pp. 99–106, 2000.

[95] M. Y. Bashouti, C. A. Garzuzi, M. De La Mata, J. Arbiol, J. Ristein, H. Haick, and S. Christiansen, "Role of silicon nanowire diameter for alkyl (chain lengths c1–c18) passivation efficiency through si–c bonds," *Langmuir*, vol. 31, no. 8, pp. 2430–2437, 2015.

[96] M. A. Stranick and A. Moskwa, "Sno2 by xps," *Surface Science Spectra*, vol. 2, no. 1, pp. 50–54, 1993.

[97] C. K. Chan, R. Ruffo, S. S. Hong, R. A. Huggins, and Y. Cui, "Structural and electrochemical study of the reaction of lithium with silicon nanowires," *Journal of Power Sources*, vol. 189, no. 1, pp. 34–39, 2009.

[98] Y. Xu, Y. Zhu, Y. Liu, and C. Wang, "Electrochemical performance of porous carbon/tin composite anodes for sodium-ion and lithium-ion batteries," *Advanced Energy Materials*, vol. 3, no. 1, pp. 128–133, 2013.

[99] S. A. Zaki, M. Abd-Elrahman, A. Abu-Sehly, M. Almokhtar, A. Soltan, and N. Shaalan, "Solar cell fabrication from semiconducting binary tin sulfide alloy on si substrate," *Solar Energy*, vol. 228, pp. 206–215, 2021.

[100] J. Toledo-Antonio, R. Gutierrez-Baez, P. Sebastian, and A. Vazquez, "Thermal stability and structural deformation of rutile sno2 nanoparticles," *Journal of Solid state chemistry*, vol. 174, no. 2, pp. 241–248, 2003.

[101] J. C. Woodard, W. P. Kalisvaart, S. Y. Sayed, B. C. Olsen, and J. M. Buriak, "Beyond thin films: Clarifying the impact of c-li15si4 formation in thin film, nanoparticle, and porous si electrodes," *ACS Applied Materials & Interfaces*, vol. 13, no. 32, pp. 38147–38160, 2021.

[102] M. Schmerling, D. Fenske, F. Peters, J. Schwenzel, and M. Busse, "Lithiation behavior of silicon nanowire anodes for lithium-ion batteries: Impact of functionalization and porosity," *ChemPhysChem*, vol. 19, no. 1, pp. 123–129, 2018.

[103] Y. Kuang, C. Chen, D. Kirsch, and L. Hu, "Thick electrode batteries: principles, opportunities, and challenges," *Advanced Energy Materials*, vol. 9, no. 33, p. 1901457, 2019.

[104] D. Lee, M. Kaushik, R. Coustel, Y. Chenavier, M. Chanal, M. Bardet, L. Dubois, H. Okuno, N. Rochat, F. Duclairoir, *et al.*, "Solid-state nmr and dft combined for the surface study of functionalized silicon nanoparticles," *Chemistry–A European Journal*, vol. 21, no. 45, pp. 16047–16058, 2015.

Appendix A

Calculations

A.1 EDX correlations

The following section shows the detailed calculations behind the EDX correlation results in Section 4.1.3. The objective of these calculations is to prove that the oxygen content in silicon is lower for the sample using SnS and seed than for the sample using SnO_2 as seed. As discussed in Section 4.1.3, one can see from the EDX correlation plots in Figure A.1.1 that the correlation between silicon and oxygen and tin and oxygen are clearly different between the two samples made with different catalysts. The following calculations quantify these differences by estimating the maximum content of oxygen in silicon and tin for the two different samples. Table A.1.1 gives an overview of the calculated values of $(O/Si)_{nw}^{max}$ and $(O/Sn)_{cat}^{max}$ for all the correlation plots.

The first assumption that is made, is that each detected element in the EDX-measurement comes from either the graphite, the grown nanowires or from catalyst particles. Equation (A.1.1) gives an overview of the expected sources of each element. Graphite (gt) is expected to contain carbon and oxygen, the nanowires (nw) are expected to contain Si, O and C, while the catalyst particles (cat) are expected to contain Sn and O. $(Sn/Si)_{tot}$ and $\frac{C_{nw}}{C_{gt}}$ are defined as k and e respectively, as they re-appear several times throughout the calculations.

$$
\begin{aligned}
gt &= C_{gt} + O_{gt} \\
nw &= Si_{nw} + O_{nw} + C_{nw} \\
cat &= Sn_{cat} + O_{cat} \\
k &= (Sn/Si)_{tot} \\
e &= C_{nw}/C_{gt}
\end{aligned}
\tag{A.1.1}
$$

A numerical value for k was found by using the slope of the linear regression Figure A.1.1e, and k was approximated to be 0.224 for Gt-SnO_2-SiNW and 0.174 for Gt-SnS-SiNW.

- Figure A.1.1c shows O/Si versus C/Si, showing how the amount of oxygen and silicon are correlated for the two samples. An expression for the total oxygen content in silicon can be written as follows,

$$
\begin{aligned}
(O/Si)_{tot} &= \frac{O_{gt}}{Si_{nw}} + \frac{O_{cat}}{Si_{nw}} + \frac{O_{nw}}{Si_{nw}} \\
(O/Si)_{tot} &= (O/C)_{gt} * \frac{C_{gt}}{Si_{nw}} + (O/Sn)_{cat} * k + (O/Si)_{nw} \\
(O/Si)_{tot} &= (O/C)_{gt} * ((C/Si)_{tot} - (C/Si)_{nw}) + (O/Sn)_{cat} * k + (O/Si)_{nw} \\
(O/Si)_{tot} &= (C/Si)_{tot} * (O/C)_{gt} - (C/Si)_{nw} * (O/C)_{gt} + (O/Sn)_{cat} * k + (O/Si)_{nw},
\end{aligned}
\tag{A.1.2}
$$

  which can be rewritten as in Equation (A.1.3), with A as the slope of the linear regression curve, and B as the interception with the vertical axis.

$$
\begin{aligned}
(O/Si)_{tot} &= (C/Si)_{tot} * A + B \\
A &= (O/C)_{gt} \\
B &= -(C/Si)_{nw} * (O/C)_{gt} + (O/Si)_{nw} + (O/Sn)_{cat} * k.
\end{aligned}
\tag{A.1.3}
$$

  The value of $(C/Si)_{nw} = 0.065$ was taken from the C/Si ratio in syntheses of pure nanowires without a graphite substrate previously made in the laboratory. By retrieving the numerical values off the graphs, the $(O/Si)_{nw}^{max}$ and $(O/Sn)_{cat}^{max}$ are estimated. It was assumed that $(O/Si)_{nw}$ took its maximum value when $(O/Sn)_{cat} = 0$ and vice versa. The values are shown in (A.1.4) and (A.1.5),

for the Gt-SnO_2-SiNW and Gt-SnS-SiNW samples, respectively. The standard deviation was taken from the regression error in the slope when using the least-squared regression method.

For Gt-SnO_2-SiNW:

$$\begin{aligned} &A = (O/C)_{gt} = 0.015 \pm 0.001 \\ &B = 0.057 \pm 0.005 = -0.065 * A + (O/Si)_{nw} + (O/Sn)_{cat} * k \\ &\underline{\Rightarrow (O/Si)_{nw} < 0.063, \;\; (O/Sn)_{cat} < 0.281} \end{aligned} \tag{A.1.4}$$

For Gt-SnS-SiNW:

$$\begin{aligned} &A = (O/C)_{gt} = 0.018 \pm 0.001 \\ &B = 0.001 \pm 0.004 = -0.065 * A + (O/Si)_{nw} + (O/Sn)_{cat} * k \\ &\underline{\Rightarrow (O/Si)_{nw} < 0.006, \;\; (O/Sn)_{cat} < 0.035} \end{aligned} \tag{A.1.5}$$

- The same calculations are made for the graph of O/C versus Si/C in Figure A.1.1a, finding an expression for $(O/Si)_{nw}$ and $(O/Sn)_{cat}$:

$$\begin{aligned} (O/C)_{tot} &= \frac{O_{gt}}{C_{tot}} + \frac{O_{cat}}{C_{tot}} + \frac{O_{nw}}{C_{tot}} \\ (O/C)_{tot} &= \frac{(O/C)_{gt}}{(1+e)} + (O/Sn)_{cat} * k * (Si/C)_{tot} + (O/Si)_{nw} * (Si/C)_{tot} \\ (O/C)_{tot} &= (Si/C)_{tot} * ((O/Sn)_{cat} * k + (O/Sn)_{nw}) + \frac{(O/C)_{gt}}{(1+e)} \end{aligned} \tag{A.1.6}$$

Equation (A.1.7) gives expressions for the slope and intercept of the linear regression curve:

$$\begin{aligned} (O/C)_{tot} &= (Si/C)_{tot} * B' + A' \\ A' &= \frac{(O/C)_{gt}}{(1+e)} \approx (O/C)_{gt} \\ B' &= (O/Sn)_{cat} * k + (O/Si)_{nw}, \end{aligned} \tag{A.1.7}$$

and the maximum values for $(O/Si)_{nw}$ and $(O/Sn)_{cat}$ are determined.

For Gt-SnO_2-SiNW:

$$\begin{aligned} A' &\approx (O/C)_{gt} = 0.016 \pm 0.002 \\ B' &= 0.054 \pm 0.005 = (O/Si)_{nw} + k * (O/Sn)_{cat} \\ &\underline{\Rightarrow (O/Si)_{nw} < 0.059, \;\; (O/Sn)_{cat} < 0.263} \end{aligned} \tag{A.1.8}$$

For Gt-SnS-SiNW:

$$\begin{aligned} A' &\approx (O/C)_{gt} = 0.018 \pm 0.001 \\ B' &= 0.001 \pm 0.003 = (O/Si)_{nw} + k * (O/Sn)_{cat} \\ &\underline{\Rightarrow (O/Si)_{nw} < 0.004, \;\; (O/Sn)_{cat} < 0.023} \end{aligned} \tag{A.1.9}$$

- O/Sn versus C/Sn is plotted in Figure A.1.1d, with calculations as follows:

$$\begin{aligned} (O/Sn)_{tot} &= \frac{O_{gt}}{Sn_{cat}} + \frac{O_{nw}}{Sn_{cat}} + \frac{O_{cat}}{Sn_{cat}} \\ (O/Sn)_{tot} &= (O/C)_{gt} * \frac{C_{gt}}{Sn_{cat}} + (O/Sn)_{cat} + \frac{(O/Si)_{nw}}{k} \\ (O/Sn)_{tot} &= (O/C)_{gt} * ((C/Sn)_{tot} - \frac{(C/Si)_{nw}}{k}) + (O/Sn)_{cat} + \frac{(O/Si)_{nw}}{k} \\ (O/Sn)_{tot} &= (O/C)_{gt} * (C/Sn)_{tot} - (O/C)_{gt} * \frac{(C/Si)_{nw}}{k}) + (O/Sn)_{cat} + \frac{(O/Si)_{nw}}{k}. \end{aligned} \tag{A.1.10}$$

The slope (C) and intercept (D) is shown in Equation (A.1.11),

$$\begin{aligned} (O/Sn)_{tot} &= (C/Sn)_{tot} * C + D \\ C &= A = (O/C)_{gt} \\ D &= -(C/Si)_{nw} * \frac{C}{k} + \frac{(O/Si)_{nw}}{k} + (O/Sn)_{cat}, \end{aligned} \tag{A.1.11}$$

and the final numerical values are found in Equation (A.1.12) and (A.1.13):

For Gt-SnO_2-SiNW:

$$\begin{aligned} C &= (O/C)_{gt} = 0.018 \pm 0.001 \\ D &= 0.214 \pm 0.014 = -0.065 * \frac{C}{k} + \frac{(O/Si)_{nw}}{k} + (O/Sn)_{cat} \\ &\underline{\Rightarrow (O/Si)_{nw} < 0.052, \;\; (O/Sn)_{cat} < 0.233,} \end{aligned} \tag{A.1.12}$$

For Gt-SnS-SiNW:

$$\begin{aligned} C &= (O/C)_{gt} = 0.019 \pm 0.001 \\ D &= -0.007 \pm 0.026 = -0.065 * \frac{C}{k} + \frac{(O/Si)_{nw}}{k} + (O/Sn)_{cat} \\ &\underline{\Rightarrow (O/Si)_{nw} < 0.005, \;\; \Rightarrow (O/Sn)_{cat} < 0.026.} \end{aligned} \tag{A.1.13}$$

- Figure A.1.1b shows O/C versus Sn/C, the calculations are as follows:

$$\begin{aligned} (O/C)_{tot} &= \frac{O_{gt}}{C_{tot}} + \frac{O_{nw}}{C_{tot}} + \frac{O_{cat}}{C_{tot}} \\ (O/C)_{tot} &= \frac{(O/C)_{gt}}{(1+e)} + ((O/Sn)_{cat} * (Sn/C)_{tot}) + \frac{(O/Si)_{nw}}{k} * (Sn/C)_{tot} \\ (O/C)_{tot} &= (Sn/C)_{tot} * ((O/Sn)_{cat} + \frac{(O/Si)_{nw}}{k} + \frac{(O/C)_{gt}}{(1+e)}) \end{aligned} \tag{A.1.14}$$

The slope (D') and intercept (C') is shown in Equation (A.1.15),

$$\begin{aligned} (O/Sn)_{tot} &= (C/Sn)_{tot} * D' + C' \\ C' &= \frac{(O/C)_{gt}}{1+e} \approx (O/C)_{gt} \\ D' &= (O/Sn)_{cat} + \frac{(O/Si)_{nw}}{k}, \end{aligned} \tag{A.1.15}$$

and the final numerical values are found in Equation (A.1.16) and (A.1.17):

For Gt-SnO_2-SiNW:

$$\begin{aligned} C' &\approx (O/C)_{gt} = 0.016 \pm 0.001 \\ D' &= 0.244 \pm 0.013 = \frac{(O/Si)_{nw}}{k} + (O/Sn)_{cat} \\ &\underline{\Rightarrow (O/Si)_{nw} < 0.058, \;\; (O/Sn)_{cat} < 0.257} \end{aligned} \tag{A.1.16}$$

For Gt-SnS-SiNW:

$$\begin{aligned} C' &= (O/C)_{gt} = 0.018 \pm 0.001 \\ D' &= 0.007 \pm 0.018 = \frac{(O/Si)_{nw}}{k} + (O/Sn)_{cat} \\ &\underline{\Rightarrow (O/Si)_{nw} < 0.004, \;\; (O/Sn)_{cat} < 0.025} \end{aligned} \tag{A.1.17}$$

Table A.1.1: The maximum value of oxygen to silicon ratio in nanowires, $(O/Si)_{nw}$, and the maximum value of oxygen to tin ratio in catalyst particles, $(O/Sn)_{cat}$, calculated by using several EDX elemental correlation plots.

Catalyst	Correlation	$(O/Si)_{nw}^{max}$ (%)	$(O/Sn)_{cat}^{max}$ (%)
SnO_2	O/Si vs C/Si	6.3	28.1
	O/C vs Si/C	5.9	26.3
	O/Sn vs C/Sn	5.2	23.3
	O/C vs Sn/C	5.8	25.7
SnS	O/Si vs C/Si	0.6	3.5
	O/C vs Si/C	0.4	2.3
	O/Sn vs C/Sn	0.5	2.6
	O/C vs Sn/C	0.4	2.5

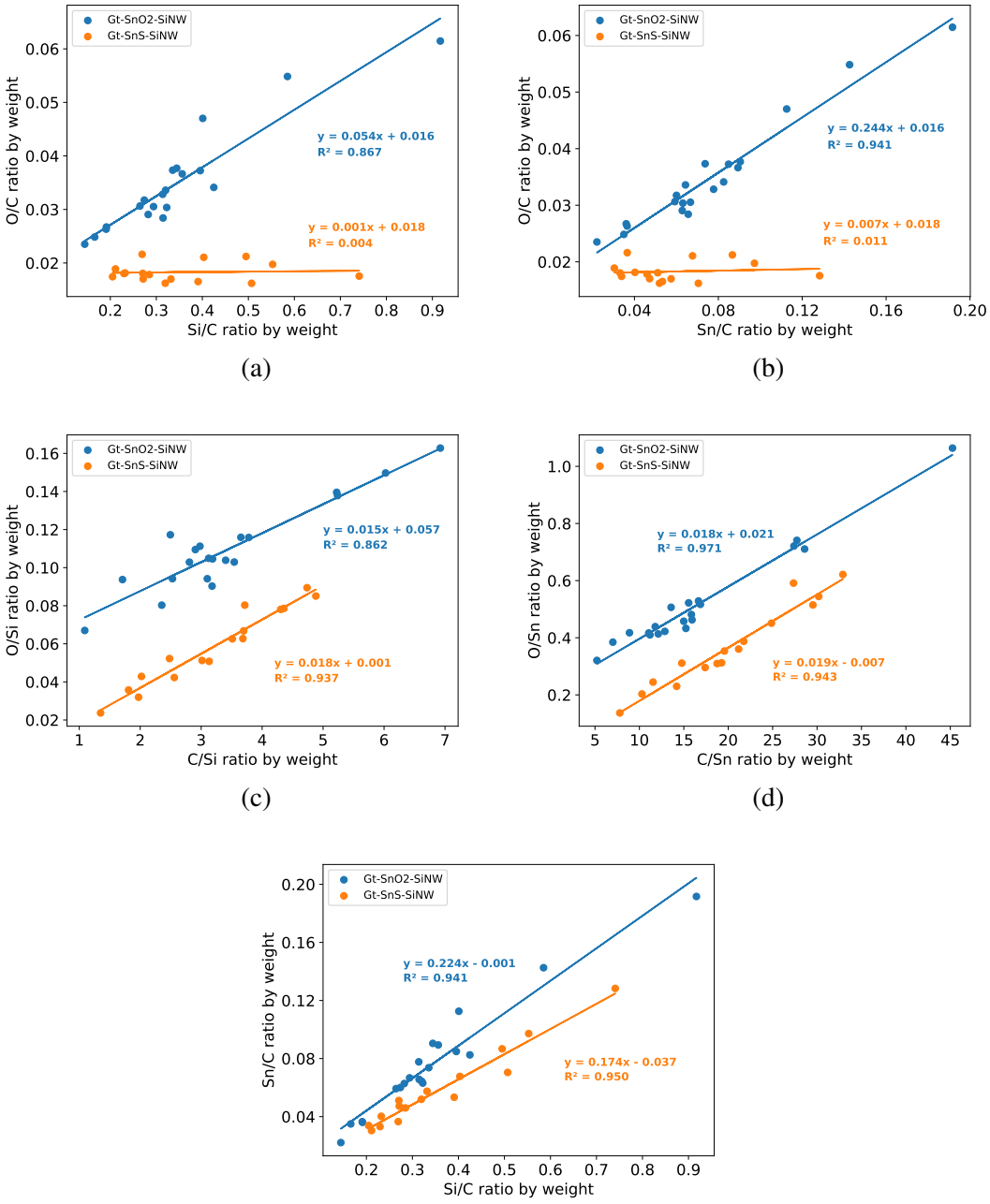

Figure A.1.1: All correlations plots obtained by quantitative EDX analysis, with linear fits and the corresponding coefficients.

Appendix B

B.1 XPS spectra

The full recorded XPS specra for Gt-SnO_2-SiNW and Gt-SnS-SiNW are shown in Figure B.1.1, together with the individual spectra of Si 2p, O 1s and C 1s with corresponding peak-fitting.

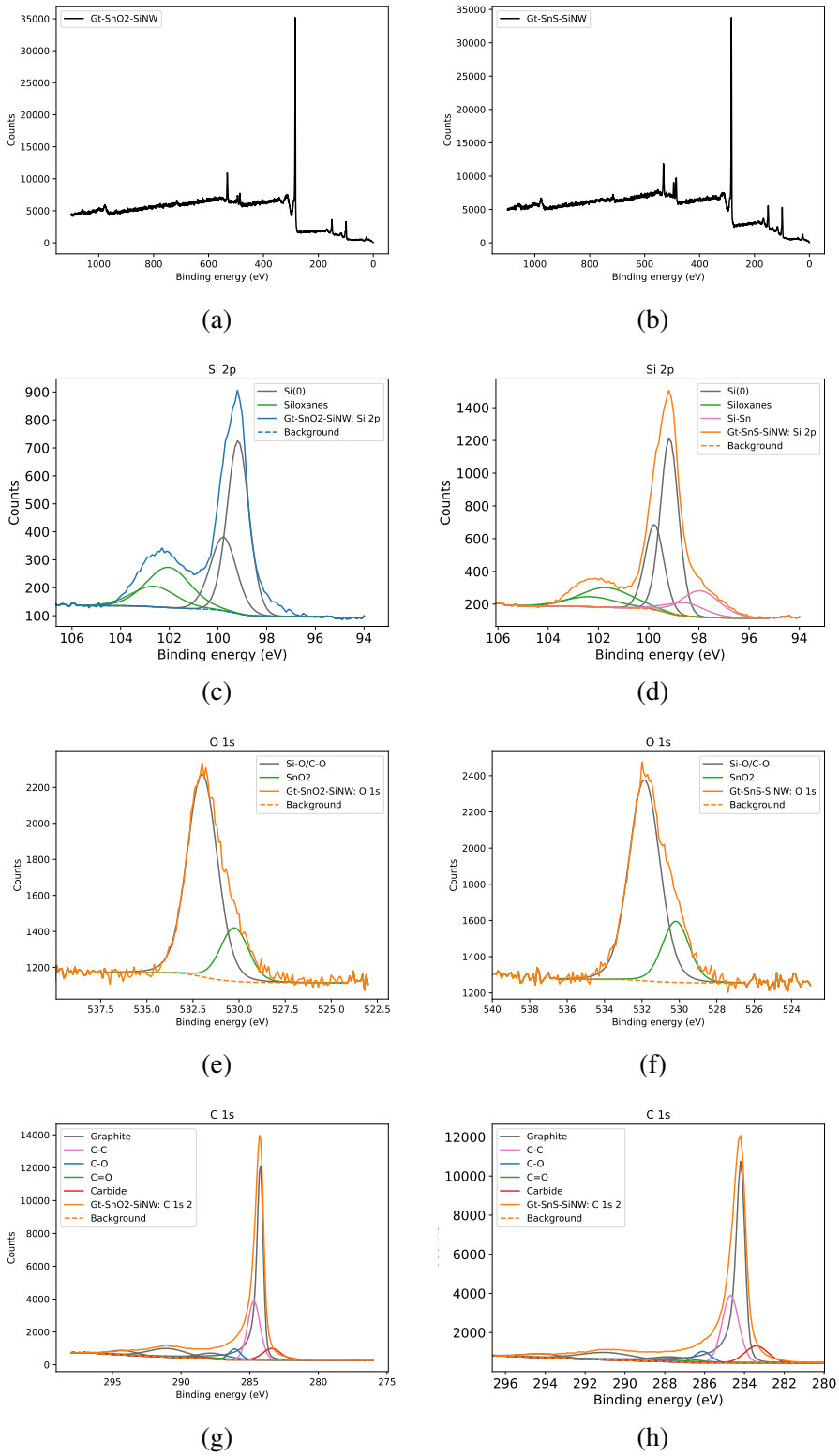

Figure B.1.1: Complete spectra from X-ray photoelectron spectroscopy, with Gt-SnO_2-SiNW on the left and Gt-SnS-SiNW on all rows. (a) and (b) shows the total measured spectra, (c) and (d) shows Si 2p with peak fitting, (e) and (f) shows O 1s with fitting, and (g) and (h) shows C 1s with peak fitting.

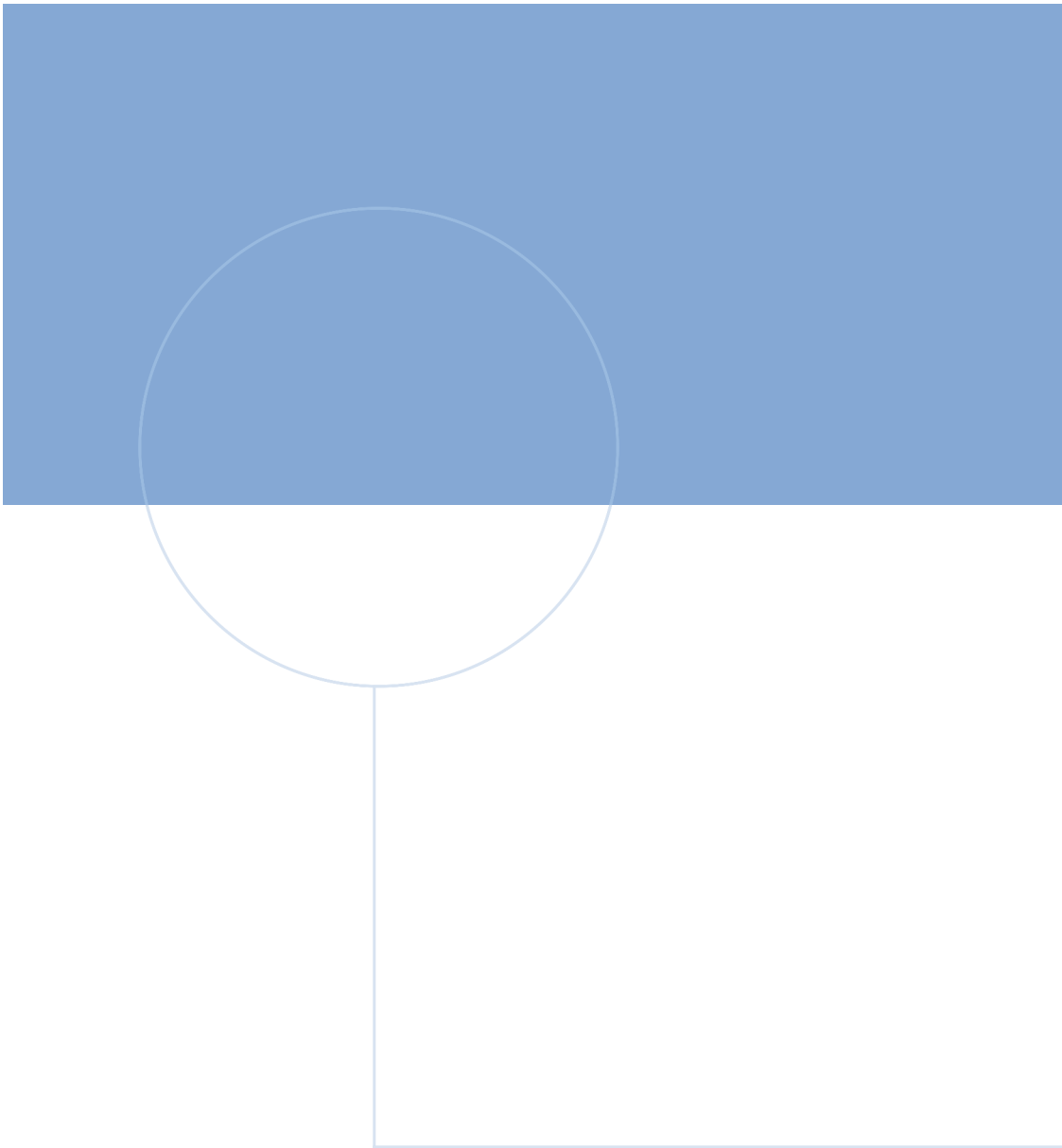

NTNU
Norwegian University of
Science and Technology

cea